Investigation of corium melt interaction with NPP reactor vessel steel (METCOR)
Phase 2

PROGRESS REPORT
2006

INVESTIGATION OF MOLTEN CORIUM INTERACTION WITH VESSEL STEEL IN STEAM ABOVE THE MELT

Tests MC10/05 and MC11/05

Project title	Investigation of Corium Melt Interaction with NPP Reactor Vessel Steel (METCOR, Phase 2), No.833.2	
Contracting organization	ISTC	
File code	METCOR2/RPMC10&11/05	
Project location	Alexandrov Research Institute of Technology of the RF Ministry for Atomic Energy Russia, 188540, Sosnovy Bor, Leningrad Region, NITI	
Project manager	Name	V.B. Khabensky
	Signature	
	Date	

Authors

Dr.(Eng.), Prof.	V. B. Khabensky
Dr.(Eng.)	S. V. Bechta
Ph.D.	V. S. Granovsky
	S. A. Vitol
	E. V. Krushinov
Ph.D.	S. Yu. Kotova
Ph.D.	A. A. Sulatsky
Prof., Associate member of the Russian Academy of Sciences	V. V. Gusarov
Dr.(Eng.), Prof.	Yu. B. Petrov
Ph.D.	I. V. Kulagin
Ph.D.	D. B. Lopukh
Ph.D.	A. Yu. Pechenkov
Ph.D.	I. V. Poznyak
Ph.D.	S. A. Smirnov
	V. I. Almjashev
	V. G. Bliznyuk
	V. R. Bulygin
	E. K. Kalyago
	N. E. Kamensky
	A. V. Lysenko
	A. P. Martynov
	V. V. Martynov
	E. V. Shevchenko
	A. A. Chertkov

ABSTRACT

The report presents a description, results and general conclusions from MC10 and MC11 tests of the ISTC METCOR Phase 2 Project carried out in the NITI, Sosnovy Bor, on the “Rasplav-2” and “Rasplav-3” test facilities.

The test focused on corrosion of vessel steel at its interaction with molten coria UO_{2+x}-ZrO_2 and UO_{2+x}-ZrO_2-FeO_y, in steam, the temperature at the steel specimen surface being within the 950÷1235°C range.

CONTENTS

INTRODUCTION

When a melt is retained in the reactor vessel, mechanical behaviour of the latter is determined, for instance, by thickness of the intact part of the bottom steel wall. In addition to the possible partial melting of the wall, its thickness is also determined by steel ablation resulting from physicochemical interaction with the melt. Phase 1 of the ISTC METCOR Project was devoted to investigating the interaction of the UO_{2+x}-ZrO_2-FeO_y prototypic corium with the cooled 15Kh2NMFA-A vessel steel for VVER-1000 in air above the melt. The performed tests and analyses of the findings showed steel ablation to occur due to its oxidation, while the diffusion processes which determine corrosion kinetics are controlled by a layer of iron oxides that forms atop the steel surface. The proposed dependence for calculating corrosion kinetics generalizes the obtained experimental data in a satisfactory way [1,2].

Though the atmosphere consisting of air ensures high oxygen potential of a melt and the results obtained under these conditions were representative, especially when compared with the those of investigations of the interaction between vessel steel and molten suboxidized corium in an inert atmosphere in METCOR Phase 2 [3,4], an atmosphere consisting of air would not be typical of the severe accident conditions. Therefore, tests with steam above the melt have been performed within the framework of METCOR Phase 2. These were aimed at determining (and comparing with air) the influence of steam, as well as of the corium composition, on the vessel steel corrosion. The present report offers descriptions and results of the said tests, MC10 and MC11.

1 TEST MC10

1.1 Test description

1.1.1 Experimental facility layout

The test was performed on the Rasplav-2 facility that was used during METCOR Phase 1 (MC1÷MC4 tests).

The present test employed the same crucible as was used in MC5÷MC9 tests. In order to provide steam above the melt, the experimental cell design has been modernized so that the above the melt space of the cold crucible was sealed, and a new furnace cover contained a steam inlet pipe, and a gas and aerosols evacuation pipe in addition to the previously used rig. The furnace schematics is given in Fig. 1.1.

A vessel steel specimen is shown in Fig. 1.2. In order to evaluate heat fluxes from melt to the specimen and for cooling the zone of coupling the ultrasonic sensor with the specimen, two calorimeters, the top and bottom ones, were provided.

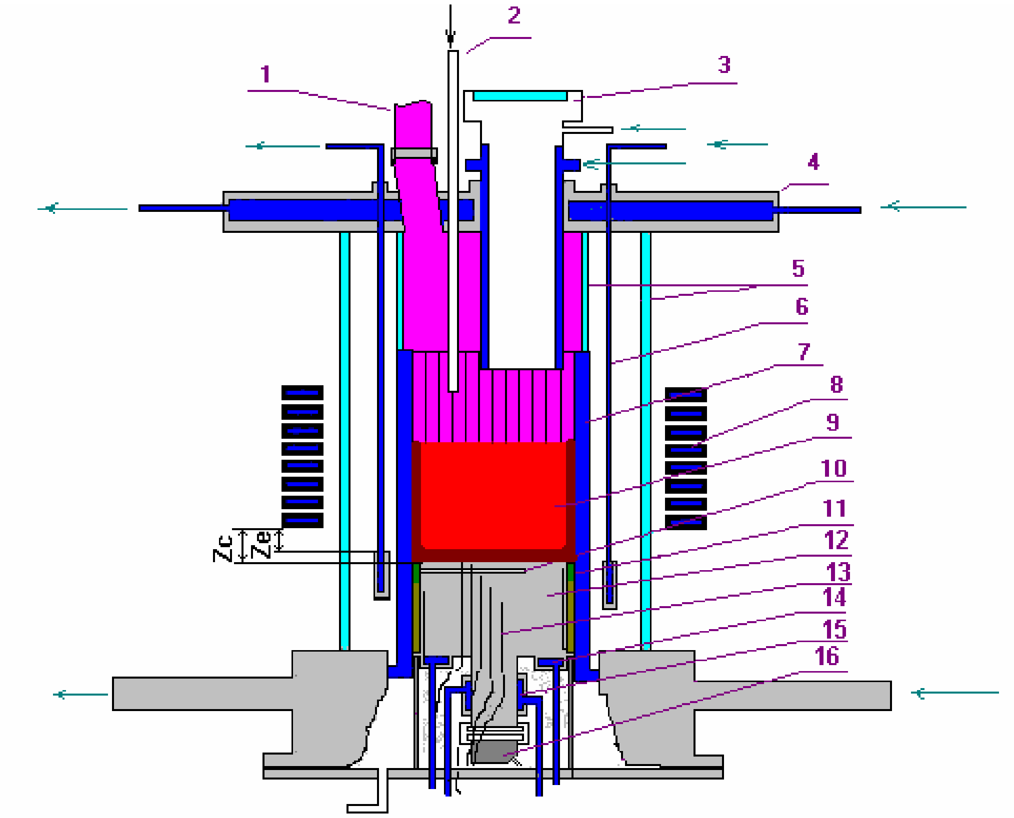

1 – gas and aerosols evacuation pipe; 2 – steam inlet pipe; 3 – water-cooled pyrometer shaft; 4 – water-cooled cover; 5 – quartz tubes; 6 – water-cooled electromagnetic screen; 7 – crucible section; 8 – inductor; 9 – melt; 10 – acoustic defect; 11 – molten ZrO2 (fianite); 12 – vessel steel specimen; 13 – K-type thermocouples; 14 – top specimen calorimeter; 15 – bottom specimen calorimeter; 16 – ultrasonic sensor

Fig. 1.1 – Furnace schematics

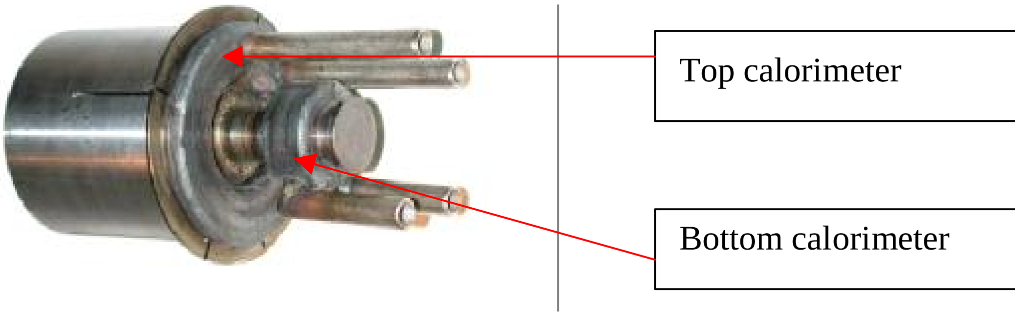

Fig. 1.2 – Vessel steel specimen

Table 1.1 gives the locations of K-type thermocouple junctions in the specimen. Within a 10 mm radius from the specimen axis the thermocouples were embedded into channels Ø 1.5 mm, and within a 29 mm radius – into the 1.5 mm-wide carved grooves.

Table 1.1 – Thermocouple hot junction locations

Thermocouple No.	α° (horizontal angle)	r, mm (distance from the specimen axis)	h, mm (distance from the melt-facing top)
TC01	0	10	8
TC02	90	10	2
TC03	45	10	4
TC04	135	10	3
TC05	270	10	6
TC06	180	10	1
TC07	225	10	20
TC08	315	29	40
TC09	90	29	2
TC10	45	29	4
TC11	225	29	20
TC12	180	29	1
TC13	45	7.5	104

To exclude electromagnetic heating of the specimen, the lower parts of crucible sections were welded together up to above the melt volume, and this arrangement served as an electromagnetic screen. The specimen was positioned in the crucible so that its top was 1 mm below the welded sections top. For the sake of thermal insulation, the gap between the specimen and crucible sections was filled with ZrO_2 powder and pellets of molten stabilized ZrO_2. An additional screening of specimen from induction heating and the bottom crust thickness control in the molten pool were performed by using a water-cooled movable screen. The argon-blasted water-cooled steel shaft was used for the melt surface monitoring.

To control the vessel steel corrosion rates, an acoustic defect was made in the specimen and the same ultrasonic converter as the one used in MC5÷MC9 was employed. Air-tightness of the furnace was ensured by the water-cooled cover and a quartz tube (see Fig. 1.1, Nos. 4 and 5). Sealing of the above the melt space of the cold crucible was ensured using a special dressing and a quartz tube (No. 5 in Fig. 1.1).

A gas-aerosol sampling system (see Fig. 1.3.) was assembled for feeding steam to the above the melt space of the cold crucible, and for controlling oxygen partial pressure in the gases removed from the furnace. A "Sussman electric boilers" (USA) steam generator (3 KW, 6.4 atm. max.) was used as a source of steam. A throttle orifice Ø 0.5 mm was installed at the steam generator outlet for the steam rate regulation. During the test steam rate was determined from the calibration dependence obtained before the test.

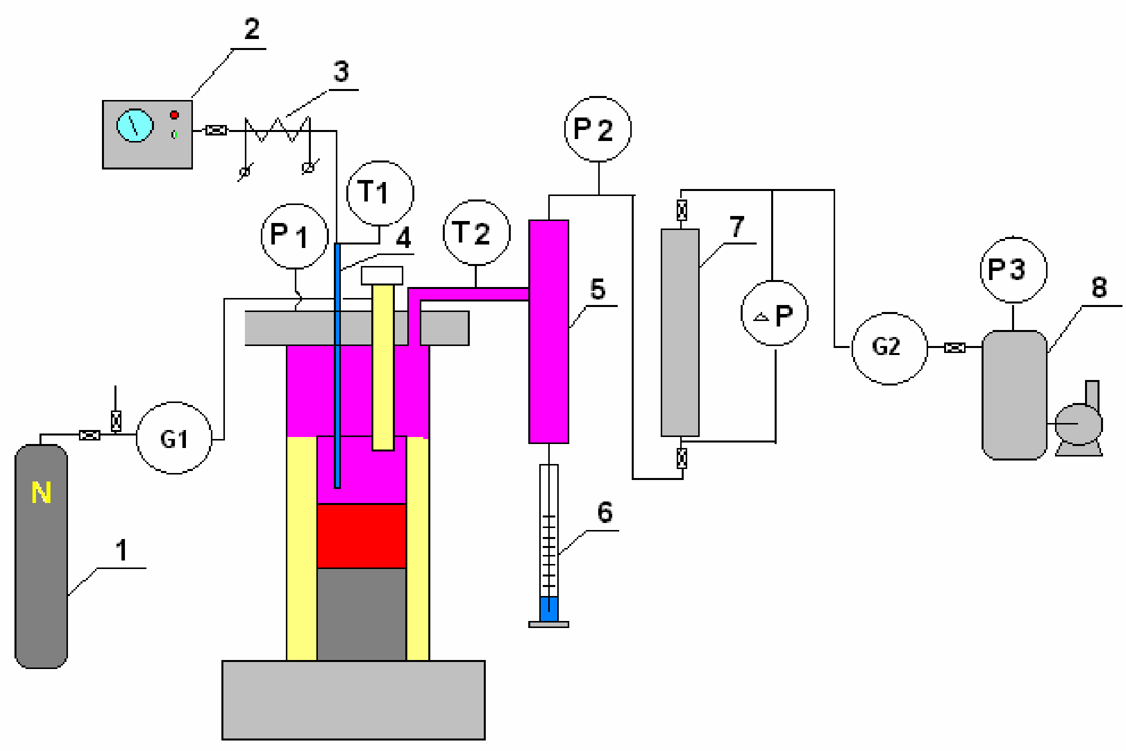

1 – nitrogen cylinder; 2 – steam generator; 3 – heated steam pipe; 4 – steam supply quartz tube; 5 – steam condenser; 6 – condensate and aerosols collector; 7 – Petryanov Large Area Filter (LAF); 8 – vacuum pump; P1, P3 – pressure gauges; T1, T2 – L-type thermocouples; G1,2 – electromechanical flowmeters.

Fig. 1.3 – Gas and aerosols in and out diagram

1.1.2 Materials

The materials used in the test included 15Kh2NMFA-A vessel steel, urania, zirconia, metallic zirconium, and superheated steam. All metal oxides and metals have been checked for the main substance content. In addition, the powdered urania was checked by thermogravimetry and the oxygen/uranium ratio was found to equal 2.24. The composition of corium charge is given in Tab. 1.2.

Table 1.2 – Corium charge composition

Component	Main substance content, %	Impurities, %	Notes
$UO_{2.24}$	> 99.9	Fe < 0.03; As < 0.0003; Cu < 0.01; phosphates < 0.002; chlorides < 0.003	Certificate data; thermogravimetry
ZrO_2	(ZrO_2+ HfO_2) > 99.4	Al_2O_3 < 0.03; Fe_2O_3 < 0.05; CaO < 0.03; MgO < 0.02; SiO_2 < 0.2; TiO_2 < 0.1; P_2O_5 < 0.15; (Na_2O+K_2O) < 0.02	Certificate data
Zr, Нб-1 alloy	Zr>99.0	Nb < 1.0	XRF

The procedure of crucible loading with the charge was as follows: a layer of crust imitator, i.e. C-100 corium (60% UO_{2+x}; 40% ZrO_2) (mass % here and further in text), with particles dispersivity below 50 µm, fused in steam in a specially performed Pr-MC10 test, was placed on the steel specimen top. Then a mixture of powdered $UO_{2.24}$ and ZrO_2 of C-100 composition was placed. Metallic Zr was used as the start-up material. The composition and masses of substances loaded into the crucible before melting are given in Tab. 1.3.

Table 1.3 – Charge components composition and mass

Purpose	Component	Fraction, µm	Mass, g
Crust imitator	C-100 corium (60% UO_{2+x}; 40% ZrO_2)	< 50	152.0
Main charge	Urania, $UO_{2.24}$	< 100	1115.8
	Zirconia, ZrO_2	< 100	435.7
	Metallic zirconium, Zr	Rods Ø 3 mm, h = 15 mm	10.1
Total:			1713.6

1.1.3 Experimental procedure

The start-up heating and molten pool formation in air were done at Z_c=20 mm and Ze=10 mm (Fig. 1.1). At 1100 s the molten pool surface temperature was about 2600°C, while at the specimen top it was only 500-600 °C. In order to increase the specimen surface temperature, anode voltage of the generator valve was regulated and the crucible and electromagnetic screen shifted. The final positions of the screen and crucible were Z_e=20 mm and Z_c=0 mm. Further on, the Z_e and Z_c coordinates were kept fixed and temperature at the specimen top was changed by varying anode voltage of the generator valve.

At 4400 s, the molten pool depth and bottom crust thickness were found to be 56 and 2 mm, respectively. The melt surface temperature was 2760 °C, and the temperature at the specimen top reached 975 °C according to TC01 thermocouple. From 4630 s on, feeding of the superheated steam to the above-melt space of the cold crucible was started at 300 g/h. In accordance with the test plan, from that moment the vessel steel ablation kinetics at the interaction with corium through the crust was studied during 1.7 hours in steam above the melt at ~1000 °C maintained at the specimen top.

An increased formation of aerosols and clogging of the gas-aerosol line at transiting to the steam atmosphere was indicated by temperature of the steam-gas mixture at the outlet from the above-melt space of the cold crucible (Fig. 1.8). That is why the rate of steam supply to the furnace was raised up to 400 g/h at 9650 s.

At 10800 s temperature regime #2 was started; it lasted for ~ 1.5 hours during which the temperature at the specimen top was maintained at ~ 1180 °C. At 16275 s temperature regime #3 (1.1 hours, ~1230 °C at the specimen top) was started. When attempting to enter the next temperature regime with a still higher temperature of the specimen top, the specimen melting began and the test was terminated. The melt was crystallized and the specimen cooled in steam.

Throughout the test, the generator regime was adjusted according to the TC01 thermocouple readings, the hot junction of which was right at the specimen top, as well as according to temperature at the specimen top evaluated from readings of the lower thermocouples in the case of higher thermocouples malfunction.

During the regimes of stabilized temperature at the specimen top, additional control was made of:

- Steam pressure in the furnace;

- Pressure drop at LAF;
- Amount of condensate and aerosols in the steam condenser.

The loss of melt mass was compensated at 10500 and 16080 s by $UO_{2.67}$ powder in the amounts of 140 and 70 g, respectively. The furnace was blasted with nitrogen beforehand.

Fig.1.4 shows the history of anode voltage of the generator valve and of the signal proportionate to the inductor current. Fig.1.5 presents the history of heat fluxes to the crucible sections and inductor, as well as pool surface temperatures. It should be noted that no correct measurements of the molten pool surface temperature could be made after steam has been supplied into the furnace, because water steam absorbs the radiation within the operating wavelength range of the colour pyrometer. Fig. 1.6 shows the readings of thermocouples within the vessel steel specimen throughout the test. Instable readings of thermocouples in the specimen may be due to the instable status of the crust on the specimen top. Fig. 1.7 presents the history of heat fluxes into the specimen’s top and bottom calorimeters.

After cooling in steam, the specimen was extracted from the crucible together with the corium ingot. Integrity of the ingot could not be preserved during its extraction. Separate fragments of the ingot were embedded in epoxy and cut for the posttest analyses. The specimen was also cut along its central axis.

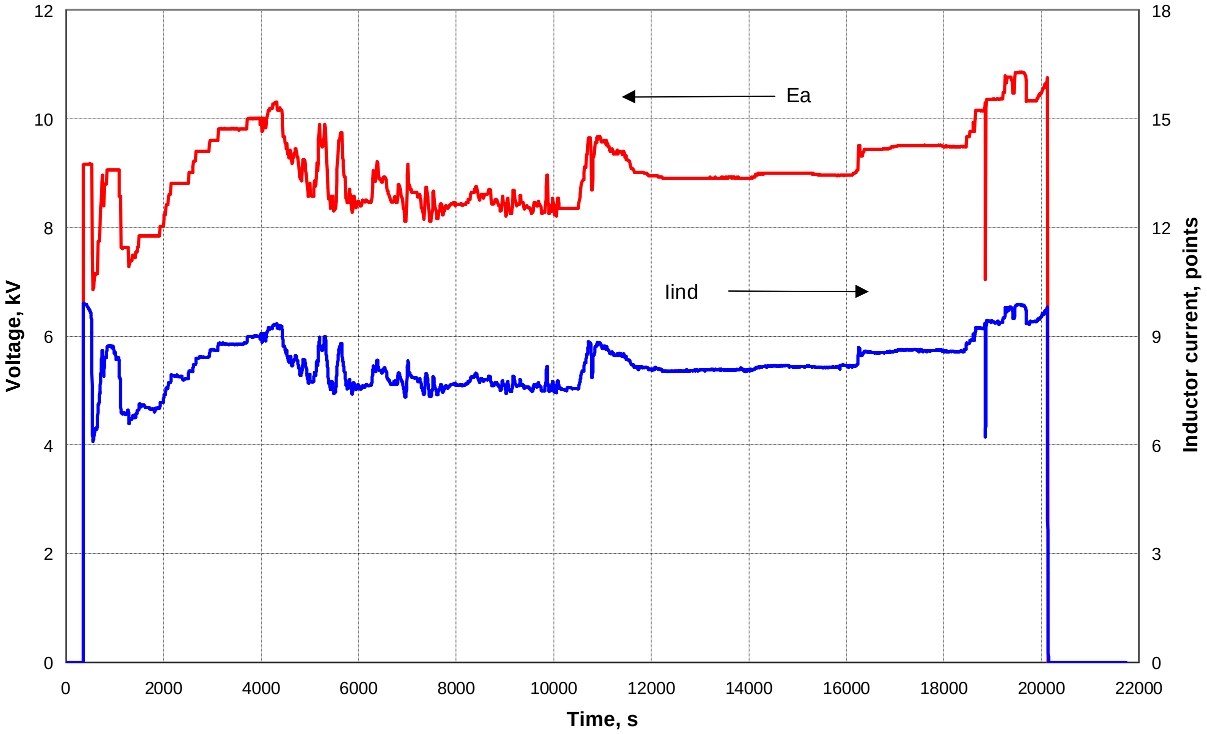

E_a – anode voltage of the generator valve; I_{ind} – signal proportionate to the inductor current

Fig. 1.4 – Anode current and voltage history

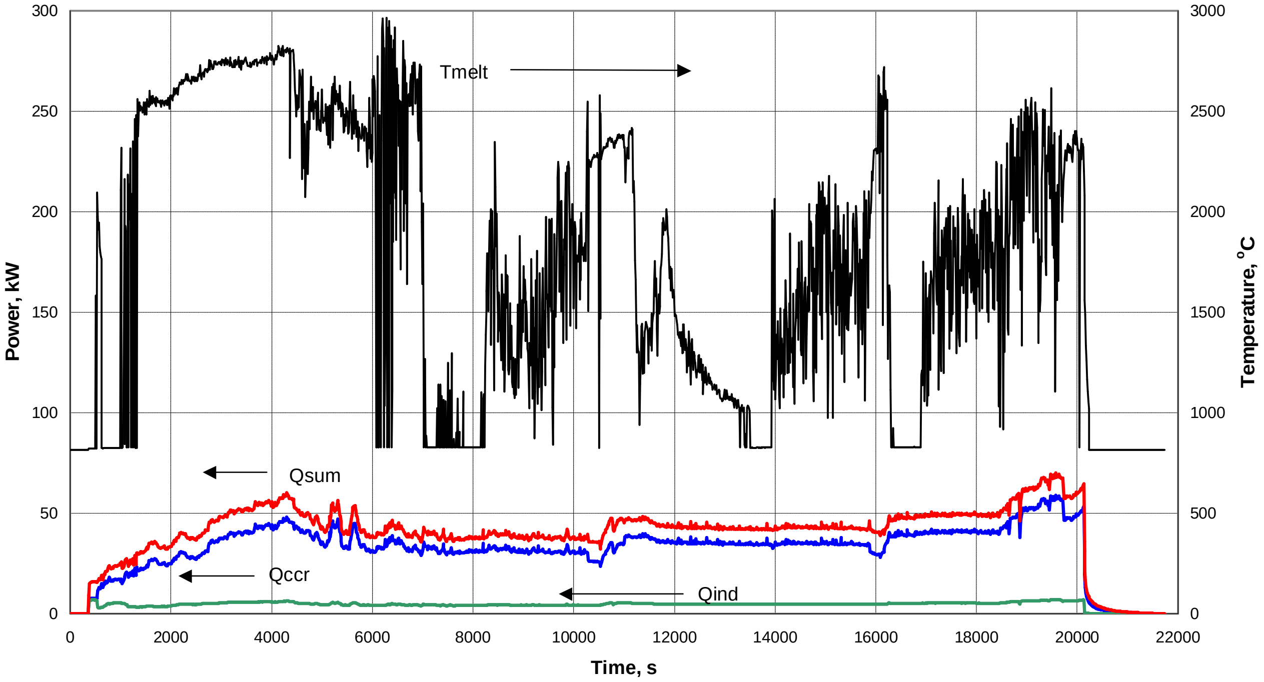

Q_{ccr} – power extracted into crucible sections; Q_{ind} – power extracted into inductor; Q_{sum} – power extracted into all water-cooled furnace components; T_{melt} – pyrometer readings

Fig. 1.5 – History of heat and electromagnetic fluxes, and of pyrometer readings

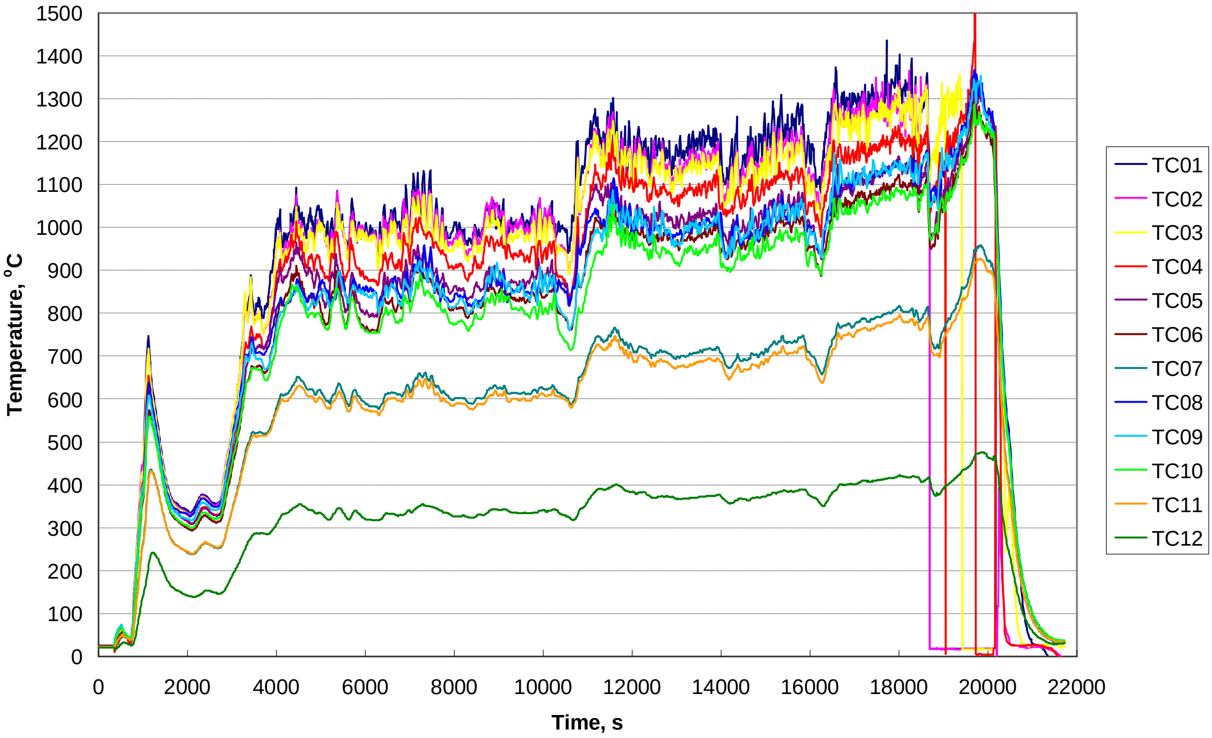

Fig. 1.6 – Thermocouple readings in MC10

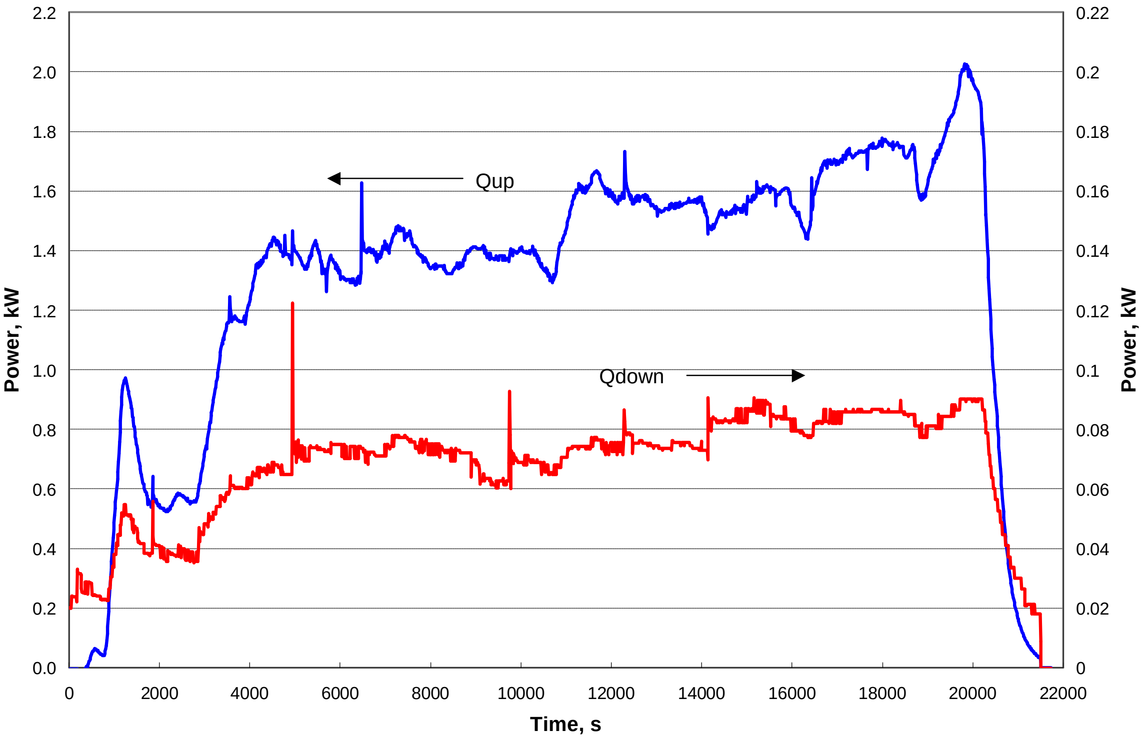

Q_{up} – heat flux to the top calorimeter; Q_{down} – heat flux to the bottom calorimeter

Fig. 1.7 – History of heat fluxes to the top and bottom calorimeters

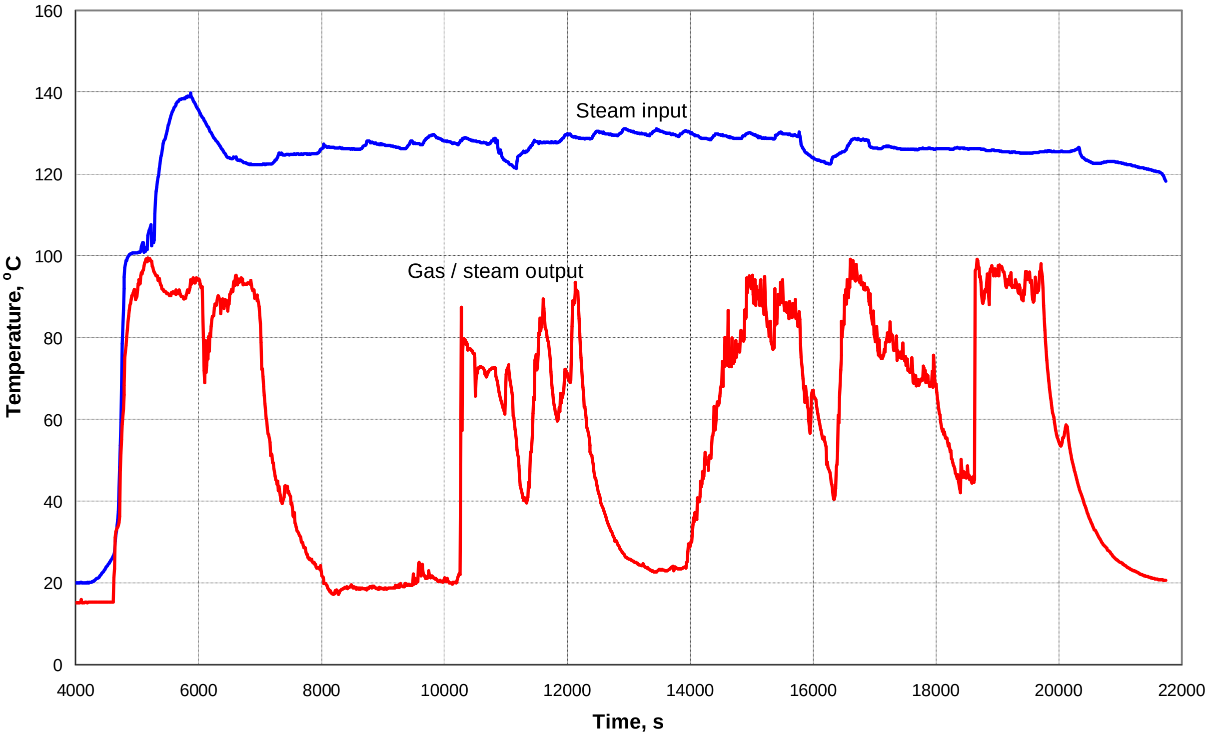

Fig. 1.8 – History of steam temperature at the inlet to the above the melt space of the cold crucible and of the steam-gas mixture temperature at the outlet from the above the melt space of the cold crucible

1.1.4 Ultrasonic measurements of the specimen corrosion

In MC10, the specimen corrosion was measured on-line. The mechanism of corrosion did not basically differ from that in MC1÷MC3 and the signal reflected from the interaction boundary (steel/crust) is the only signal reflected (excluding that one reflected from the defect), so, unlike in MC6÷MC9, there is no need in complicating the technique of signals processing by the echogram field analysis. Therefore, the only difference of the ‘true’ time profile of corrosion depth from the one measured on-line is a correction for the change in sound velocity in steel under the temperature change along the segment between the acoustic defect and the interaction boundary (front). The said temperature correction was obtained through approximation of the US measurements during the specimen heating without ablation. It is written as:

$$C_1(T) = 6{,}018 - 8 \cdot 10^{-5}T - 5{,}47 \cdot 10^{-7}T^2. \qquad (1.1)$$

Taking the mentioned correction into account, the distance from the interaction boundary to the acoustic defect is described by the expression:

$$D_1 = D_m \frac{C_1(T_S) + C_1(T_D)}{2C_0}, \qquad (1.2)$$

where D_m is the distance from the interaction boundary to the acoustic defect recorded in the test, mm;

C_0 is the sound velocity at room temperature, km/s;

C(T) is the sound velocity at temperature T, km/s;

T_S is the temperature at the interaction boundary, °C.

T_D, °C is directly measured by TC5 thermocouple, and the value of T_S is determined by interpolating readings of the thermocouples located above and below the corrosion front position at the current instant of time.

Tab. 1.4 contains the initial parameters used for determining the specimen corrosion rate, and Fig. 1.9 shows the history of corrosion depth in MC10.

A sharp increase in ablation rate was recorded at the final stage of MC10. It corresponded to a brief period of steel melting.

Table 1.4 – Initial values of main parameters

Parameter	Notation	Value	Unit	Note
Total specimen length	L	104.1	mm	
Distance from the defect to the 1st point of temperature measurement	l_1	-0.04	mm	6 mm from top
Distance from the defect to the 2nd point of temperature measurement	l_2	3.96	mm	2 mm from top
Temperature measured at the 1st point by TC05 thermocouple	T_1	variable	°C	6 mm from top
Temperature measured at the 2nd point by TC02 thermocouple	T_2	variable	°C	2 mm from top
Initial distance from the defect axis to top	D_o	6.25	mm	
Initial speed of sound in the specimen	C	6.018	km/s	

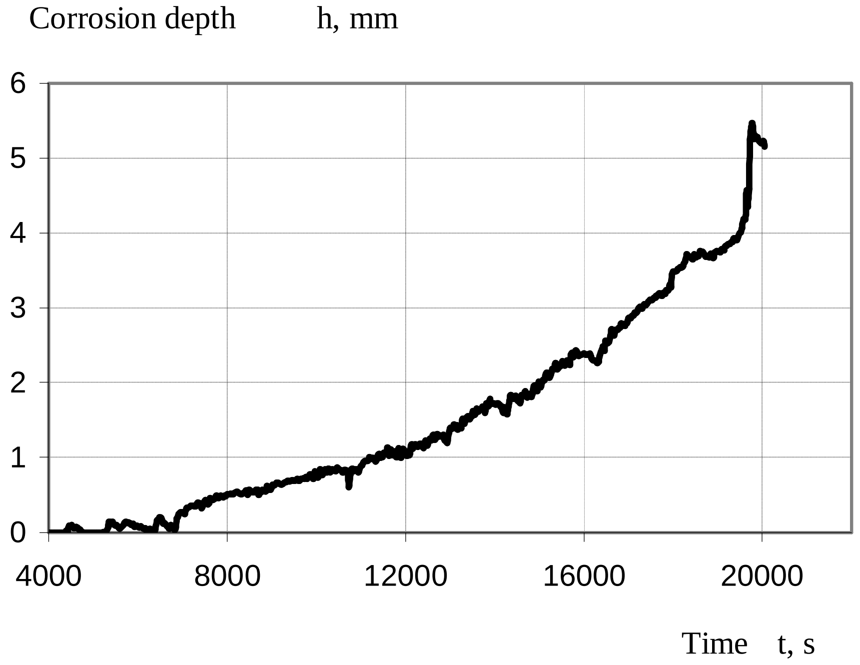

Fig. 1.9 – Specimen corrosion depth

The results of temperature measurements (Fig. 1.6) helped to specify time intervals of 3 regimes, and using the measured corrosion depths (Fig. 1.9) average values of corrosion rate were obtained for each regime:

Regime #1, from 4600 s through 10200 s – 0.55 mm/h.

Regime #2, from 11000 s through 15800 s – 1.07 mm/h.

Regime #3, from 16600 s through 18600 s – 2.07 mm/h.

1.2 Posttest analysis

The necessity of a posttest analysis is determined by the following circumstances. The experimentally obtained data on corrosion kinetics should be brought into correlation with a combination of parameters that govern the said process. First of all, it relates to the specimen surface temperature. The discrete thermocouple measurements directly in the specimen do not allow determination of the temperature at the surface and can be used as reference points only in numerical modeling of the specimen temperature condition. The numerical modeling requires a preliminary determination of how density of the heat flux from the melt distributes along the specimen top radius. For this purpose, calculations of melt thermal hydrodynamics were performed, which, in their turn, required a numerical analysis of the entire electromagnetic system.

In addition to the said calculations, a broad complex of physicochemical and metallographic analyses has been performed. They were aimed at 1) determining, specifying or confirming the compositions participating in the interaction of materials (initial and final ones), 2) checking material balances that would confirm reliability of the obtained data, 3) identifying the additional effects that accompany the main process in question (i.e., vessel steel corrosion), – and finally getting an insight into the nature and mechanism of corrosion. The indicated aims explain the apparent redundancy of the performed analyses. Omitting any of them might have lead to a loss of potentially valuable data.

1.2.1 Calculation of the induction system electromagnetic parameters

Fig. 1.10 shows an electromagnetic system diagram which includes inductor, cold crucible with sections and collector, vessel steel specimen, molten corium, furnace cover, electromagnetic screens and pyrometer shaft.

The electromagnetic problem solution yields integral parameters of the induction system, distribution of heat sources and Lorentz forces in molten corium, and distribution of heat sources in the specimen in general.

Due to the lack of reliable data on specific resistance of molten corium with the composition in question, an inverse problem was solved, an argument of which was the volume-averaged specific resistance of the melt. To ensure determination or over determination of the system, the other input parameters were the inductor voltage and power, as well as the total power in the melt and cold crucible. Thus, solving of the inverse problem was based on the functional minimization, a parametric function of which was the electromagnetic field equation with regard to the accepted limitations and input parameters, and a necessity of observing the following relation:

$$Q_{ccr} + Q_{cov} + Q_{sh} + Q_{sp} = Q_{spe} + Q_{ccre} + Q_{Melt} + Q_{cove} + Q_{she}, \qquad (1.3)$$

where Q_{ccr} – is the total power removed from the crucible;
Q_{cov} – the total power removed from the cover;
Q_{sh} – the total power removed from the shaft;
Q_{sp} – the total power removed from the specimen;
Q_{spe} – the power induced in the specimen;
Q_{ccre} – the power induced in the crucible;
Q_{Melt} – is the power in the melt;
Q_{cove} – the power induced in the cover;
Q_{she} – the power induced in the shaft.

The results of numerical analysis were obtained using the software tools described in [5].

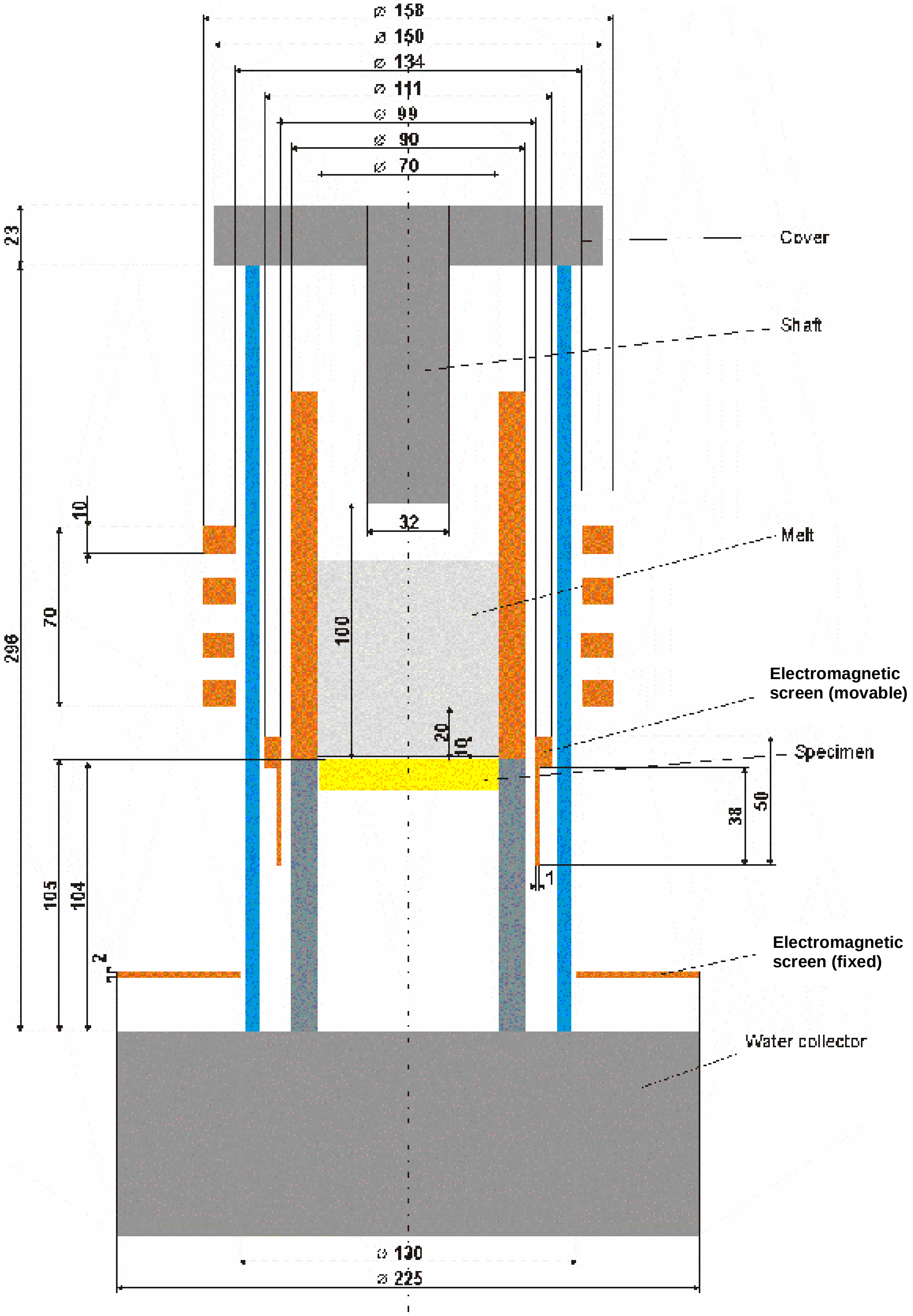

Fig. 1.10 – Electromagnetic system diagram

Tab. 1.5 contains the experimental and calculated data for two regimes of MC10 which correspond to different temperature conditions of the specimen, where a_2 is the molten pool depth, ξ is the bottom crust thickness, ρ_2 is the volume-averaged specific resistance of the melt.

The finite-element grid in the molten pool and in the vessel steel specimen is shown in Fig. 1.11.

Table 1.5 – Results of calculations

Time, s	**a_2, mm**	**x, mm**	**Q_{ccr}, kW**	**Q_{cov}, kW**	**Q_{sh}, kW**	**Q_{sp}, kW**	**Q_{spe}, kW**	**Q_{ccre}, kW**	**Q_{melt}, kW**	**Q_{cove}, kW**	**Q_{she}, kW**	**ρ_2, ohm-cm**
	Test						Calculated					
4600-10200	56.0	2.0	31.4	0.62	0.45	1.44	0.019	2.07	**31.730**	0.01	0.081	**3.00×10^{-2}**
11000-15800	56.0	2.0	35.6	0.61	0.57	1.63	0.023	2.32	**35.967**	0.01	0.090	**3.15×10^{-2}**

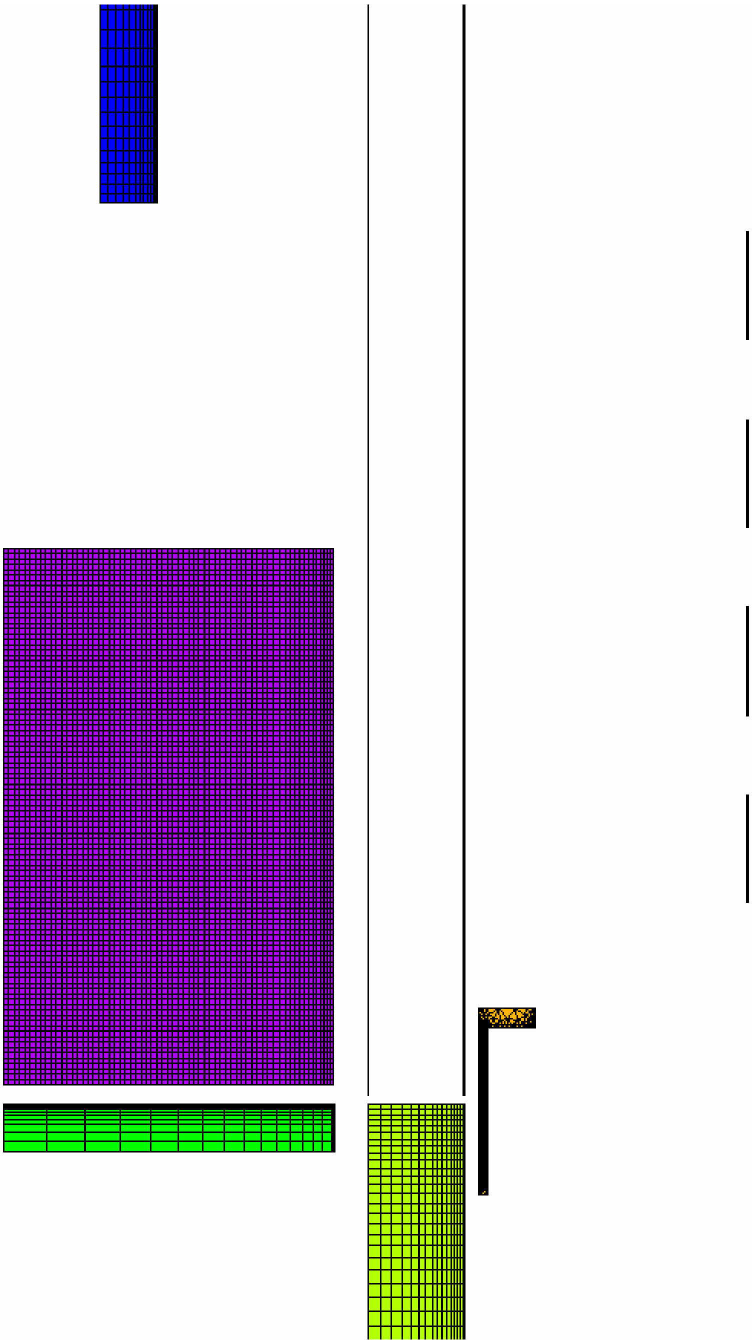

Fig. 1.11 – Finite-element grid of the computational domain

1.2.2 Thermal hydrodynamics of the molten pool

The solution found in Sect. 1.2.1 for the electromagnetic system determines the distribution of heat sources and Lorentz forces in the melt, formation of crusts at the molten pool boundaries is not taken into account. Therefore, the problem of melt thermal hydrodynamics is solved together with the electromagnetic problem, in which the total power in the melt and electrical conductivity of the melt are taken from the results of calculations in Sect. 1.2.1.

The model realized in the DYMELT software describes a 2D nonstationary axis-symmetrical motion of a nonisothermal viscous liquid in the field of gravitational and electromagnetic forces, with the volume heat source. The equations of motion, continuity and energy were written as:

$$c\frac{\partial u}{\partial t}+cu\frac{\partial u}{\partial r}+cv\frac{\partial u}{\partial z}=-\frac{\partial p}{\partial r}+\frac{1}{r}\frac{\partial}{\partial r}\left(\text{м}(T)\cdot r\frac{\partial u}{\partial r}\right)-\text{м}(T)\frac{u}{r^2}+\frac{\partial}{\partial z}\left(\text{м}(T)\frac{\partial u}{\partial z}\right)+f_r, \quad (1.4)$$

$$c\frac{\partial v}{\partial t}+cu\frac{\partial v}{\partial r}+cv\frac{\partial v}{\partial z}=-\frac{\partial p}{\partial z}+\frac{1}{r}\frac{\partial}{\partial r}\left(\text{м}(T)\cdot r\frac{\partial v}{\partial r}\right)+\frac{\partial}{\partial z}\left(\text{м}(T)\frac{\partial v}{\partial z}\right)-$$

$$-c_0\text{в}(T-T_0)g+f_v, \quad (1.5)$$

$$\frac{\partial u}{\partial r}+\frac{u}{r}+\frac{\partial v}{\partial z}=0\ , \quad (1.6)$$

$$cc\frac{\partial T}{\partial t}+cuc\frac{\partial T}{\partial r}+cvc\frac{\partial T}{\partial z}=\frac{1}{r}\frac{\partial}{\partial r}\left(\text{л}(T)\cdot r\frac{\partial T}{\partial r}\right)+\frac{\partial}{\partial z}\left(\text{л}(T)\frac{\partial T}{\partial z}\right)+W(r,z), \quad (1.7)$$

where t is time; r is radius; z is height; u, v are the radial and vertical components of velocity; T, ρ, p are temperature, density and pressure; β is the volumetric expansion coefficient; ρ_0 is density at a temperature T_0; μ is the dynamic viscosity coefficient; c is heat capacity; λ is thermal conductivity; g is the gravitational acceleration; f_r, f_v are the radial and vertical components of the Lorentz force; W is the power of volume heat release.

The discrete analogs of differential equations have been produced applying the finite volume method [6]. The Lorentz force and the volume heat source were calculated by the formulas

$$\bar{f}=\bar{J}\times\bar{B}=y\left(\bar{E}+\bar{V}\times\bar{B}\right)\times\bar{B}, \quad (1.8)$$

$$W=\bar{J}\cdot\bar{E}, \quad (1.9)$$

where $\bar{J}$ is the current density vector; $\bar{E}$ is the electric field vector; $\bar{B}$ is the magnetic inductance vector; $\bar{V}$ is the velocity vector.

The vector potential $\left(\bar{A}\right)$ was used for calculating the electric and magnetic fields intensity:

$$\bar{E}=-\frac{1}{c}\frac{\partial\bar{A}}{\partial t}-\text{grad}\,j\ , \quad (1.10)$$

$$\bar{H}=\text{rot}\bar{A}. \quad (1.11)$$

In the case of a sine field, the equation for amplitude of the vector potential is written as

$$\frac{1}{\mu}\left(\frac{\partial^2 \dot{A}}{\partial r^2}+\frac{1}{r}\frac{\partial \dot{A}}{\partial r}+\frac{\partial^2 \dot{A}}{\partial z^2}-\frac{\dot{A}}{r^2}\right)= j\sigma\omega\dot{A}\ , \tag{1.12}$$

and the volume heat source and electric field intensity are calculated using the formulas

$$W=\frac{1}{2}\sigma_r\omega^2\left|\dot{A}\right|^2\ , \tag{1.13}$$

$$\dot{E}=j\omega\dot{A}\ , \tag{1.14}$$

where $\dot{A}$ is amplitude of the vector potential; μ is magnetic permeability; ω is circular frequency; σ is electrical conductivity of the melt; j is the imaginary unit.

The problem algorithm is based on the iterative solution of a system of equations (1.4)÷(1.14). The crucible walls were assumed to be transparent for electromagnetic energy, and the inductor current was specified at a level that would ensure power in the melt according to the value calculated in Sect. 1.2.1. The value of electrical conductivity of the melt was taken from the same calculations.

Thermophysical properties of the melt.

- Corium type: C-100
- Liquidus/solidus temperature: $T_{L/S}$ =2550 °C
- Heat capacity: c = 540 J/kg
- Density

T, K	300	2973	3970
ρ, kg/m^3	8490	7410	6960

- Emissivity factor: $\varepsilon = 0.8$
- Fusion heat: $3.2\cdot10^5$ J/kg
- Thermal conductivity at $T < T_{L/S}$, [7]

T, K	300	1000	1500	2000	3000
λ, W/(m·K)	7.7	3.01	2.15	2.00	2.8

At $T > T_{L/S}$ – λ = 2.8 W/(m·K);

- Kinematic viscosity coefficient at $T > T_{L/S}$, [8].

T, C	2600	2650	2700	2750	2800
$\nu\cdot10^7$, m^2/s	9.49	8.83	7.37	7.66	6.83

For calculating the melt crust at T < $T_{L/S}$, an artificially overestimated viscosity value $\nu = 1.33 \cdot 10^{-2}$ m^2/s was specified.

- Electrical conductivity of the solid phase was accepted to be orders of magnitude lower than that of the liquid phase.

Specimen

- Density: $\rho = 7800$ kg/m^3
- Heat capacity: c = 600 J/kg
- Thermal conductivity

T, K	300	383	573	673	873	1073	1273	1673
λ, W/(m·K)	51	45	42	39	36	35	34	34

Lateral crust

- Density: $\rho = 6000$ kg/m^3
- Heat capacity: c = 540 J/kg
- Теплопроводность

T, K	273	473	873	1273	1673	2073
λ, W/(m·K)	0.414	0.414	0.605	0.805	1.119	1.61

Boundary conditions

Velocity. The condition of liquid adhesion on the crucible and specimen walls was set to be

$$u = v = 0. \tag{1.15}$$

Temperature. A condition of the 2nd kind was specified for the heat radiated from the melt free surface. Taking into account low temperature of the surrounding surfaces compared to the melt temperature, the condition is written as

$$\text{л}\frac{\partial T}{\partial n} = \text{ey}T^4, \tag{1.16}$$

where σ is the Stefan-Boltzmann constant.

The temperature boundary condition for the crucible water-cooled walls was formulated as in the calculations performed for MC4 and MC5, i.e. supposing a loose thermal contact between the crust and crucible. Across the gap, heat is transferred by both radiation and thermal conductivity. The corresponding boundary condition is written as

$$\text{л}\frac{\partial T}{\partial n} = \text{ey}\left(T^4 - T_W^4\right) + \text{б}\left(T - T_W\right), \tag{1.17}$$

where T_W is the crucible wall temperature, T is temperature of the corium crust surface facing the crucible, n is the normal to the surface, α is the effective heat transfer coefficient; according to MC4 and MC5, α was accepted to be 150 W/(m^2·K).

Results of calculations

Calculations have been performed for regime #1 (from 4600 through 10200 s) and #2 (from 11000 through 15800 s).

Fig.1.12 shows the computational domain geometry and distribution of the vector potential vertical component. Obviously, the electromagnetic field near the pool lower part is absorbed by the screen, and the maximum electromagnetic field penetration into the melt is observed in the upper peripheral region.

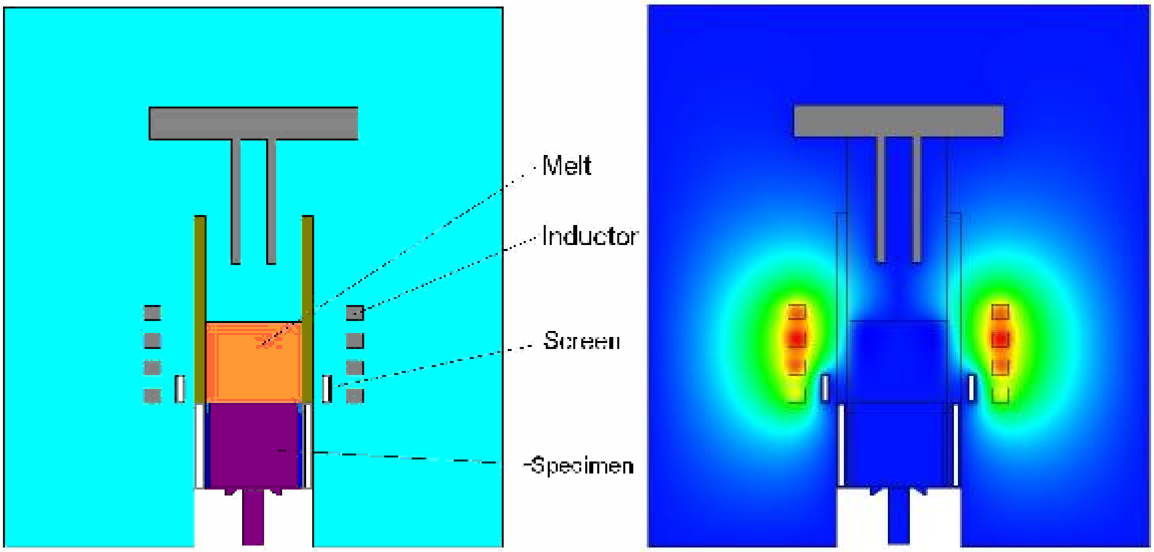

(a) (b)

Fig. 1.12 – Computational domain (a) and distribution of the vector potential vertical component (b)

Figs.1.13-1.14 illustrate the distribution of temperature (Kelvin scale) and velocity vector during regimes ##1, 2. The local minimum temperature of the free surface is seen to be near the pool axis, and in the pool central part the melt is moving downwards. The peak temperature of regime #2 is only 40 K higher than that of regime #1.

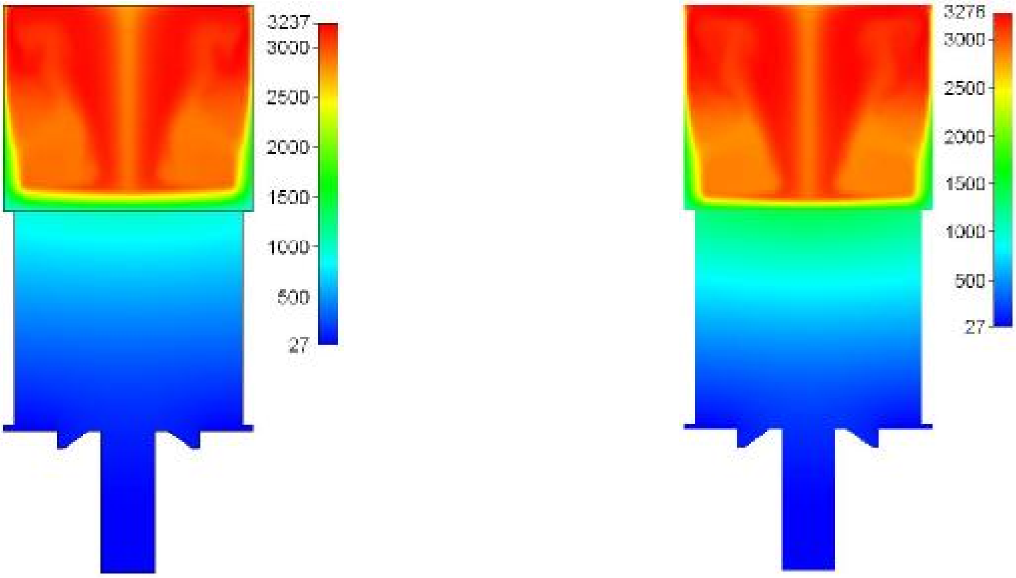

(a) (b)

Fig. 1.13 – Temperature distribution in the melt and specimen: (a) – regime#1; (b) – regime#2

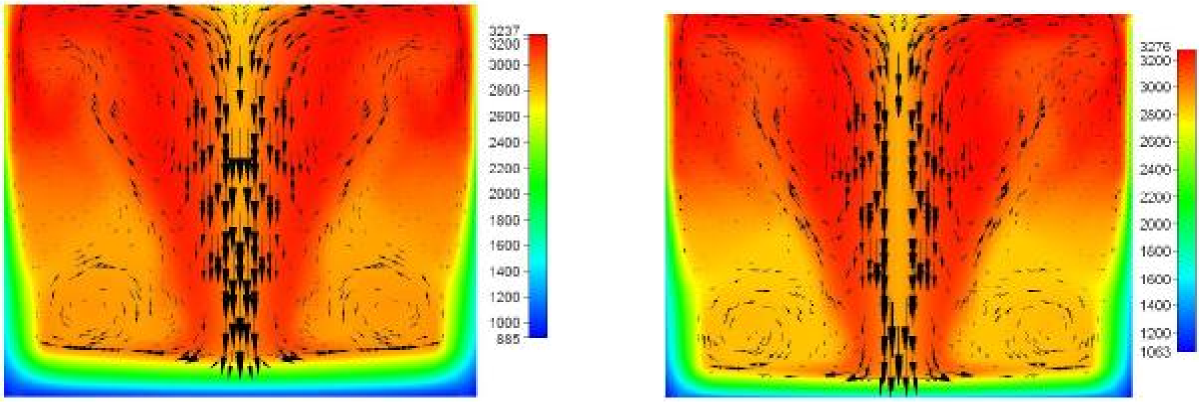

(a) (b)

Fig. 1.14 – Distribution of temperature and velocity vector in the melt: (a) – regime#1; (b) – regime#2

Fig. 1.15 depicts corium crust; during regime #2 it is approximately twice smaller that during regime #1. The lateral crust thickness is at its maximum in the pool bottom part and equals about 4 mm, it being the consequence of melt shielding by the electromagnetic screen.

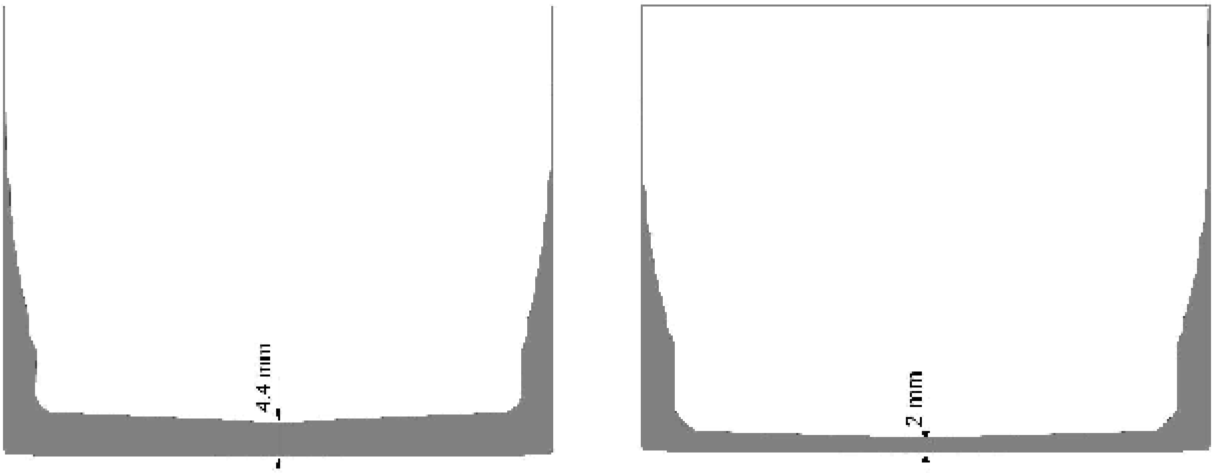

(a) (b)

Fig. 1.15 – Crust thickness: (a) – regime#1; (b) – regime#2

Fig.1.16 shows the radial distribution of heat flux density at the corium/specimen boundary. Mximum density is recorded for the central part.

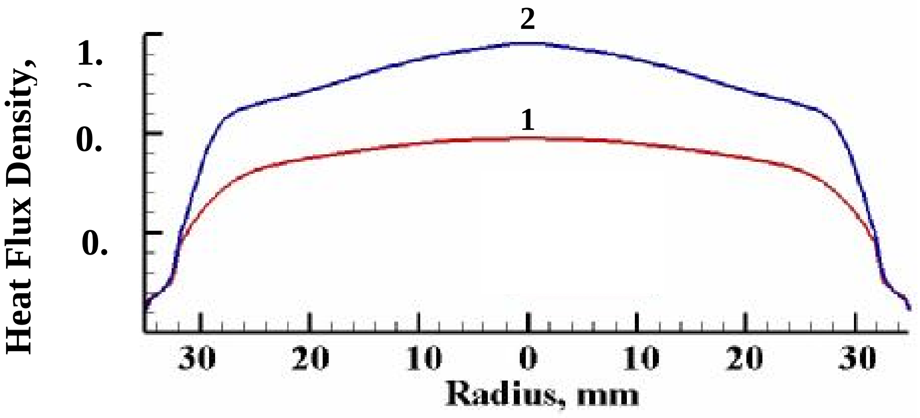

Fig.1.16 – Radial distribution of heat flux density at the specimen upper top, regimes ## 1 and №2

1.2.3 Temperature condition of the specimen

In order to determine steel corrosion conditions and to analyze experimental results, calculations of the specimen temperature conditions were performed in the same way as in the previously conducted tests. The calculations employed a finite-element program that implemented solution of a stationary thermal conductivity equation in the axis-symmetrical formulation. The specified boundary conditions were 1) the temperature on the inner surface of the top calorimeter (see Fig. 1.1.) estimated at 100°C (calculation results are practically insensitive to the insignificant error of its determination), 2) the temperature on the inner surface of the bottom calorimeter (20°C), and 3) the temperature on the outside surface of peripheral thermal insulation layer accepted as equal to the average temperature of cooling water. Thermal conductivity of 15Kh2NMFA-A steel, from which the specimen was produced, was taken from the results of the ISTC METCOR, Phase 1 Project. The heat flux density to the specimen top and thermal conductivity of the lateral insulation were varied in the calculations to provide the best agreement between the calculated and measured temperatures in the specimen at the locations of thermocouple junctions. The distribution of the incoming heat flux relative density along the radius of the specimen upper top was specified according to the melt thermal hydrodynamics calculated jointly with solving the electromagnetic problem (see Sect. 1.2.2). The said distribution was accepted to be the same in both regimes ##2 and 3.

Thermocouple readings have been averaged for each quasistationary regime (at each temperature plateau) within the following time intervals: #1 – from ~ 4600 through ~ 10000 s; #2 – from ~ 11000 through ~ 15800 s; #3 – from ~ 16500 through ~ 18500 s.

Fig. 1.17 a), b), c) illustrates a comparison of the calculated and experimental temperature values which confirm the acceptable accuracy of the calculations. An example of the calculated temperature field in the specimen upper part during regime #1 is shown in Fig. 1.18. The corrosion front position (as seen in the ∅15 mm spot of the US sensor) in the beginning and the end of a temperature plateau was marked in the temperature field for each regime according to Fig 1.9, and the regime-defining temperature values were accepted for the front middle position.

The temperatures and heat flux densities obtained as described above, as well as the calculated and experimental values of power into the specimen top calorimeter are summarized in Tab. 1.6.

Table 1.6 – Temperature and thermal parameters of the specimen

Regime No	Temperature at the ablation front, °C	Heat flux density at the ablation front, MW/m^2	Power into the top calorimeter, kW	
			Calculated	Test
1	1035	0.95	1.37	1.38
2	1185	1.05	1.56	1.58
3	1235	1.10	1.70	1.73

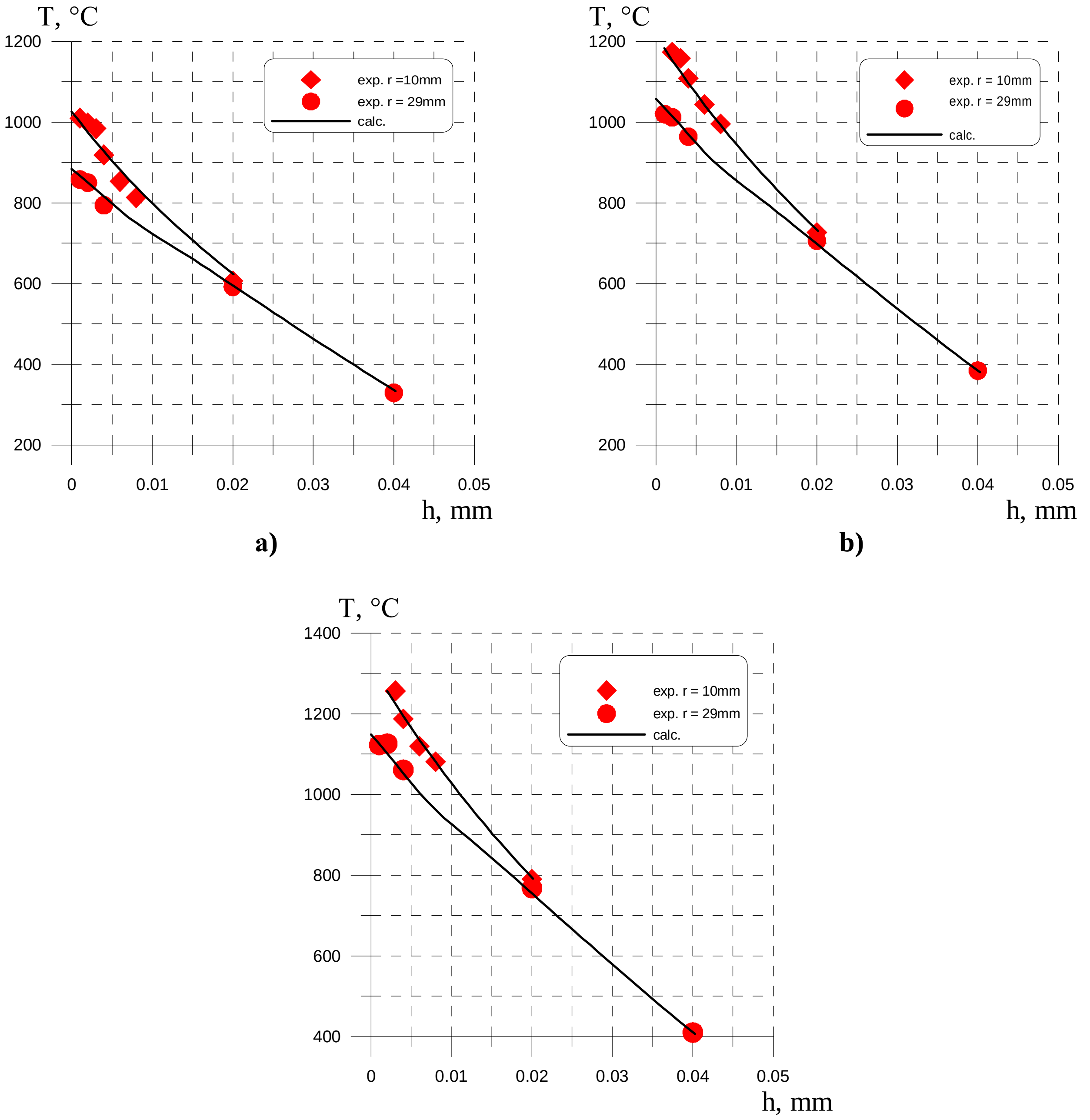

a)

b)

c)

a) – regime #1; b) – regime #2; c) – regime #3

Fig. 1.17 – Axial distribution of temperature in the specimen

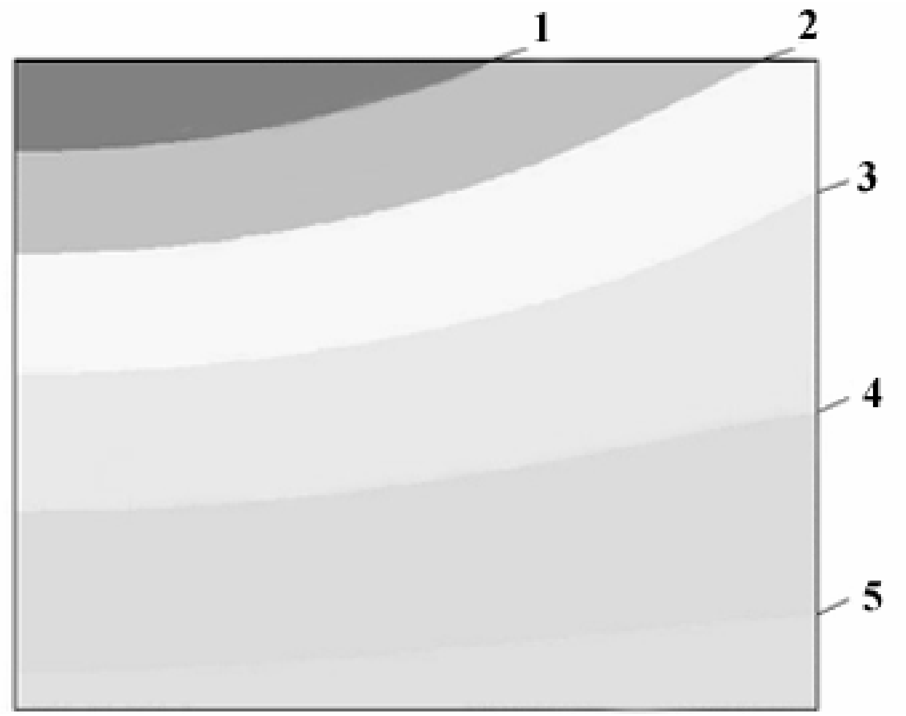

1 – T=1000°C; 2 – T=900°C; 3 – T=800°C; 4 – T=700°C;
5 – T=600°C

Fig. 1.18 – Temperature field in the specimen. Regime # 1

1.2.4 Physicochemical analysis

1.2.4.1 Ingot macrostructure

When disassembling the furnace after MC10, the crucible sections were found to be coated with aerosols (see. Fig. 1.19). The mass of aerosol deposits collected from the crucible sections amounted to 194.2 g. The mass of the crust above the crystallized ingot surface was 35.5 g.

The extraction of corium ingot and steel specimen from the crucible resulted in separation of the oxidic ingot from the metallic specimen and partial destruction of the former. The oxidic ingot was later reconstructed and position of the oxidic ingot relative to the steel specimen determined. A fragment of the oxidic ingot and steel specimen were embedded in epoxy and then used for templates preparation for the SEM/EDX. Fig. 1.20 shows the pattern of templates cutting from the oxidic ingot and steel specimen, and the steel specimen longitudinal section with the ablation boundary.

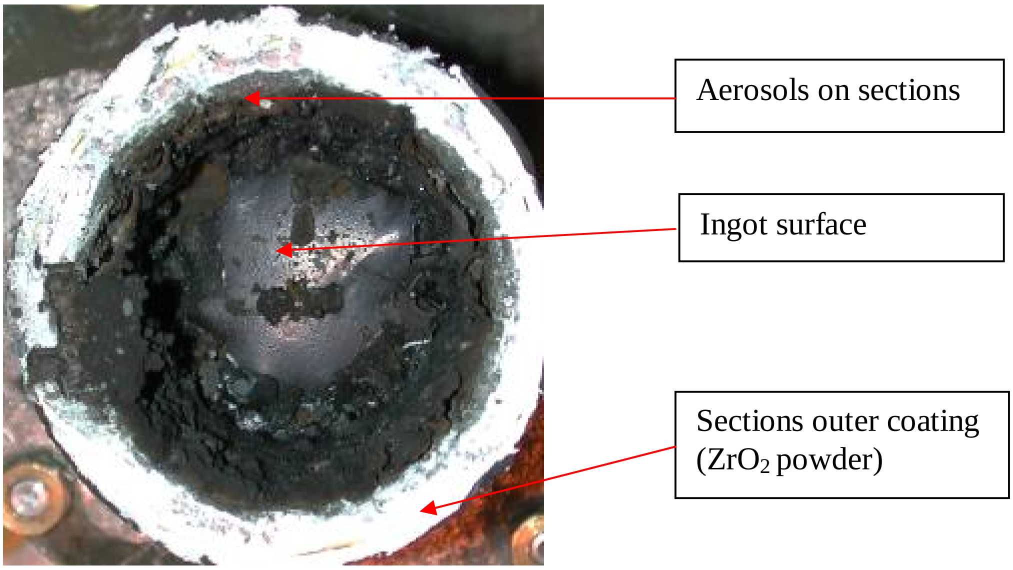

Fig. 1.19 – Ingot surface and aerosol deposits on the crucible sections

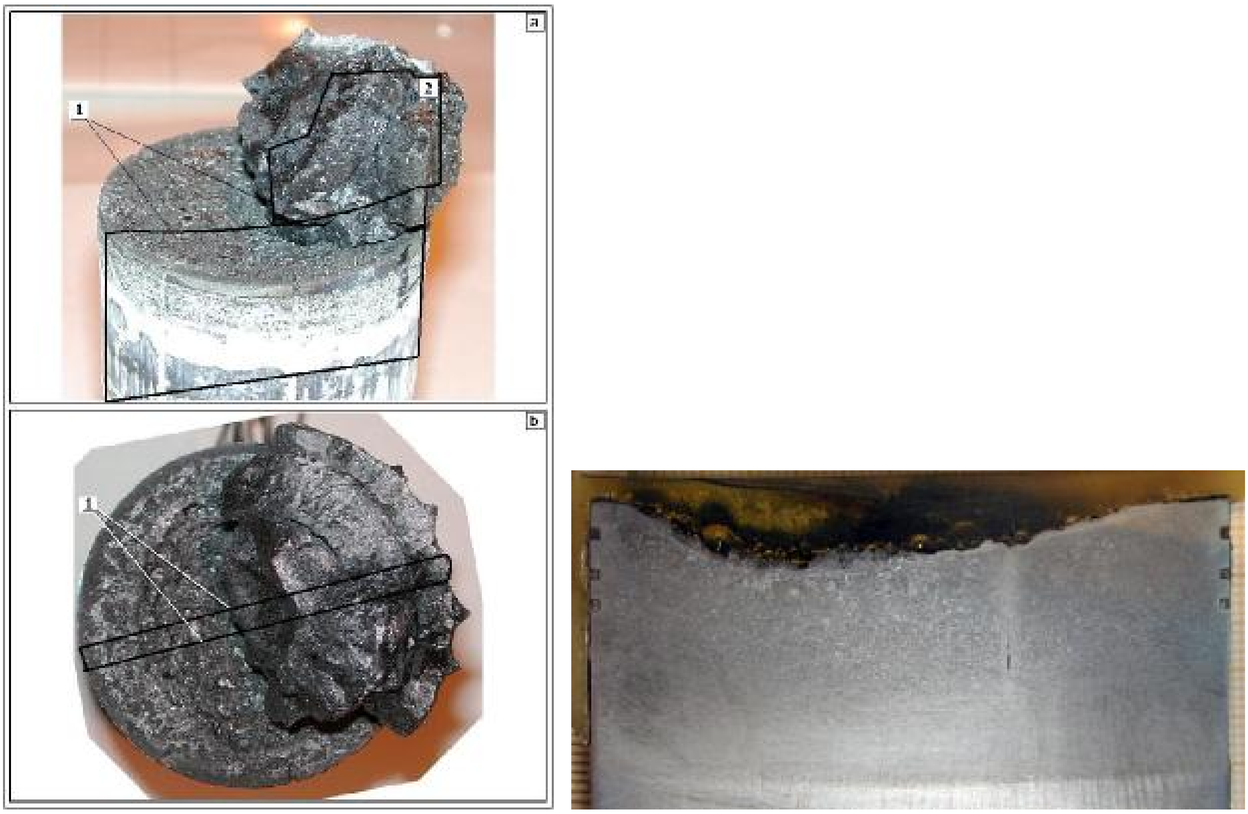

Fig. 1.20 – Pattern of templates cutting from the oxidic ingot and steel specimen. Steel specimen longitudinal section

1.2.4.2 Material balance of MC10

In order to make the material balance, the initial charge components and fused products were weighed with accuracy up to 0.1 g and then analyzed for the content of main components.

Material balance of components in MC10 is given in Tab. 1.7.

Table 1.7 – MC10 material balance

Introduced into the melt, g		Collected after the test, g	
$UO_{2.24}$	1115.8	Rod sample	2.6
ZrO_2	435.7	Crust	35.5
metallic Zr	10.1	Ingot	1369.7
Crust* (from Pr- MC10)- <50 µm fraction	152.0	Аэрозоли	523.9
Addition #1 (U_3O_8)	140.0		
Addition #2 (U_3O_8)	70.0		
Σ	**1923.6**	Σ	**1931.7**
Debalance		**+8.1**	

*) Corium, fused in steam in Pr-MC10 pretest, was used as the crust. Crust composition according to the physicochemical analysis is given in Tab. 1.8.

Table 1.8 – Physicochemical analysis of an average sample from the ingot produced in Pr-MC10

Determination method	**XRF**			**Chemical analysis**	
Element	**U**	**Zr**	**Impurities and O**[1]	U^{+4}	U^{+6}
	mass %				
Ingot average sample	51.0	30.8	18.2	42.0	10.2

[1] - from residue.

1.2.4.3 Chemical analysis of the fused products from MC10

The corium ingot, except the templates for the SEM/EDX, was crushed, and an average sample was taken by quartering. The aerosol deposits from the crucible sections and quartz tube were screened through a sieve with 50 µm mesh for separating melt splashes from aerosols. The dispersed fractions were weighed and average samples were taken by quartering.

The content of Fe(II) and Fe(III) was determined by photocolorimetry with orthophenanthroline [12-14]. The range of identified iron concentrations is 0.4-400 mg/dm^3. The total relative error of the method does not exceed ±3%, provided the measured optical densities are within 0.2-0.6 range.

Determination of U^{+4}, U^{+6} with arsenazo III was done according to technique [10, 11]. The results of chemical analysis of the fused products are given in Tab. 1.9.

Table 1.9 – **Chemical analysis of the fused products from MC10**

Sample	**Content, mass %**	
	U	**Fe**
Corium ingot average sample	62.7 (U^{4+} -58.0, U^{6+} -4.7)	3.2
Rod sample	62.0 (U^{4+} -51.0, U^{6+} -11.0)	<0.1
Aerosols from crucible sections (> 50 µm fraction)	67.2 (U^{4+} -67.2, U^{6+} - not detected)	not detected
Aerosols from crucible sections (< 50 µm fraction)	70.9 (U^{4+} -67.3, U^{6+} -3.6)	not detected
Aerosols from quartz tube (> 50 µm fraction)	73.1 (U^{4+} -73.1, U^{6+} - not detected)	not detected
Aerosols from quartz tube (< 50 µm fraction)	69.2 (U^{4+} -69.2, U^{6+} - not detected)	not detected
Aerosols condensed with steam #1	84.7 (U^{4+} -39.5, U^{6+} -45.2)	not detected
Aerosols from LAF-1 (air)	84.5 (U^{4+} -22.4, U^{6+} -62.1)	not detected

The analysis of the obtained results (see Tab. 1.9) shows that the aerosols from the crucible sections and quartz tube (> 50 µm fraction) contained no U^{6+}, while in the finer aerosols (< 50 µm fraction) U^{6+} was found in small quantities. Apparently, the hydrogen forming at the water steam thermolysis restores U^{6+} to U^{4+}.

1.2.4.4 XRF of the fused products from MC10

The elemental composition of the fused products was determined by XRF using the SPECTROSCAN MAX-GV spectrometer [9]. Tab. 1.10 contains the XRF results and per-element mass balances, as the most comprehensive analysis for all elements has been performed by this method.

Table 1.10 – XRF results for the fused products and per-element mass balance for MC10

Sample	U	Zr	Fe	O1)	Fused product mass, g	U	Zr	Fe	O1)
	mass %					g			
Ingot average sample	58.6	22.7	1.9	16.8	1369.7	817.7	317.8	26.0	208.2
Crust	61.4	21.8	2.5	14.3	35.5	21.8	7.7	0.9	5.1
Aerosols from crucible sections (> 50 µm fraction)	66.4	17.0	1.3	15.3	200.0	132.8	34.0	2.6	30.6
Aerosols from crucible sections (< 50 µm fraction)	70.1	12.1	1.1	16.7	32.9	23.1	4.0	0.4	5.5
Aerosols from quartz tube (> 50 µm fraction)	71.5	12.8	1.0	14.7	47.7	34.1	6.1	0.5	7.0
Aerosols from quartz tube (< 50 µm fraction)	64.7	19.8	0.3	15.2	11.7	7.6	2.3	0.0	1.8
Aerosols condensed with steam #1	79.1	0.1	0.1	20.7	7.8	6.2	0.0	0.0	1.6
Aerosols condensed with steam #2	82.3	0.1	0.1	17.5	6.2	5.1	0.0	0.0	1.1
Aerosols condensed with steam #3	82.3	0.1	0.3	17.3	6.9	5.7	0.0	0.0	1.2
Aerosols condensed with steam #4	83.5	0.1	0.7	15.7	5.1	4.3	0.0	0.0	0.8
Aerosols condensed with steam #5	84.4	0.1	0.3	15.2	84.4	71.2	0.1	0.3	12.8
Aerosols from LAF-1 (air)	81.0	0.1	0.1	18.8	39.0	31.6	0.0	0.0	7.3
Aerosols from LAF-II	83.2	0.1	0.1	16.6	65.1	54.2	0.1	0.1	10.8
Aerosols from LAF-III	85.0	0.1	0.1	14.8	8.6	7.3	0.0	0.0	1.3
Rod sample	61.5	21.3	-	17.2	2.6	1.6	0.6	0.0	0.4
Collected in the end of the test					1931.7	1214.3	367.9	30.8	318.6
Introduced into the melt					1923.6	1230.0	379.5	-	314.2
Δ					+8.1	-15.6	-11.6	+30.8	+4.5

1) - O and impurities determined from the residue.

From the mass balance for MC10 (Tab. 1.10) it may be seen that the mass difference between the introduced into the melt component and that collected in the end of the test (debalance) does not exceed 3%, it being within the accuracy limit for the applied analytical methods.

According to the profilogram (see Fig. 1.47) the calculated amount of iron transiting into molten corium equals approximately 38 g. An explanation of the insignificant deviation of the calculated mass from that determined by XRF (30.8 g) (see Tab. 1.10) may be the fact that the iron that exited steel was calculated on the basis of measurements made in one longitudinal section of the specimen only.

The difference in zirconium content in aerosols attracts attention. Significant amounts of zirconium found in all aerosols deposited in the furnace may possibly be explained by the melt droplets loss by the pool. The absence of zirconium in aerosols deposited in the condenser indicates the low pressure of its vapours under the test conditions.

The errors of the performed analyses are given in Tab. 1.11.

Table 1.11 –Analyses errors

Element	Error, % rel.	Detection method
U, Fe	5	Photocolorimetry
U, Zr, Fe		XRF

A comparison of the XRF and chemical analyses results of the main components in the fused products has shown them to be in satisfactory accord.

1.2.4.5 Density of fused corium from MC10

The bottle density of the fused corium average sample was determined according to the technique described in [15]. Ethyl alcohol was used as a picnometric liquid. The results of density determination under normal conditions are presented in Tab. 1.12.

Table 1.12 – Fused corium bottle density determination

Sample	Fused corium particle size, µm	Bottle density, g/cm^3
Ingot average sample	100-200	8.47
	<50	8.49

The density evaluation error was ± 0.02 g/cm^3.

A comparison of bottle densities of corium average samples from MC10 (<50 µm - 8.49 g/cm^3) and MC5 (C-100 corium, melting in an inert atmosphere, <50 µm - 8.65 g/cm^3), shows the density of ingot from MC10 to be lower than that of ingot from MC5. In the first place, this is explained by the fact that during melting in the oxidizing atmosphere formation of aerosols, the main part of which is represented by uranium oxides, proceeds at a much higher rate. The melt becomes depleted in uranium (MC10 – 58.6%, в MC5 – 64%), and hence density of the crystallized ingot decreases.

1.2.4.6 The SEM/EDX of corium and steel

<u>The SEM/EDX of corium from Pr-MC10 pretest</u>

Microstructure and elemental composition of templates from different zones of the ingot and vessel steel specimen after the interaction have been studied by Scanning Electron

Microscopy (SEM) Energy Dispersive X-ray Microanalysis (EDX). The findings are described below.

The limit of an element reliable detection depends on its atomic number in the periodic table and varies from 0.5 mass % for light elements to 0.3 mass % for heavy ones. Detection of smaller quantities would be unreliable. Oxygen content was determined using an oxygen-sensitive probe.

Depending on the electron beam energy and sample composition, the depth of electronic probe penetration varies from 1 to 5 µm. A microanalyzer detects radiation in a still thinner layer of ~1 µm. The zone of excitation by the probe is about 20 µm, it making fine phases hard to identify.

One template from Pr-MC10 has been prepared for determining bulk composition and that for each phase. The results of analysis are given in Figs. 1.22, 1.23 and in Tabs. 1.13, 1.14.

The SEM of images at x50 magnification has revealed layered microstructure of the ingot in question. (Fig. 1.22, region 1 and Fig. 1.23, region 3). At larger magnifications the microstructure looks highly textured and two uranium-based phases insignificantly differing by U:Zr ratio may be identified (Fig. 1.22, region 1-1-1, Tab. 1, points P1 and P2).

Decomposition of the $Zr_{1-x}U_xO_{2-\delta}$ solid solution into two solid solutions – $Zr_{1-x1}U_{x1}O_{2-\delta1}$ and $Zr_{1-x2}U_{x2}O_{2-\delta2}$ – insignificantly differing from each other in terms of composition (Tab. 1.13), may be supposed to follows the spinoidal mechanism in the solid phase, as it may be supposed on the basis of the SEM results (Fig. 1.22, region 1-1-1). However, the composition of solid solutions detected by the SEM/EDX significantly differs from those due to form in accordance with the available experimental data [16]. The said differences may be results from different reasons. Firstly, due to small size of the coexisting solid solutions, a mistake in determining their compositions could be due to the neighbouring solid solution capturing by the microprobe. Secondly, inaccuracy of data on the UO_2-ZrO_2 phase diagram given in [16] cannot be excluded. Another reason for the $Zr_{1-x}U_xO_{2-\delta}$ solid solution decomposition into solid solutions with the compositions given in Tab. 1.13 may be oxygen defectiveness of the initial solid solution (due to steam above the crystallizing melt) which decomposes into a somewhat urania-enriched, less oxygen-defective solid solution, and a zirconia-enriched, more oxygen-defective ($\delta_2>\delta>\delta_1$) solid solution. The SEM/EDX data may be referred to for confirming this hypothesis (see Tab. 1.13).

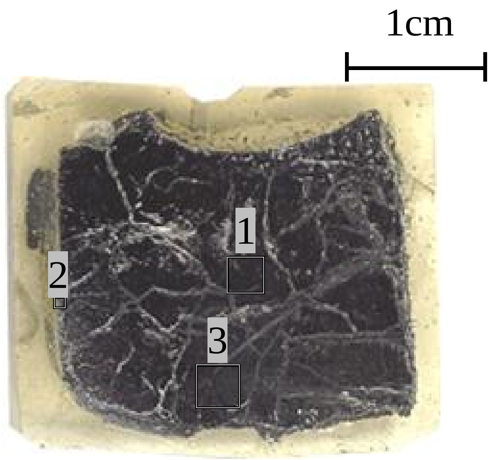

Fig.1.21 – Upper part (a) of the ingot longitudinal section with regions marked for the SEM/EDX. Pr-MC10 pretest

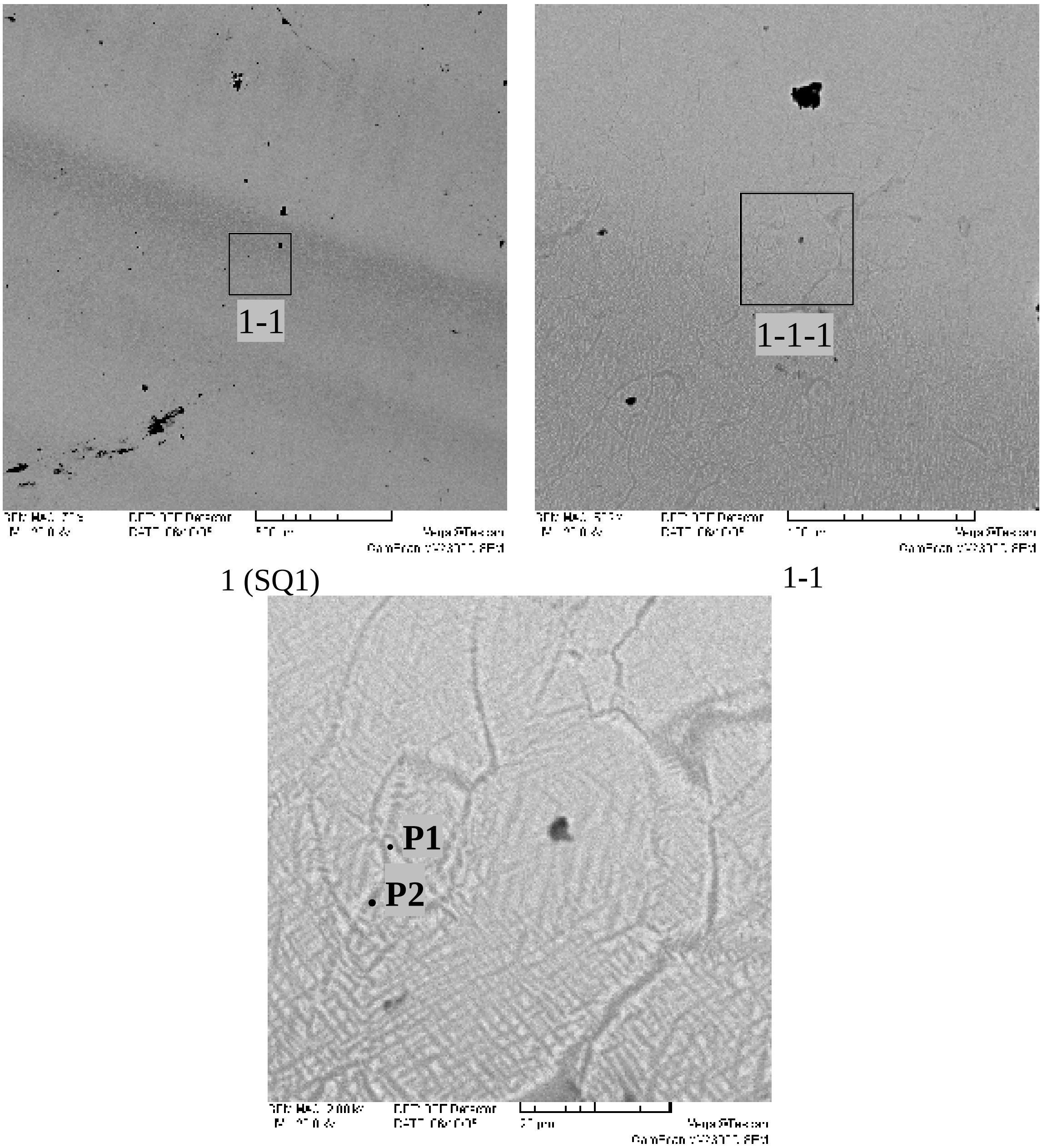

1 (SQ1)

1-1

1-1-1

Fig.1.22 – Micrographs of region 1

Table 1.13 – Data on region 1 EDX analysis

No		U	Zr	O
SQ1	mass %	50.16	32.69	17.15
	mol.%	12.84	21.84	65.32
	mol.% MeO_x	37.04	62.96	
P1	mass %	53.42	29.8	16.78
	mol.%	14.03	20.42	65.56
	mol.% MeO_x	40.72	59.28	
P2	mass %	46.75	35.61	17.64
	mol.%	11.63	23.11	65.27
	mol.% MeO_x	33.47	66.53	

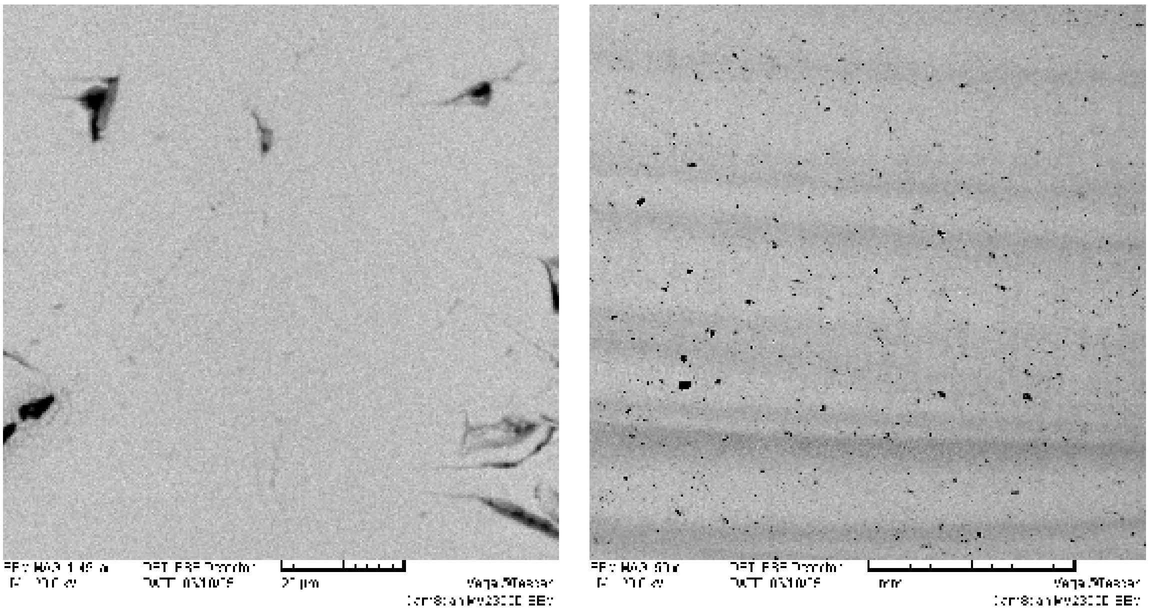

2 (SQ1) 3 (SQ2)

Fig.1.23 – Micrographs of regions 2 and 3

Table 1.14 – Data on regions 2 and 3 EDX analysis

No		**U**	**Zr**	**O**
SQ1	mass %	55.73	27.88	16.39
	mol.%	14.97	19.53	65.5
	mol.% MeO_x	43.38	56.62	
SQ2	mass %	51.73	31	17.27
	mol.%	13.28	20.76	65.96
	mol.% MeO_x	39.01	60.99	

The SEM/EDX of the corium/steel specimen interaction zone

Partial melting of the specimen occurred at the final stage of the test and lead to exit of a part of molten metal together with the formed interaction zone into the molten pool. During extraction of the specimen with ingot from the crucible, the ingot crumbled and separated from the specimen completely. Therefore, the SEM/EDX of the specimen (Figs. 1.24-1.30 and Tab. 1.15) yielded only the results of the molten pool temperature effect on the specimen. For instance, rounded FeO inclusions (P5 point, Tab. 1.15) were discovered regions 1 & 2 in metal to a depth of 0.1 mm. This supposes that this layer had melted and a two-phase area consisting of metallic and oxidic parts formed during melt cooling and settled during crystallization. Also, significant porosity of metal can be observed above this layer (Fig. 1.2.3), which may specify the carbon burning-out. Melt traces are observed in regions 2, 4 and 6 as inclusions in the metal (Figs. 1.26, 1.28, 1.30).

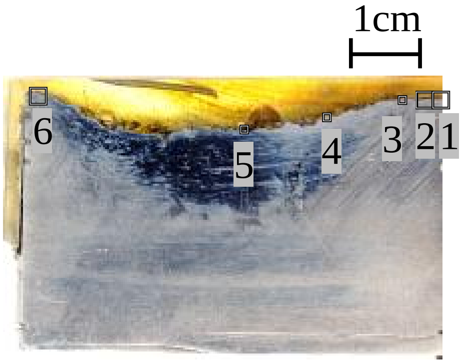

Fig. 1.24 – Longitudinal section of the metallic part of the ingot from MC10 c with regions marked for the SEM/EDX

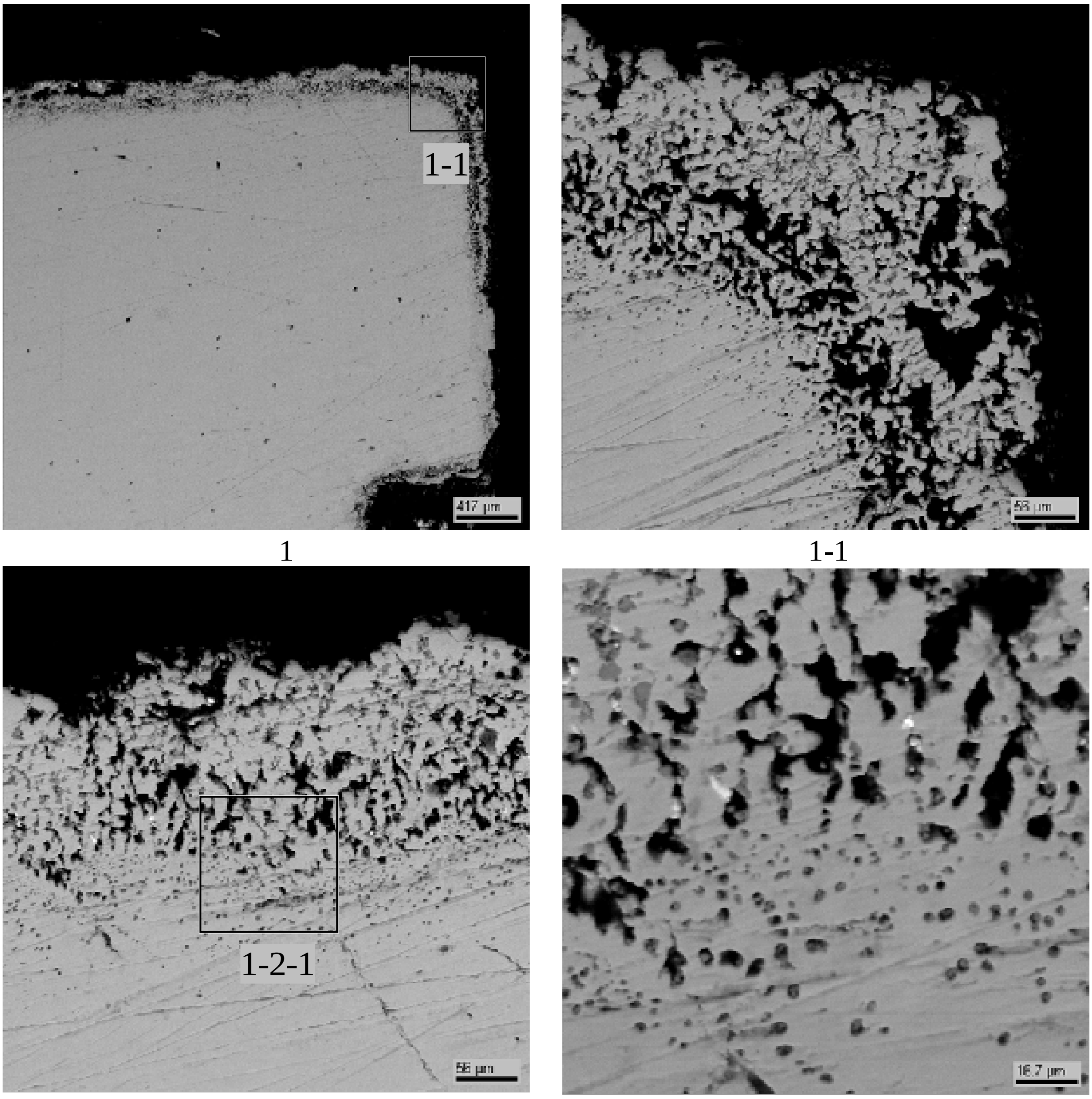

1 1-1

1-2 1-2-1

Fig. 1.25 – Micrographs of region 1

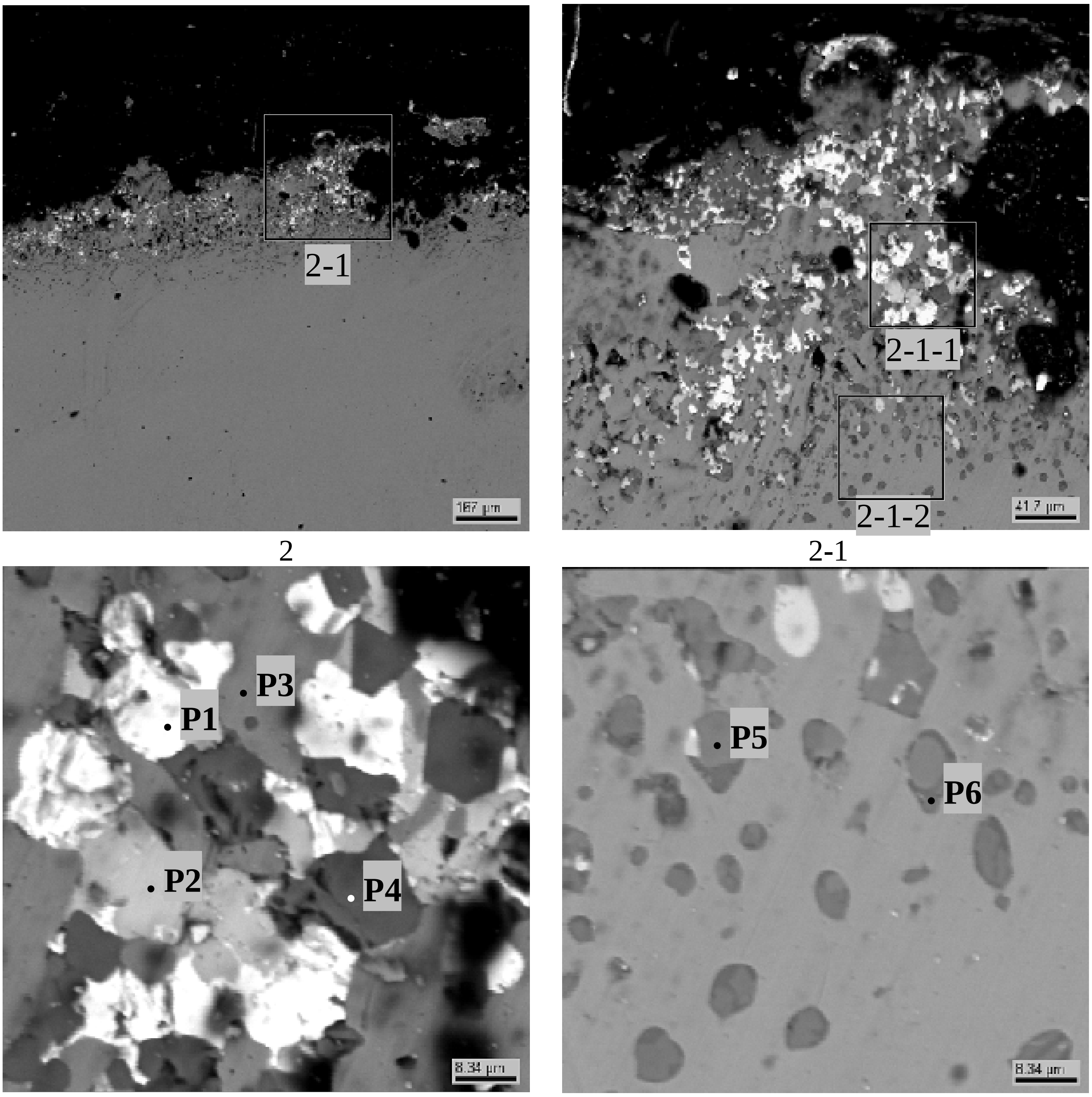

2 2-1

2-1-1 2-1-2

Fig. 1.26 – Micrographs of region 2

Table 1.15 – **Data on region 2 EDX analysis**

No		U	Zr	Fe	Cr	Ni	Mn	Mo	~O
P1	mass %	78.04	3.16	5.00	0.57	-	-	-	13.24
	mol.%	25.41	2.68	6.94	0.85	-	-	-	64.12
	mol.% MeO_x	70.82	7.47	19.33	2.37	-	-	-	
P2	mass %	34.20	30.27	8.11	0.52	-	0.29	-	26.61
	mol.%	6.25	14.43	6.31	0.44	-	0.23	-	72.34
	mol.% MeO_x	22.59	52.17	22.83	1.58	-	0.83	-	
P3	mass %	0.81	0.29	89.93	0.65	4.93	-	1.15	2.06
	mol.%	0.18	0.17	86.56	0.67	4.52	-	0.64	6.91
	mol.% MeO_x	0.20	0.18	92.98	0.72	4.85	-	0.69	
P4	mass %	0.80	1.60	36.11	27.91	-	0.72	2.20	30.47
	mol.%	0.11	0.56	20.51	17.03	-	0.41	0.73	60.43
	mol.% MeO_x	0.27	1.41	51.85	43.05	-	1.05	1.84	
P5	mass %	-	0.58	69.53	1.72	-	0.87	0.11	26.76
	mol.%	-	0.21	41.65	1.11	-	0.53	0.04	55.95
	mol.% MeO_x	-	0.48	94.55	2.51	-	1.20	0.09	
P6	mass %	0.17	1.63	50.43	0.52	-	2.30	-	30.34
	mol.%	0.02	0.53	26.63	0.29	-	1.24	-	55.94
	mol.% MeO_x	0.05	1.19	60.45	0.67	-	2.80	-	

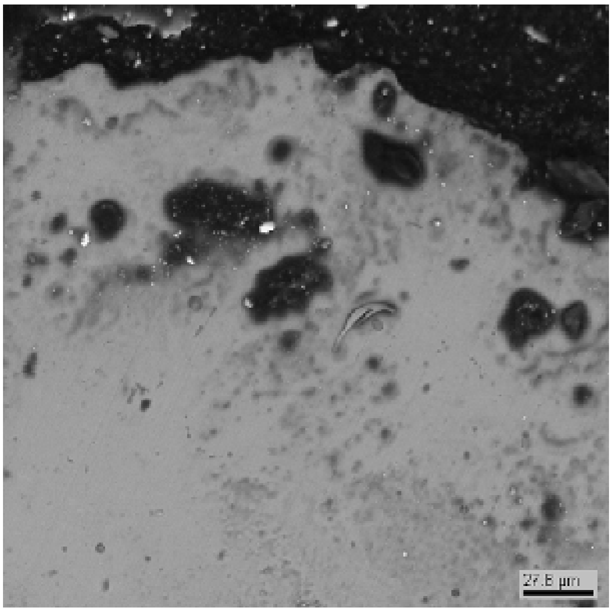

3

Fig. 1.27 – **Micrograph of region 3**

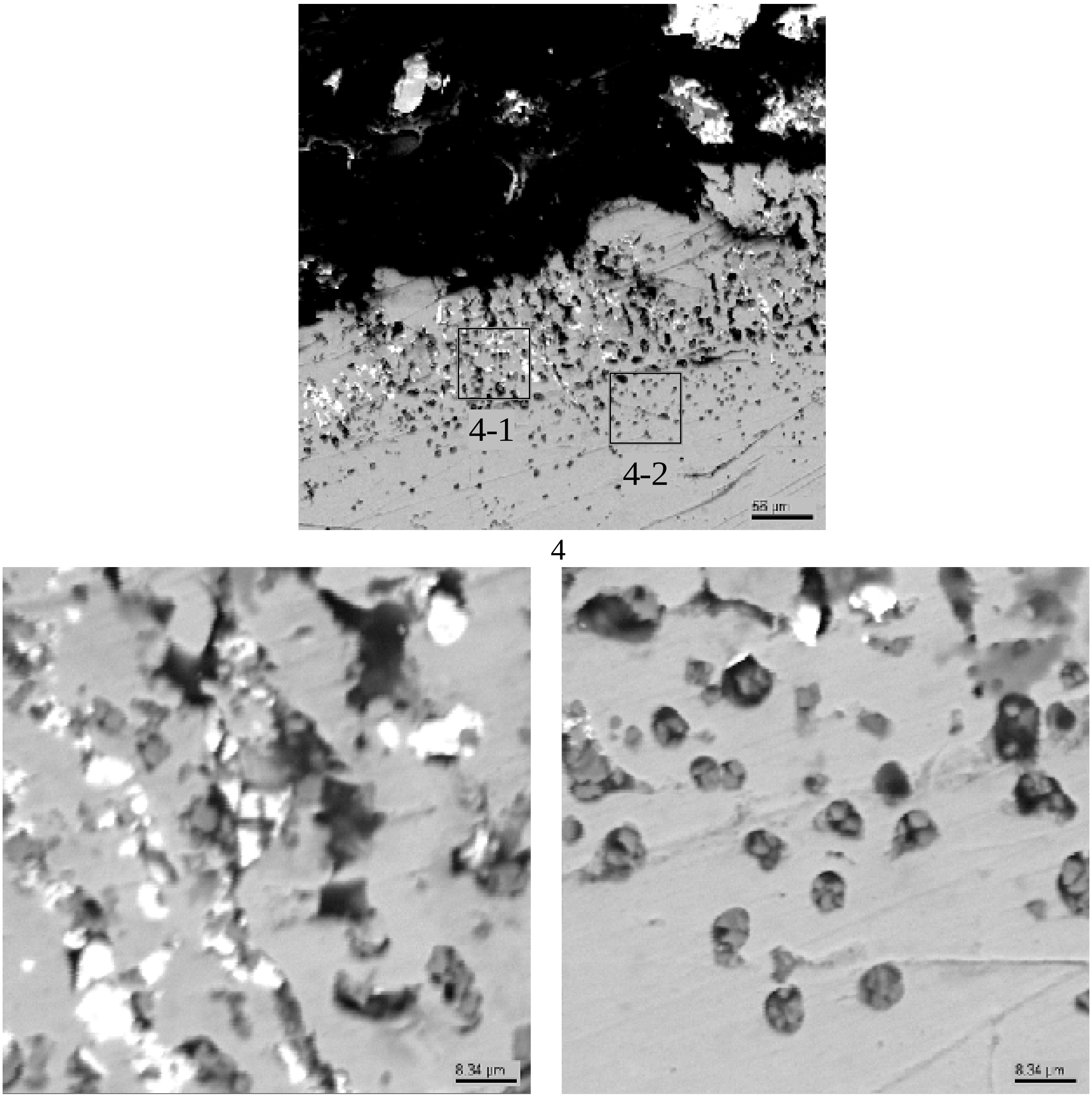

4

4-1

4-2

Fig. 1.28 – Micrographs of region 4

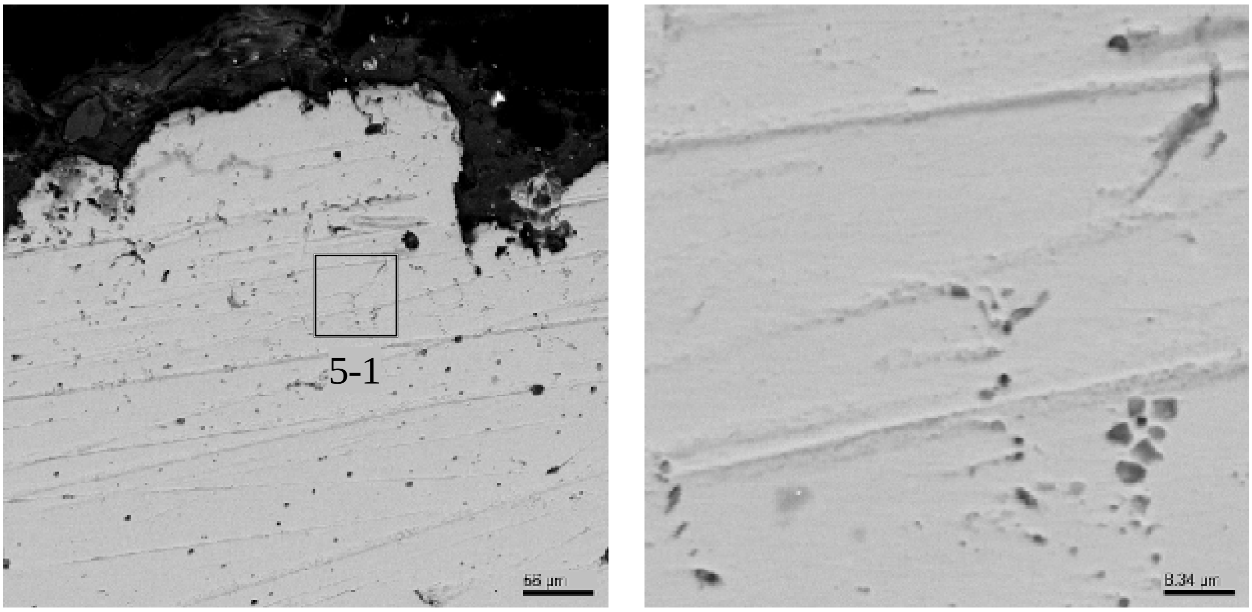

5 5-1

Fig. 1.29 – **Micrographs of region 5**

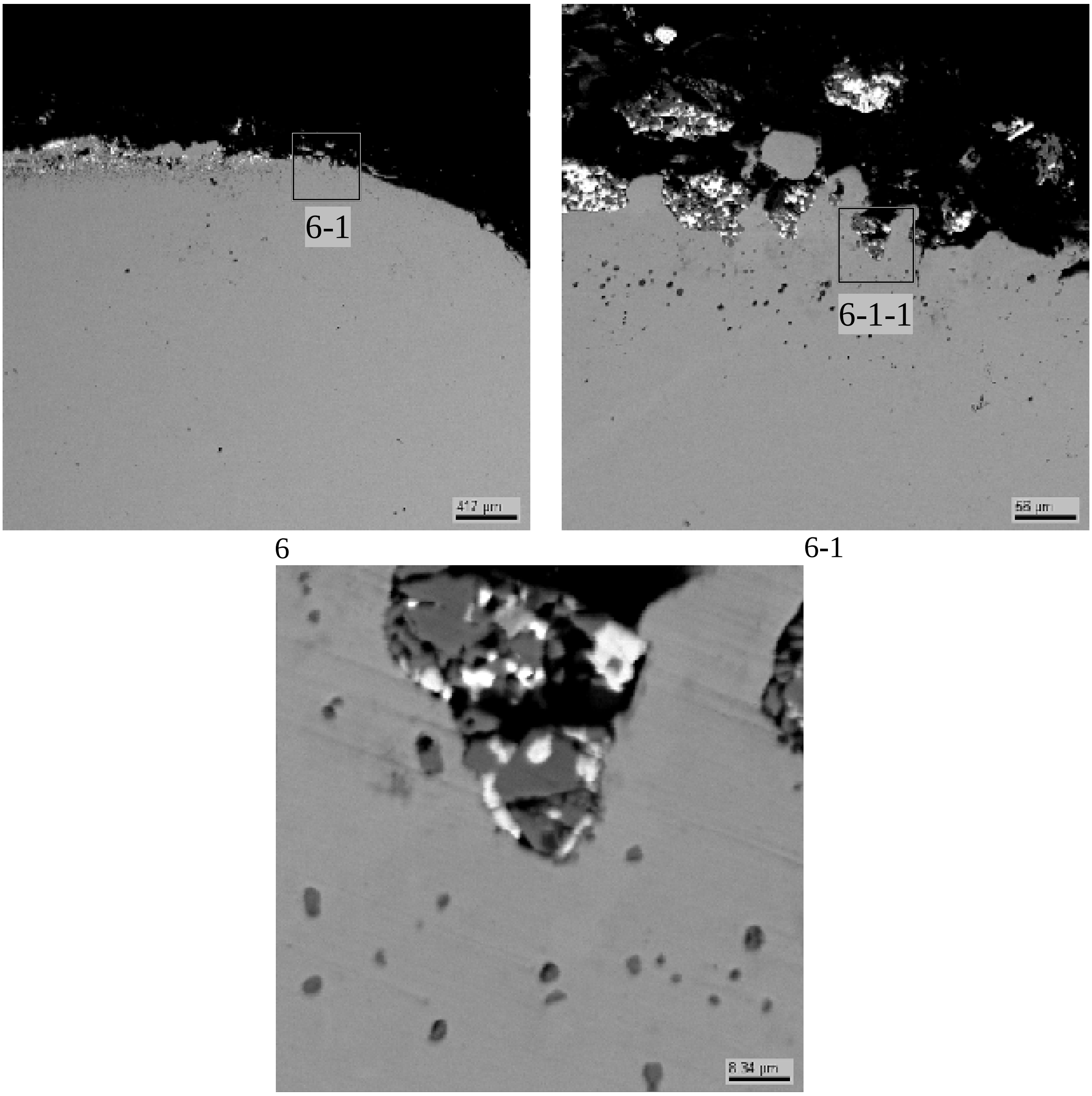

6 6-1

6-1-1

Fig. 1.30 – Micrographs of region 6

<u>The SEM/EDX of corium ingot</u>

Three templates have been prepared for the SEM/EDX: from the longitudinal section of the ingot bottom part adjacent to the steel specimen (Fig. 1.31), from the longitudinal section of the oxidic ingot upper part (Fig. 1.37), and from the longitudinal section of the crust above the corium ingot (Fig. 1.41). Bulk composition of the crystallized oxidic ingot was studied and composition of the discovered phases identified.

The analysis of all templates for the oxidic ingot bulk composition showed slight discrepancy, but in general corresponded to the U:Zr:Fe molar ratio of ~3.4:2.5:1.

Notable is a sufficiently high iron concentration in all the studied samples, including the above-melt crust, which indicates the interaction that had taken place between the steel specimen and oxidic melt.

Also, a slight increase in iron content closer to the ingot/steel boundary (Fig. 1.33, Tab. 1.17, SQ1 area), and in the above-melt crust (Fig. 1.43, Tab. 1.23, SQ1 area) may be mentioned. Uranium content is higher at the ingot lateral surface (Fig. 1.35, Tab.1.19, SQ1 area).

The unusual porosity of the ingot, not typical for all the previously investigated oxidic coria, attracts attention (e.g., see Fig. 1.32, region 1, Fig. 1.33, region 2, etc.). It caused insuperable difficulties for the mass deficiency estimation, and consequently for estimating oxygen when analyzing the ingot bulk composition by the ABT-55 instrument.

The phase microstructure of the ingot is not typical, too. The microstructure skeleton is represented by a solid solution, presumably a UO_2-ZrO_2–based one, with iron dissolved in it at the U:Zr:Fe cations molar ratio of ~5.5:3.8:1 (Fig. 1.32, field 1-1-1, Tab. 1.16, P2; Fig. 1.35, field 4-1-2, Tab. 1.19, P2; Fig. 1.43, field 2-1-1-1, Tab. 1.23, P2). Also, areas with smeared boundaries occasionally occur in bulk matrix. Presumably, the are composed of a UO_2-ZrO_2–based solid solution with iron dissolved in it at the U:Zr:Fe cation molar ratio of ~8:6.8:1 (different from that in the main phase).

Other identified phases are concentrated near pores (e.g., see Fig. 1.33, regions 2 and 2-1). It is a phase with the U:Zr:Fe cations molar ratio of ~2.5:1:1 (maybe, erroneous data, as this area has a very finely dispersed structure, Fig. 1.32, 1-1-1-1, Tab. 1.16, P1), another phase the U:Zr:Fe cations molar ratio of ~12:1.7:1 (Fig. 1.35, 4-1-2, Tab. 1.19, P1), and one more phase the U:Zr:Fe cations molar ratio of ~2.5:3.5:1 (Fig. 1.35, 4-1-2, Tab. 1.19, P3; Fig. 1.43, region 2-1-1-1, Tab. 1.23, P3).

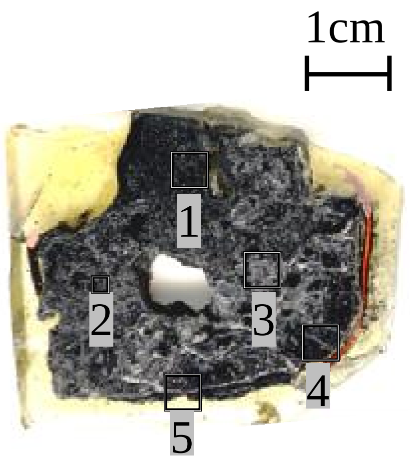

Fig. 1.31 – Template from the ingot bottom part

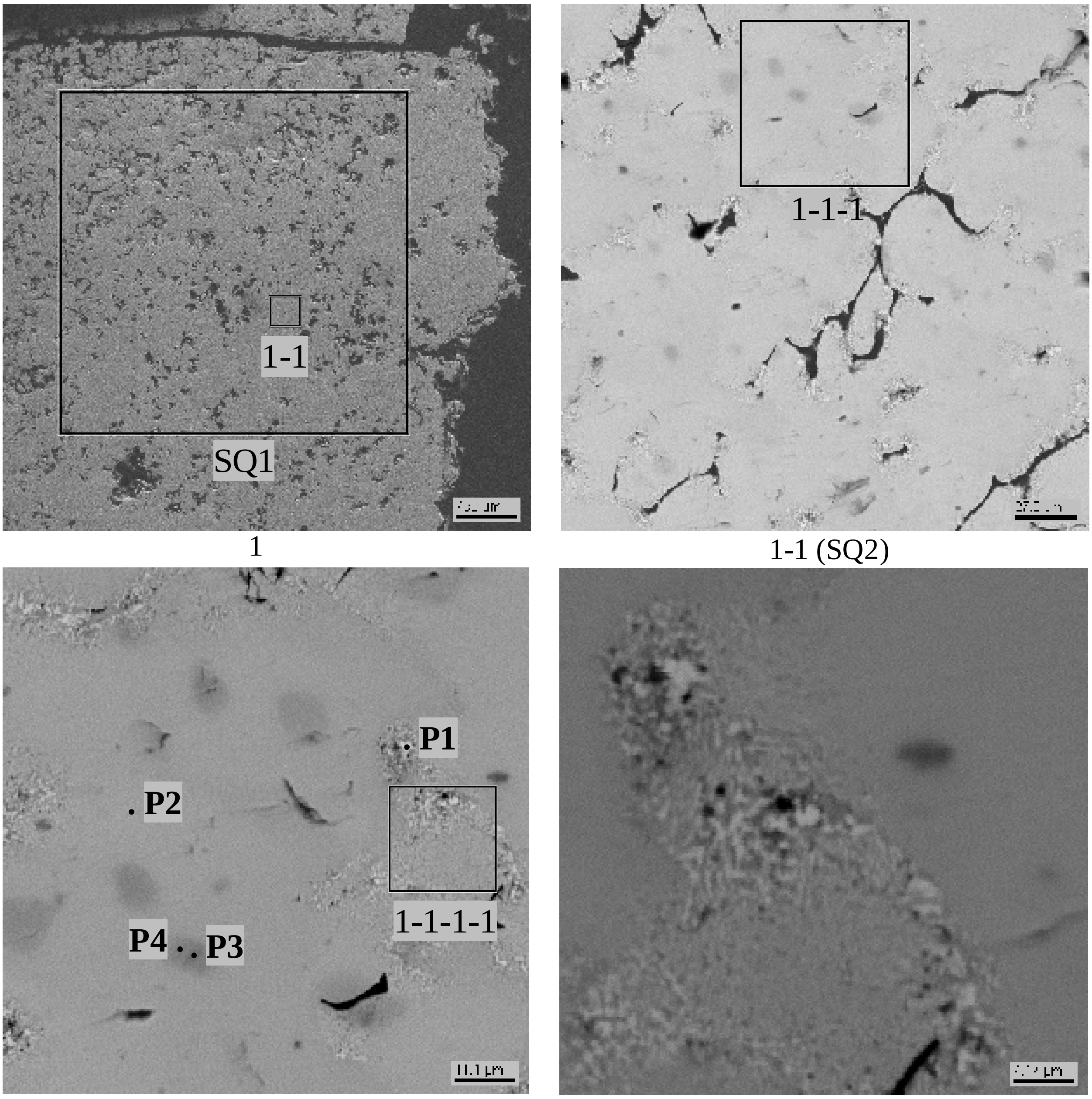

1 | 1-1 (SQ2)

1-1-1 | 1-1-1-1

Fig. 1.32 – Micrographs of region 1

Table 1.16 - Data on region 1 EDX analysis

No		**U**	**Zr**	**Fe**	**~O**
SQ1	mass %	60.59	17.08	3.89	18.43
	mol.%	15.30	11.26	4.19	69.25
	mol.% MeO_x	49.76	36.61	13.63	
SQ2	mass %	67.00	18.57	5.06	9.38
	mol.%	24.23	17.52	7.79	50.46
	mol.% MeO_x	48.90	35.36	15.73	
P1	mass %	75.99	13.20	7.06	3.76
	mol.%	38.68	17.53	15.31	28.48
	mol.% MeO_x	54.09	24.51	21.41	

P2	mass %	70.34	18.35	2.98	8.33
	mol.%	27.60	18.79	4.98	48.63
	mol.% MeO$_x$	53.73	36.58	9.70	
P3	mass %	65.55	21.26	1.91	11.28
	mol.%	22.07	18.68	2.74	56.51
	mol.% MeO$_x$	50.75	42.95	6.29	
P4	mass %	66.67	20.86	2.07	10.40
	mol.%	23.42	19.13	3.10	54.36
	mol.% MeO$_x$	51.32	41.90	6.78	

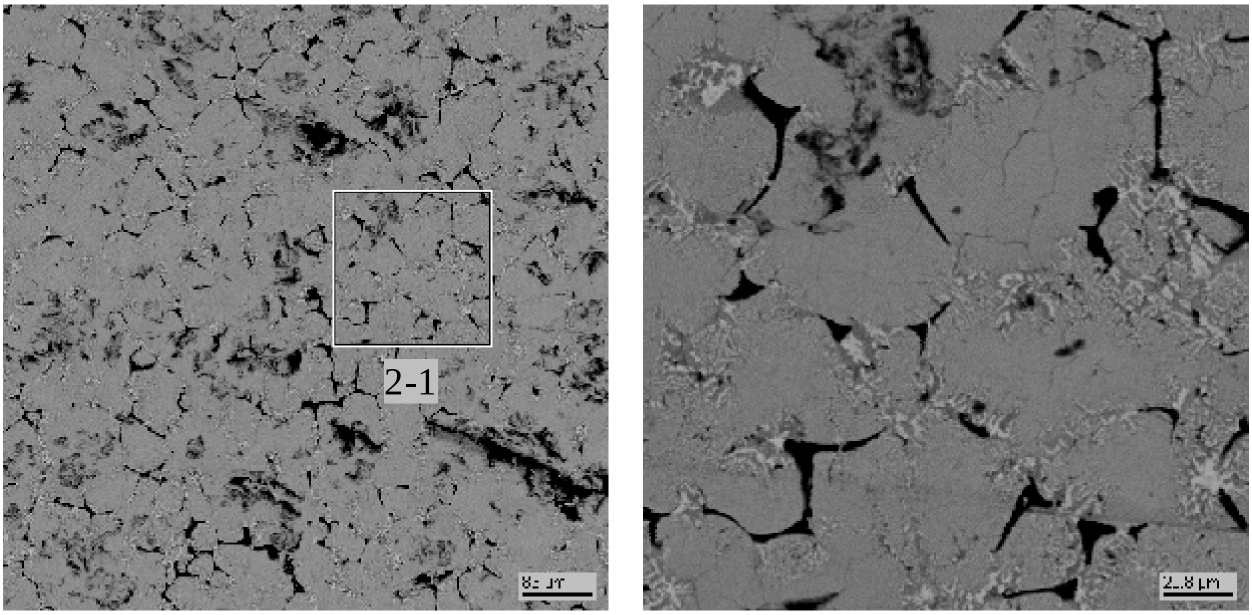

2 (SQ1) 2-1

Fig. 1.33 – Micrographs of region 2

Table 1.17 - Data on region 2 EDX analysis

No		**U**	**Zr**	**Fe**	**~O**
SQ1	mass %	66.43	18.40	5.96	9.21
	mol.%	23.99	17.34	9.18	49.49
	mol.% MeO$_x$	47.50	34.33	18.17	

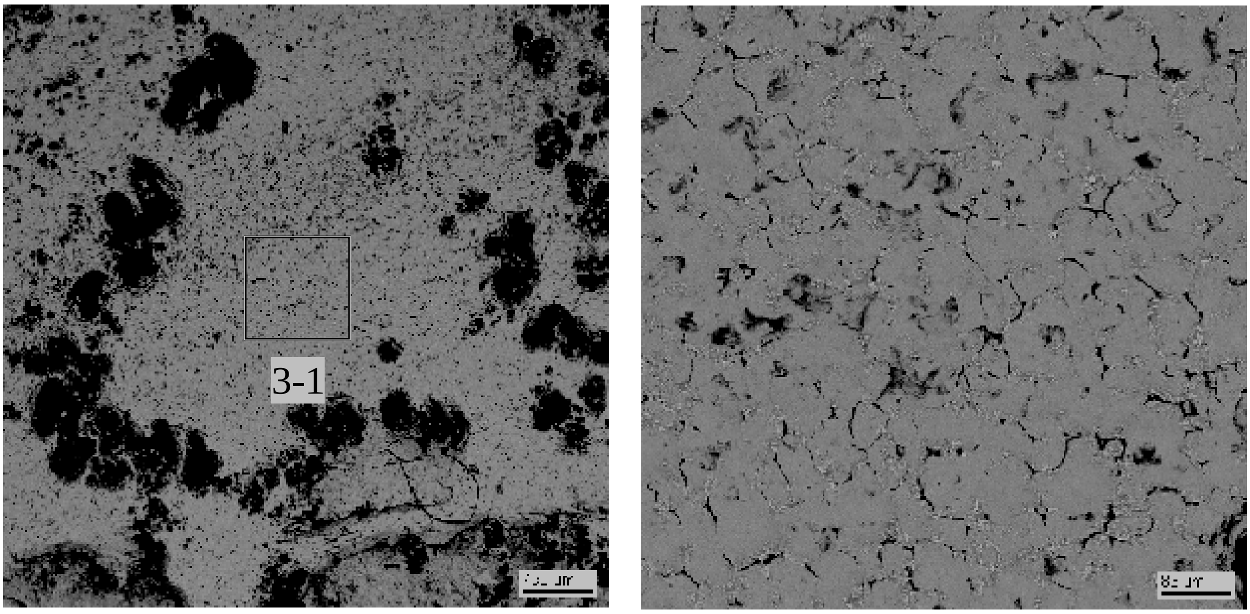

3 3-1 (SQ1)

Fig. 1.34 – Micrographs of region 3

Table 1.18 - Data on region 3 EDX analysis

No		**U**	**Zr**	**Fe**	**~O**
SQ1	mass %	68.48	18.79	4.85	7.89
	mol.%	26.80	19.19	8.08	45.94
	mol.% MeO_x	49.56	35.49	14.95	

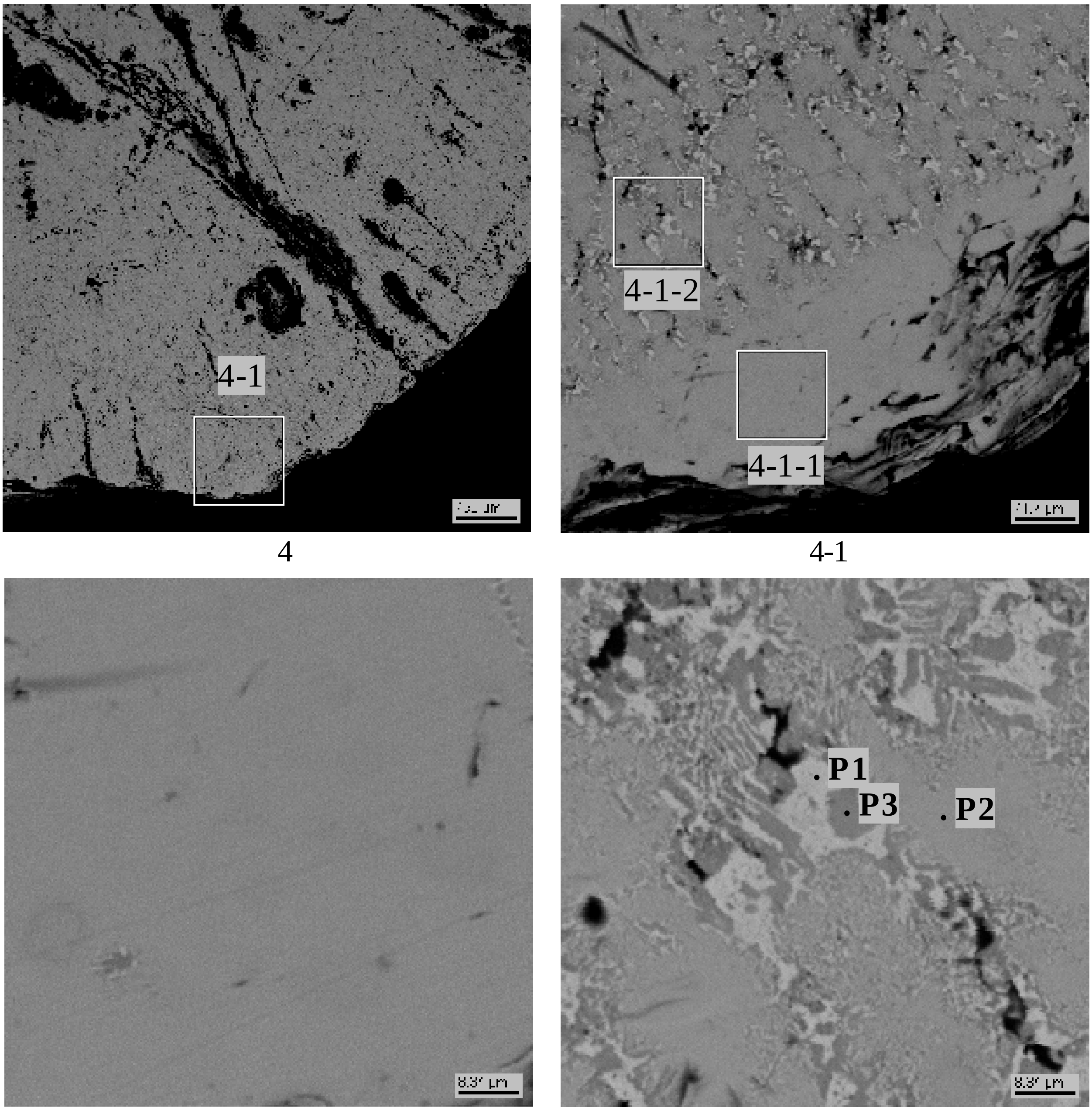

4 4-1

4-1-1 (SQ1) 4-1-2

Fig. 1.35 – Micrographs of region 4

Table 1.19 - Data on region 4 EDX analysis

No		**U**	**Zr**	**Fe**	**~O**
SQ1	mass %	67.12	17.59	1.99	13.31
	mol.%	21.01	14.36	2.65	61.98
	mol.% MeO_x	55.25	37.78	6.97	
P1	mass %	91.95	5.03	1.79	1.22
	mol.%	70.25	10.04	5.84	13.87
	mol.% MeO_x	81.57	11.65	6.78	
P2	mass %	70.80	19.45	2.65	7.09
	mol.%	29.70	21.30	4.75	44.25

	mol.% MeO_x	53.28	38.20	8.51	
P3	mass %	54.42	29.32	4.77	11.49
	mol.%	16.89	23.75	6.31	53.06
	mol.% MeO_x	35.98	50.59	13.43	

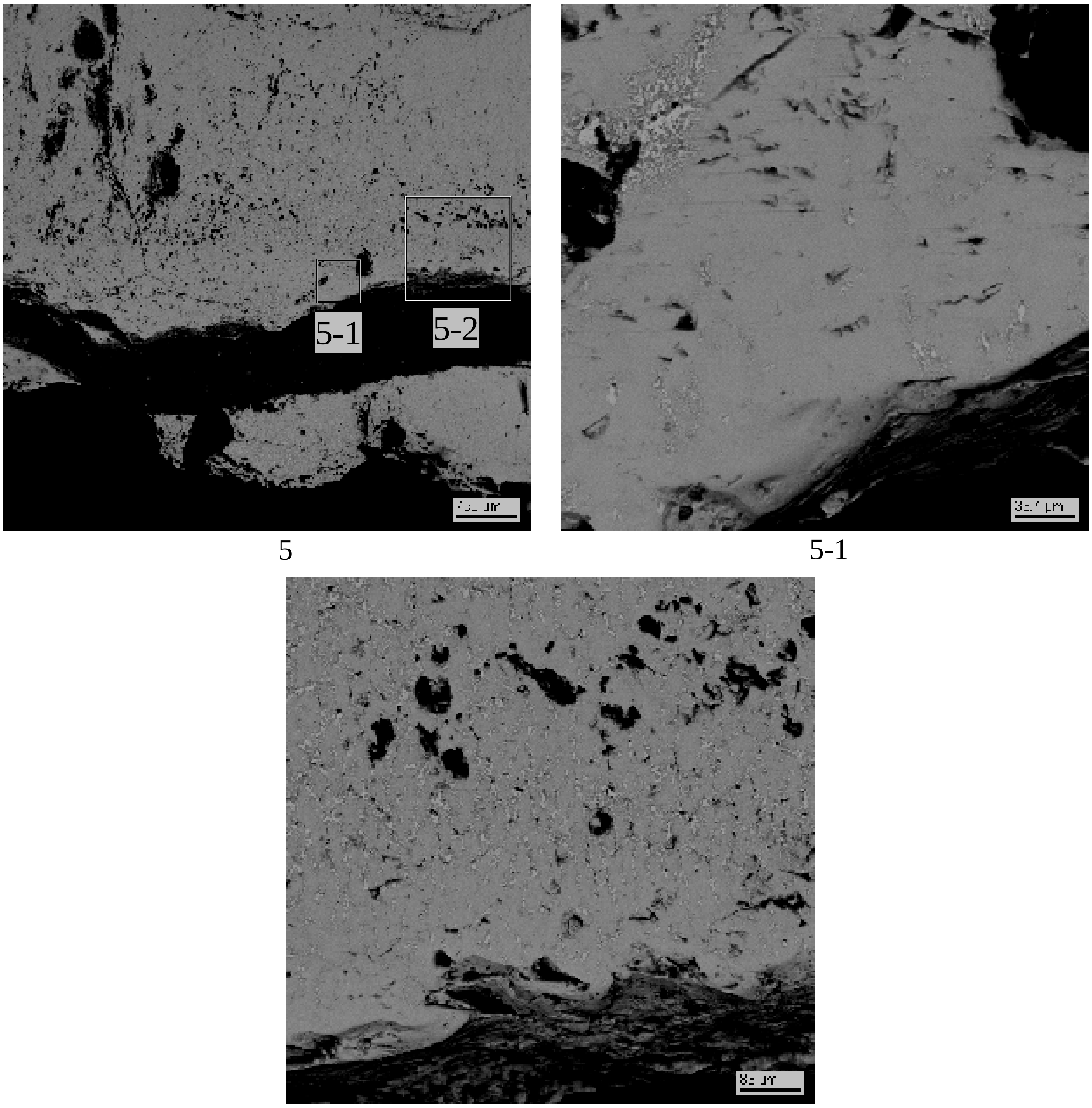

5 5-1

5-2

Fig. 1.36 – Micrographs of region 5

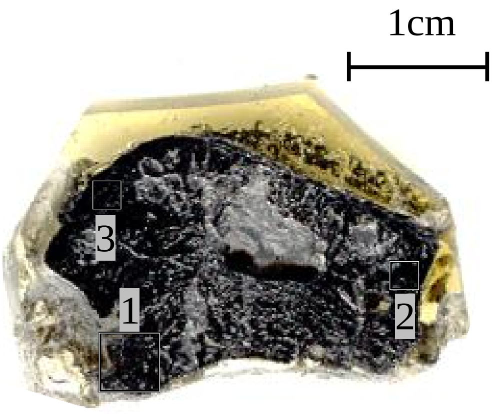

Fig.1.37 – Template from the ingot upper part

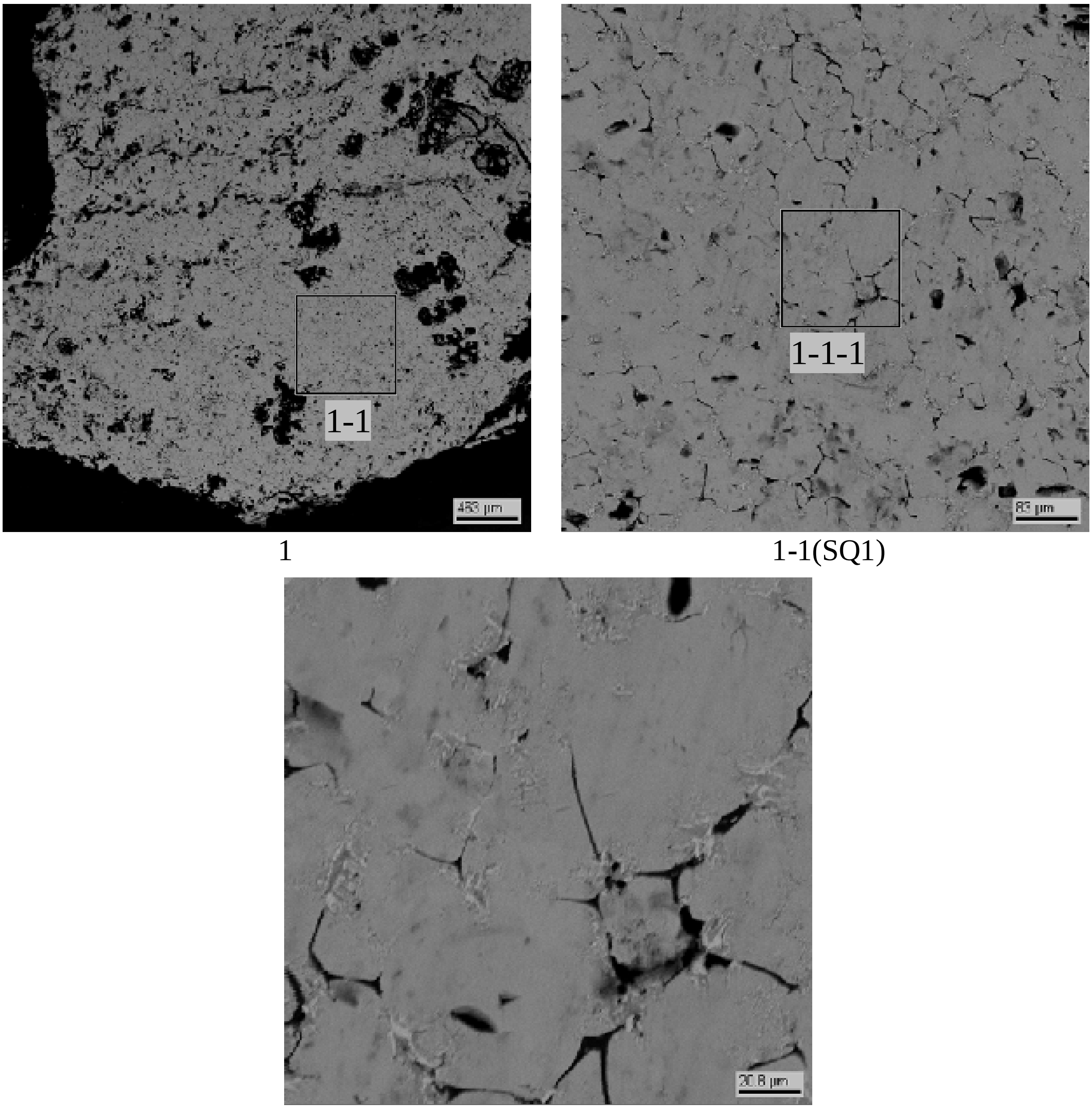

1

1-1(SQ1)

1-1-1

Fig. 1.38 – Micrographs of region 1

Table 1.20 - Data on region 1 EDX analysis

No		U	Zr	Fe	~O
SQ1	mass %	68.15	19.60	4.62	7.63
	mol.%	26.99	20.26	7.79	44.96
	mol.% MeO_x	49.04	36.81	14.15	

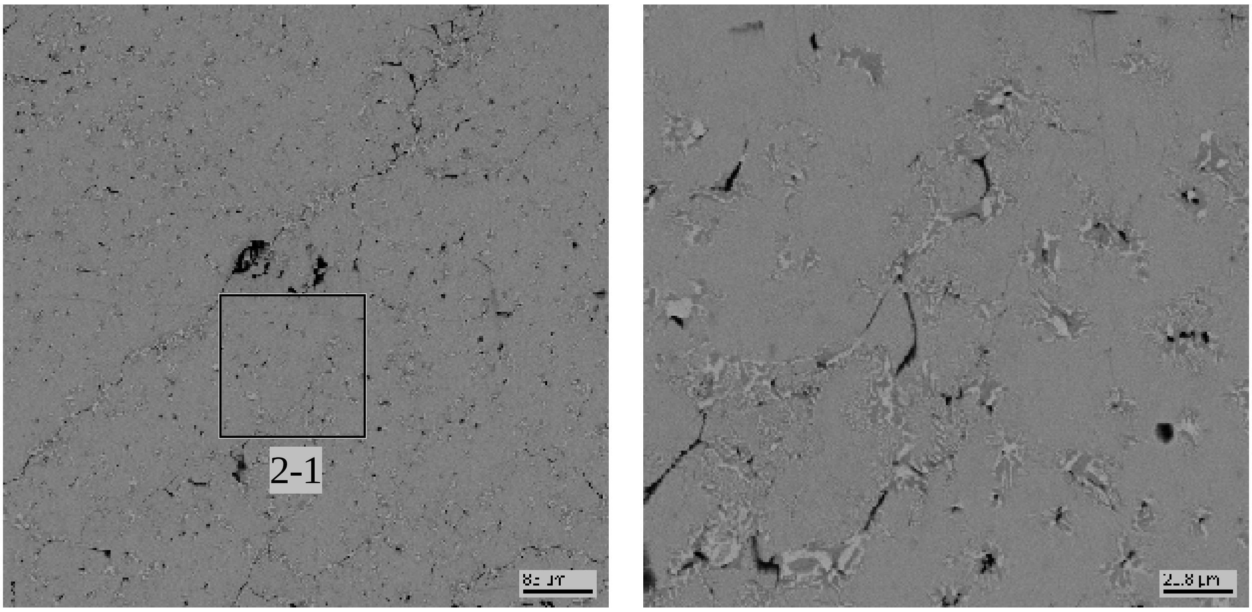

2 (SQ1) 2-1

Fig. 1.39 – Micrographs of region 2

Table 1.21 - Data on region 2 EDX analysis

No		U	Zr	Fe	~O
SQ1	mass %	70.93	19.64	3.37	6.06
	mol.%	31.29	22.60	6.34	39.77
	mol.% MeO_x	51.95	37.53	10.52	

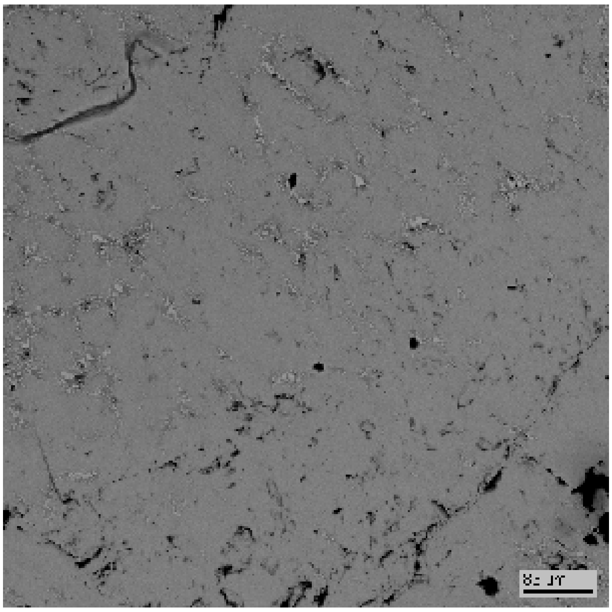

3 (SQ1)

Fig. 1.40 – Micrograph of region 3

Table 1.22 – Data on region 3 EDX analysis

No		**U**	**Zr**	**Fe**	**~O**
SQ1	mass %	67.32	20.86	3.62	8.20
	mol.%	25.97	21.00	5.96	47.07
	mol.% MeO_x	49.07	39.68	11.25	

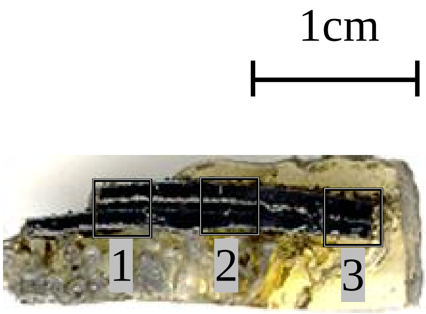

Fig. 1.41 – Template from the above-ingot crust

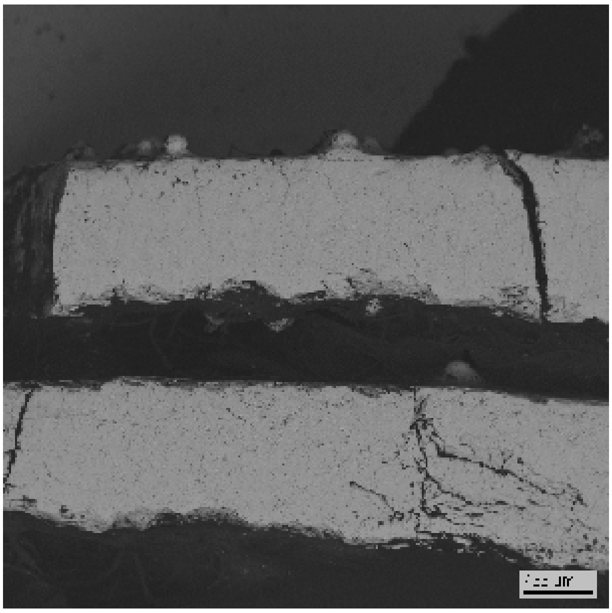

1

Fig. 1.42 – Micrograph of region 1

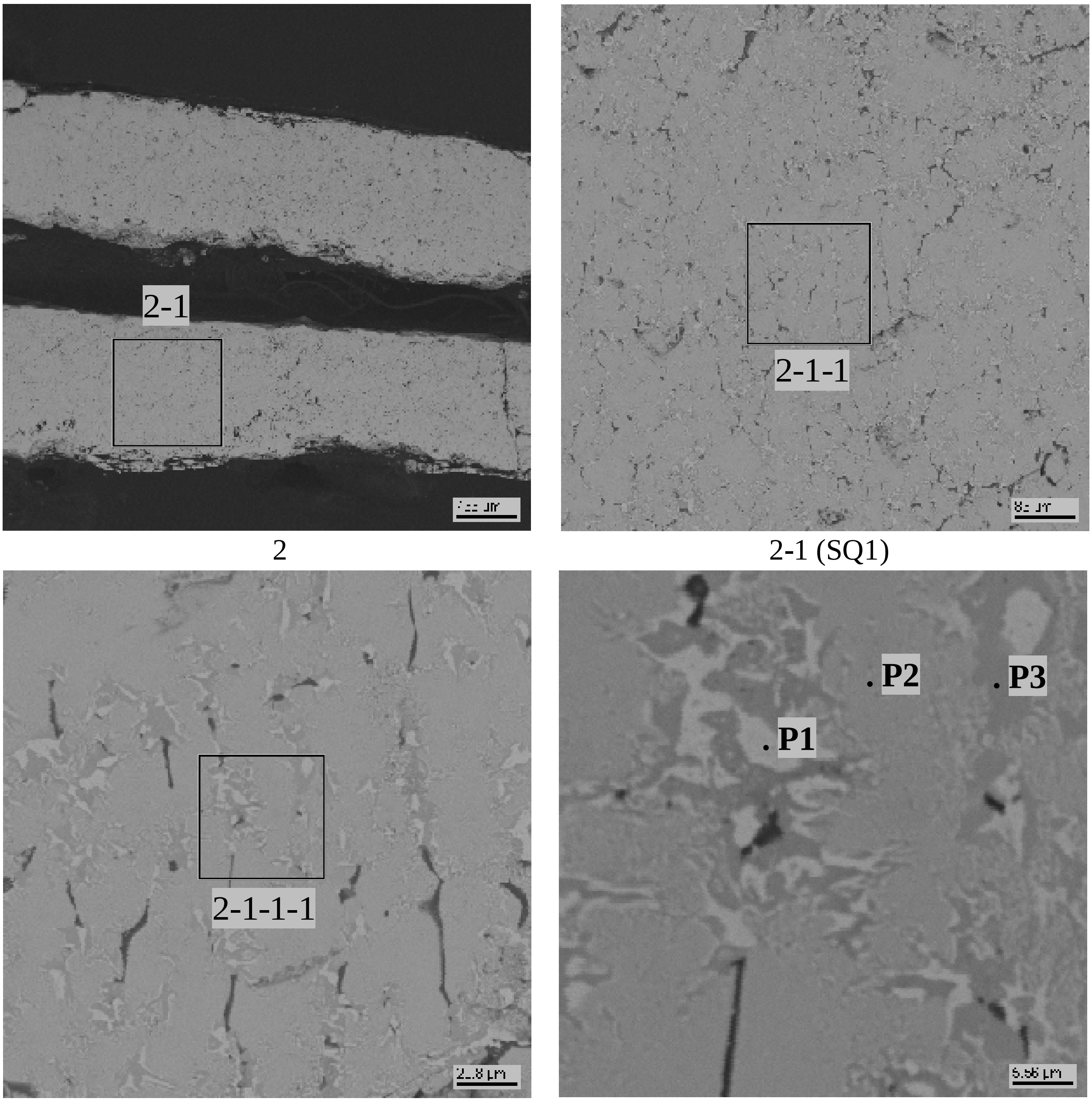

2 2-1 (SQ1)

2-1-1 2-1-1-1

Fig. 1.43 – Micrographs of region 2

Table 1.23 – Data on region 2 EDX analysis

No		**U**	**Zr**	**Fe**	**~O**
SQ1	mass %	66.68	18.71	5.80	8.81
	mol.%	24.58	17.99	9.11	48.31
	mol.% MeO$_x$	47.56	34.81	17.63	
P1	mass.%	89.86	5.87	1.89	2.38
	mol.%	60.46	10.31	5.41	23.82
	mol.% MeO$_x$	79.36	13.54	7.10	
P2	mass %	68.54	19.70	2.65	9.11
	mol.%	25.69	19.27	4.23	50.81

	mol.% MeO_x	52.23	39.17	8.60	
P3	mass %	56.69	27.88	5.33	10.10
	mol.%	18.74	24.05	7.52	49.69
	mol.% MeO_x	37.25	47.81	14.94	

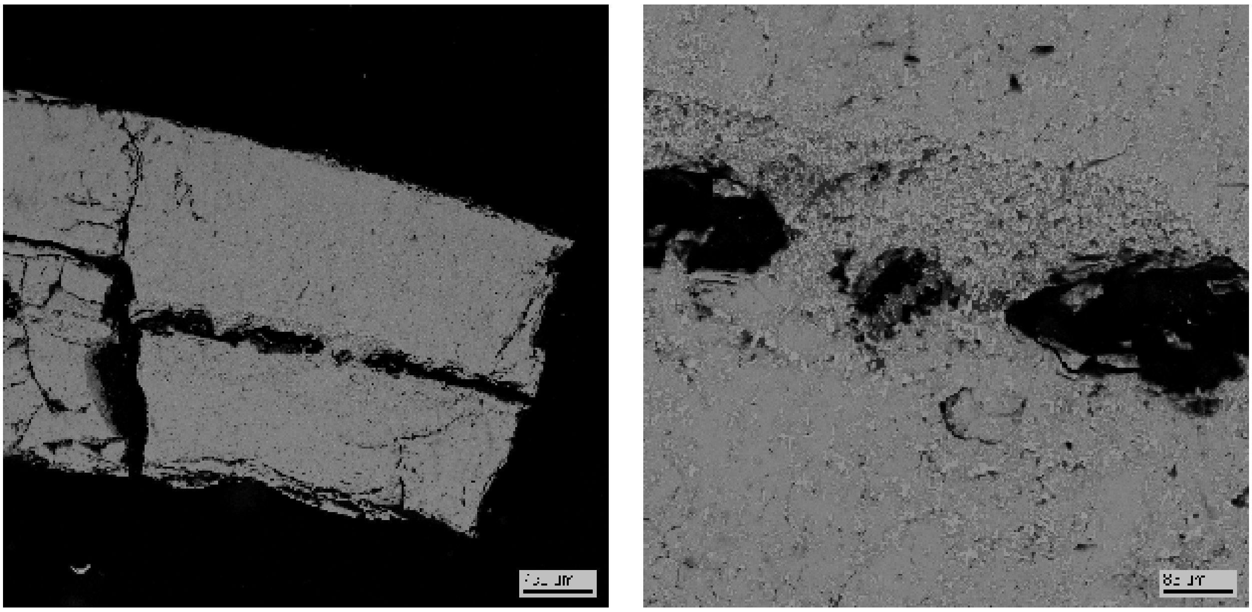

3

3-1

Fig. 1.44 – Micrographs of region 3

1.2.4.7 Specimen metallography

The performed investigations included:

- Pre-test inspection of steel;
- Initial steel specimen measurement;
- Analysis of steel structure after the interaction with molten oxidic corium.

Pre-test inspection of steel

Like for the tests MC5 – MC9, the specimen for MC10 was made from 15Kh2NMFA-A vessel steel.

Metallographic pre-test inspection of the witness specimen included analysis of its macro- and microstructure, and microhardness measuring.

Metallographic investigations and microhardness measurements were performed in the same way as in the pervious tests and showed the initial microstructure of steel to consist of the finely-dispersed pearlite, and the integral microhardness of the witness specimen (H_μ) to be 250 – 260 kgs/mm^2.

Initial steel specimen measurement

The dimensions were measured with the calipers with a scaling factor of 0.02 mm (20 μm) and the MBC-9 stereoscopic microscope with a 14 μm scaling factor and x50 magnification.

The distance A from the upper top to the first groove, distance B to the reference hole axis and diameter D of the reference hole are given in Tab. 1.24. The points of measurements are shown in Fig. 1.45.

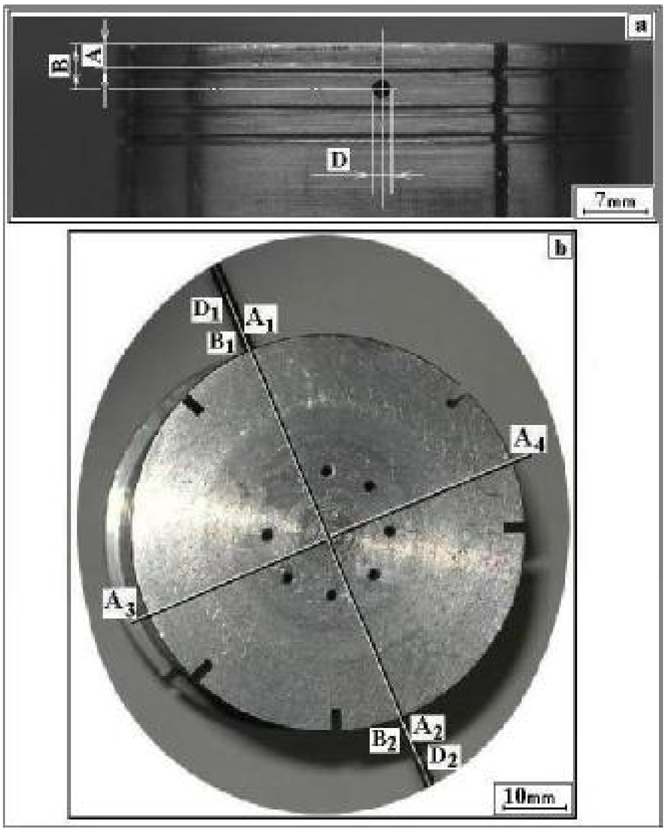

A (A_1, A_2, A_3, A_4), B (B_1, B_2), D (D_1, D_2) – points of measurements.

Fig. 1.45 – Fragments of steel specimen lateral surface (a) and upper top (b) before MC10

Table 1.24 – Steel specimen measurements (mm)

A_1	A_2	A_3	A_4	B_1	B_2	D_1	D_2
2.98	2.95	3.00	2.95	5.10	5.05	2.10	2.12

Specimen length L = 104.1 mm

These dimensions are important for the posttest determination of the initial top position and steel specimen corrosion depth.

Determination of steel ablation depth

Templates have been prepared from the oxidic corium and steel specimen after the test. The template of the steel specimen axial section was used for measuring the maximum depth of specimen corrosion, determining boundary of the interaction zone and of changes in the macro- and microstructure of steel.

Fig. 1.46 shows macrostructure of the vessel steel specimen in the longitudinal section, boundaries of the interaction zones, of the thermal influence zone, and of the regions marked for microstructure examination.

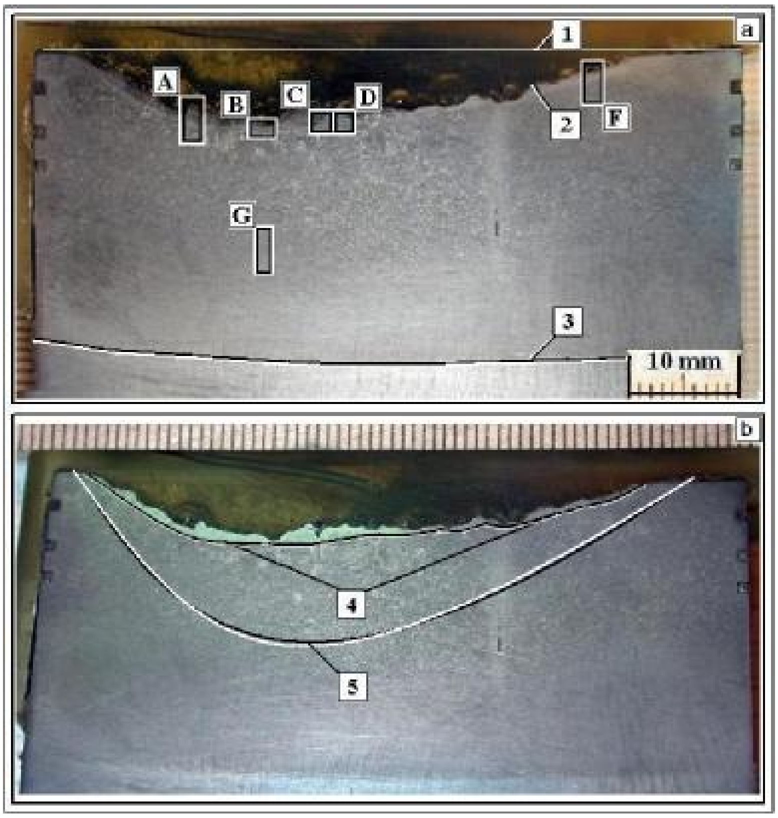

1 – reference plane of the steel specimen initial upper top;
2 – profile of specimen top after the test;
3 – zone of molten corium thermal influence on steel macrostructure;
4 – decarbonized steel zone boundary;
5 – conventional boundary of changes in steel microstructure;
A–G – microsection areas where microstructure was photographed.

Fig. 1.46 – Macrostructure of the steel specimen upper part longitudinal section

Direct measurements along the specimen longitudinal section were made using the PMT-3 microhardness tester at x180 magnification and the MBS-9 stereoscopic microscope at x50 and x100 magnifications. The scale factor of micrometer screws and object plate of microhardness tester is 0.01 mm (10 μm). The measurement error is ±10 μm; it was determined with the stage micrometer. The position of the initial top plane was determined from the groove made in the specimen lateral surface at the distance of 3.0 mm from the upper top. The images produced by processing macrosection photographs on the computer were used for plotting the steel specimen ablation diagram (line 2). Dimensions marked in the profilogram are as follows: specimen width (diameter) – along the X-line; distance from the reference plane of the initial top – along the Y-line (top-down).

According to the results of measurements, the maximum depth of steel specimen corrosion amounted to 7.15 mm. In the US sensor sighting spot it was 5.15 mm.

Fig.1.47 offers profilogram of the corium/steel specimen upper top interaction zone (line 1).

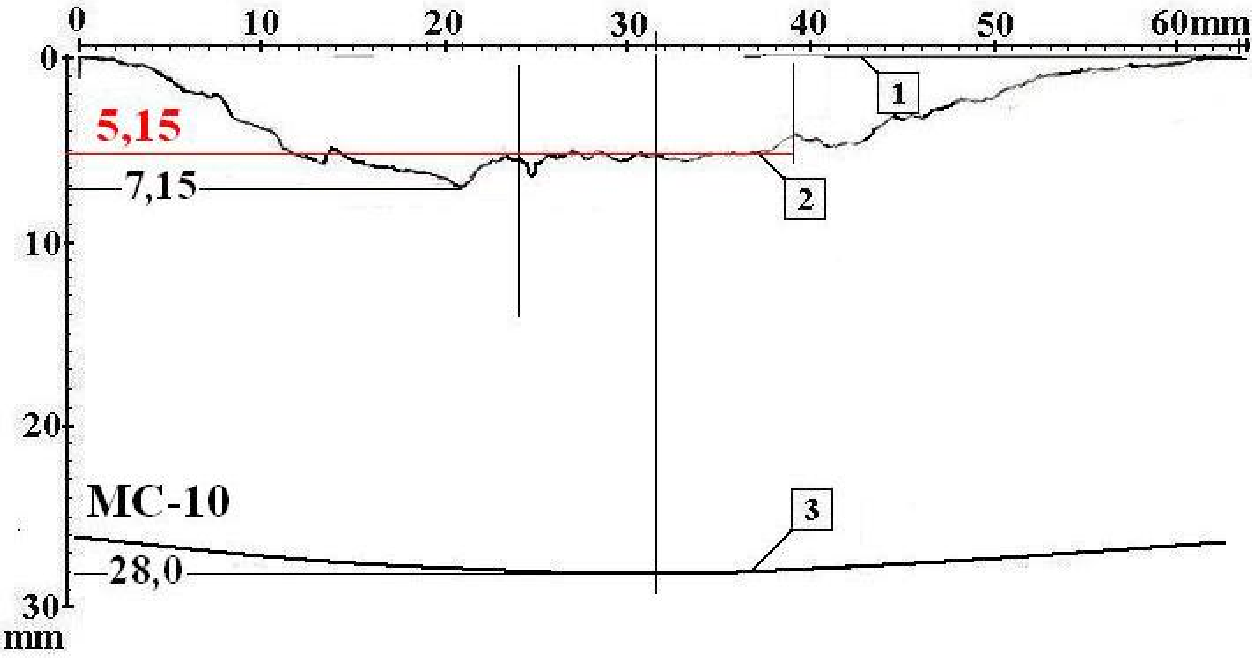

1. reference plane of the steel specimen initial top;
2. profile of specimen top after the test;
3. zone of molten corium thermal influence on steel macrostructure

Fig. 1.47 – Profiles of the interaction zone in the steel specimen axial section plane

Steel macro- and microstructure after the test

Grinding and polishing of the template was done according to the standard technique.

To reveal the microstructure, the prepared section was treated with etchants, and used metallographic microscopes for quality control. The combined use of etchants for the austenitic and pearlitic steels [17] displays both macro- and microstructure of the zone of molten corium high-temperature influence of steel and identifies microstructure of steel.

Sections' surfaces were photographed by a NIKON digital camera coupled with the METALLUX metallographic microscope at x200, x400 and x900 magnifications.

The area, within which structural transformations occurred in the specimen, spreads to a depth of 28 mm from its upper top.

Figs. 1.48 – 1.52 show steel microstructure in different zones of the specimen marked by rectangles in Fig. 1.46.

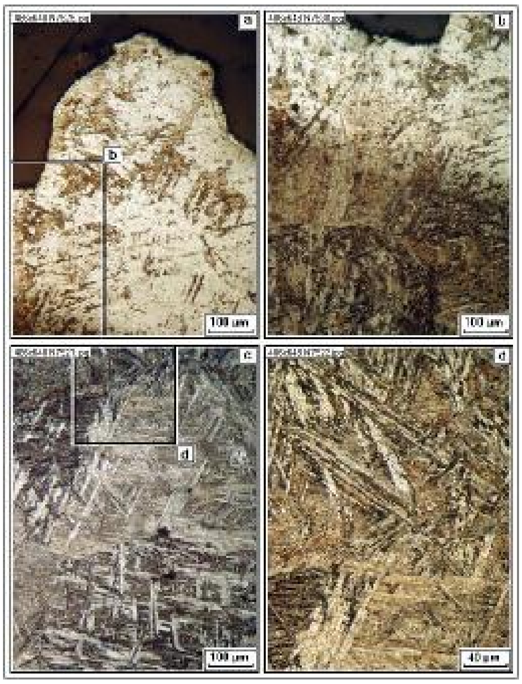

Fig. 1.48 – Steel microstructure near the top surface, area (A)

Fig. 1.49 – Steel microstructure near the top surface, area (C)

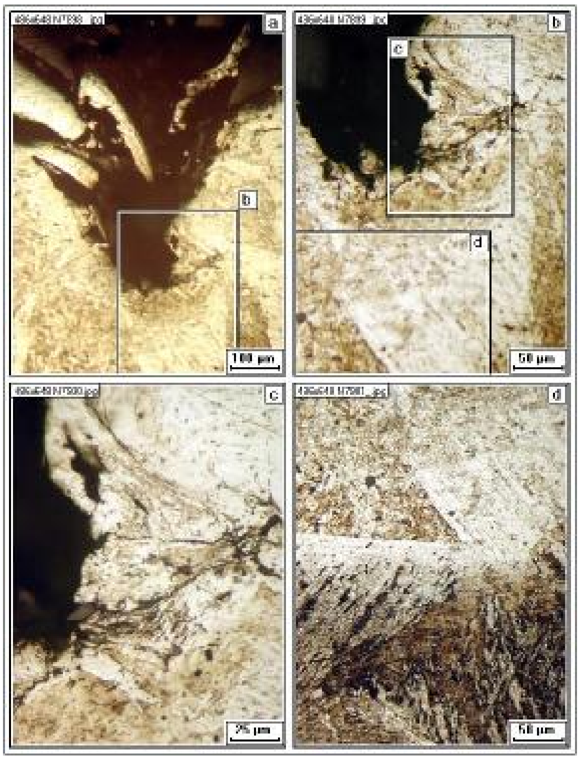

Fig. 1.50 – Steel microstructure near the top surface, area (D) with enlarged fragments (b-d)

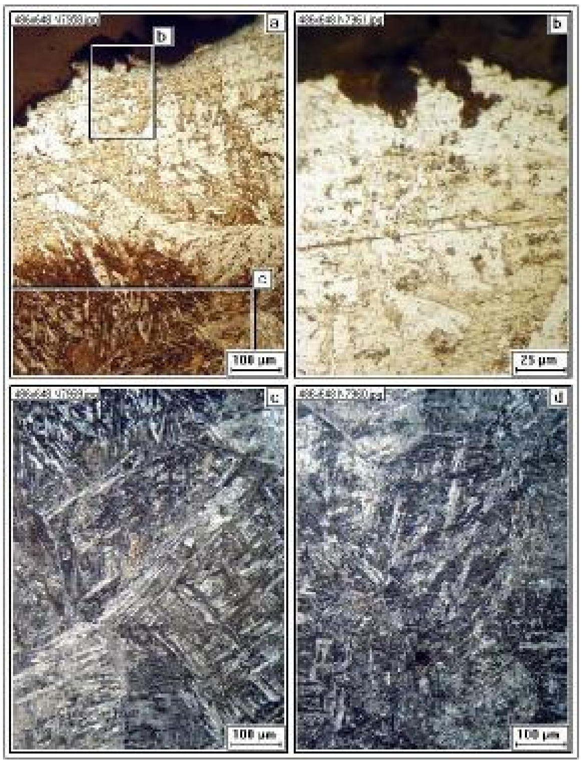

Fig. 1.51 – Steel microstructure near the top surface, area (F)

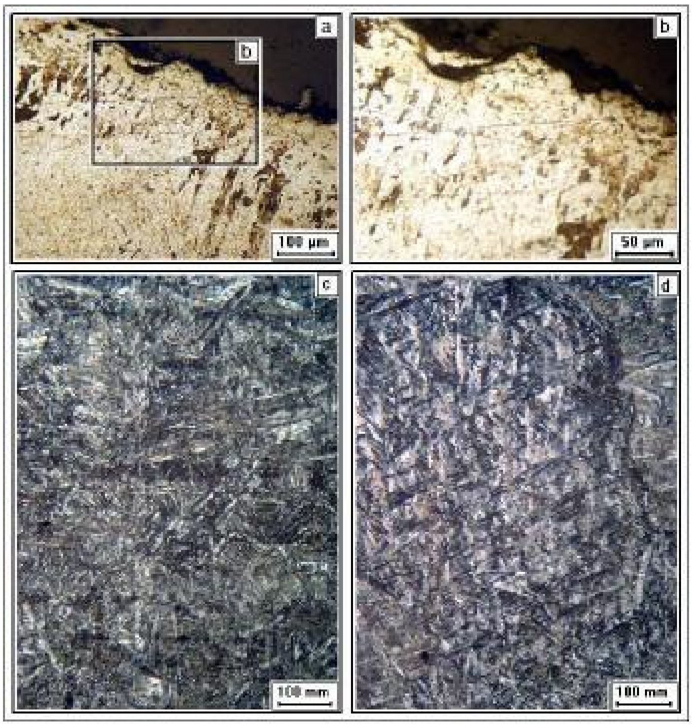

Fig. 1.52 – Steel microstructure at the top surface, with enlarged fragments: a, c – area (B); c, d – at the line 5 boundary, area (G)

A ferritic structure with the minimal carbon content has formed in the subsurface layers of the upper top which profile is shown in Fig. 1.46 b and Fig. 1.47 (line 2). This zone goes to a depth of 1-2 mm. The specimen macro- and microstructure below line 4 (Fig. 1.46 b) underwent transformations as the result of carbon and chromium repartitioning and grain size enlargement. Formation of a "new" ferrite-pearlite structure has occurred between lines 4 and 5 (1.46 b) (Fig. 1.48 c,d and Fig. 1.51 c,d). Formation of such a microstructure may occur at cooling of the steel heated above the critical point Ac_3 from the austenitic state, repartitioning of carbon, and a relatively high cooling rate. In such a case, different modifications of pearlite may be obtained, that is, sorbite, troostite or martensite, even with the given small quantity of carbon. The forming acicular pearlite may lead to an increased strength and hardness of steel and, simultaneously, a reduced impact strength and tensile strain. The area of structural transformations in the specimen goes down to a depth of 16 mm from the initial upper top. Below line 5 (Fig. 1.1.46 b) microstructural changes are insignificant. Notable is the pores formation in the subsurface layers (Figs. 1.49 & 1.50), which might have occurred at these layers melting and crystallization. Th absence of a corrosion layer in the steel specimen central part should be stressed. A possible explanation may be the melting of the specimen surface layer in the end of the test and its transport into molten corium.

To sum it up, the type of the resulting steel microstructure depends on the temperature gradient along the steel specimen height, development of diffusion and recrystallization processes during the test, and on the content of carbon in the mentioned zones.

2 TEST MC11

2.1 Test description

2.1.1 Experimental facility layout

The Pr-MC11 pretest was performed prior to the main test in order to optimize operation of the induction system, select the heating current frequencies, and produce corium with the specified composition in steam. Later this corium was crushed and used as the charge in the main test. Charge composition (mass %) : 56 UO_{2+x} – 24 ZrO_2 – 20 FeO_y. The results of the test determined selection of Rasplav-3 for MC11, i.e. of a facility with a lower inductor current frequency than that used in the tests of METCOR Phase 1. The design of furnace and steel specimen, as well as the thermometering technique, did not differ from those used in MC10.

Table 2.1 gives the locations of K-type thermocouple junctions in the specimen. Within a 10 mm radius from the specimen axis the thermocouples were embedded into channels Ø 1.5 mm, and within a 29 mm radius – into the 1.5 mm-wide carved grooves.

Table 2.1 – Thermocouple hot junction locations

Thermocouple No	α^o	r, mm (distance from the specimen axis)	h, mm (distance from the melt-facing top)
TC06	0	10	8
TC02	90	10	10
TC04	45	10	4
TC03	135	10	3
TC05	270	10	6
TC01	180	10	1
TC07	225	10	20
TC12	315	29	40
TC09	90	29	2
TC10	45	29	4
TC11	225	29	20
TC08	180	29	1
TC13	45	7.5	104.2

The system of gas and steam supply and gas-aerosol sampling is given diagrammatically in Fig. 2.1.

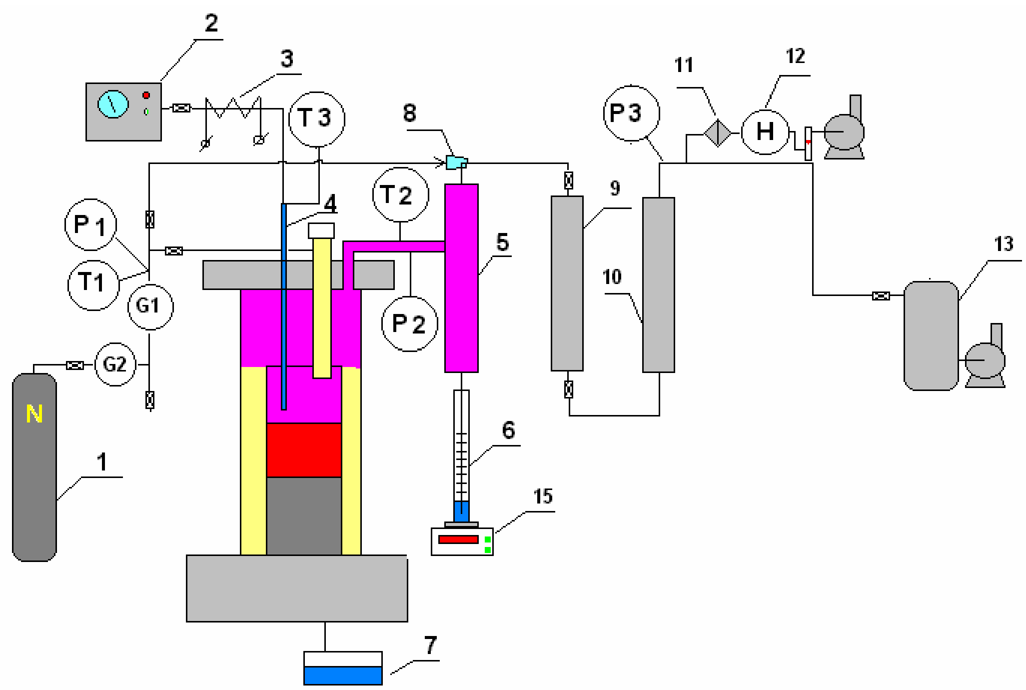

1 – nitrogen cylinder; 2 – steam generator; 3 – heated steam pipe; 4 – steam supply quartz tube; 5 – steam condenser; 6 – condensate and aerosols collector; 7 – emergency condensate collector; 8 – ejector; 9 - Petryanov Large Area Filter (LAF); 10 – silica gel column; 11 – AFA filter; 12 – hydrogen and oxygen electrochemical sensors; 13 - vacuum pump; 14 – weight strain gauge; P1, P3 – pressure gauges; T1, T2 – L-type thermocouples; G1,2 – electromechanical flowmeters.

Fig. 2.1 – The system of gas and steam supply and gas-aerosol mixture sampling

A brief description of the system operation: the start-up heating and charge melting are carried out in air. After the molten pool formation, air was cut off and steam was supplied into the furnace via steam supply tube (4) from steam generator (2). To avoid steam condensation, the steam pipe (3) was heated up to 120-150°C. From the furnace, the steam-gas mixture proceeded to steam condenser (5). The condensate flowed down into reservoir (6). Strain gauge (15) was used for the online measurement of the condensate weight. The condensable were taken from the condenser by ejector (8) and nitrogen (1) was used as the carrier gas. Then the gas arrived at filter (9) and passed silica gel dehumidifier (10). The composition of gas, in particular, hydrogen and oxygen concentration in it, was controlled by electrochemical sensors (12) after the additional purification at filter (11).

2.1.2 Materials

A special procedure was followed to load the crucible with the specified mixture (mass %) of 56.1$UO_{2.24}$-23.9ZrO_2-20FeO. A 150.3 g batch of corium composed of 57.54% UO_{2+x}; 24.69% ZrO_2; 17.77% FeO_y) (mass % here and further in text) with particles dispersivity below 50 µm was placed on the steel specimen top. The corium composed of 57.54% UO_{2+x}; 24.69% ZrO_2; 17.77% FeO_y has been fused in steam before, in a special Pr-MC11 test. Then the charge composed of powdered U_3O and ZrO_2 and corium (57.54% UO_{2+x}; 24.69% ZrO_2; 17.77% FeO_y) was added, and metallic Zr (10 g) was used as the start-up material.

The composition and masses of substances loaded into the crucible before melting are given in Tab. 2.2.

Table 2.2 – Charge components composition and mass

Purpose	Component	Fraction, mm	Mass, g	mass %
Crust imitator	Corium (57.54% U_{2+x}; 24.69% ZrO_2; 17.77% FeO_y)	< 50	150.3	10.4
Main charge	Corium (57.54% UO_{2+x}; 24.69% ZrO_2; 17.77% FeO_y)	< 500	1106.9	76.8
	Urania (U_3O_8)	< 500	133.1	9.2
	Zirconia, ZrO_2	< 50	41.8	2.9
	Metallic zirconium, Zr	plate	10.0	0.7
Total			**1442.1**	**100.0**

The required fraction of corium (57.54% UO_{2+x}; 24.69% ZrO_2; 17.77% FeO_y) was obtained through crushing the corium ingot fused beforehand in the Pr-MC11 test.

2.1.3 Experimental procedure

The start-up heating and molten pool formation in air were done at Z_c=20 mm, Ze=10 mm, where Z_e, Z_c are the distances from the inductor lower coil to the electromagnetic screen and to the welded sections upper edge, respectively. At 520 s the molten pool surface temperature was about 2050°C, and from 630 through 790 s a considerable growth of temperature at the specimen top was indicated by thermocouples (Fig. 2.2). To limit the specimen surface temperature, the crucible was shifted 5 mm down (Z_c=25 mm, Ze=15 mm) at 830 s of the 1st oxidation regime, and during the period from 870 to 1180 s power to the melt was decreased (Fig. 2.3). This brought the molten pool surface temperature down to 1950°C. At 1248 s the molten pool depth and bottom crust thickness were measured and found to be 60 and 2 mm, respectively. Then the crucible was again shifted 2 mm down (Z_c=27 mm, Ze=17 mm).

At 1748 s steam was supplied into the furnace. The temperature at the specimen top was found to be about 900°C and, in accordance with the test plan, from that moment of the stabilized temperature regime #1 the vessel steel ablation kinetics at the interaction with corium through the crust was studied in steam. After the supply of steam, a water layer formed on the pool surface due to condensation of a pert of steam on the water-cooled surfaces of the furnace. To avoid the complete flooding of the surface with water, steam was temporarily cut off, and the rate of its supply into the furnace reduced at 2487 and 2676 s. To intensify water evaporation from the melt surface, the screen was shifted upwards 3 mm at 2777 s and 2 mm at 2812 s (Z_c=27 mm, Ze=12 mm), thus reducing the specimen surface temperature, and then increased power in the melt to simultaneously raise the melt temperature and the specimen surface temperature. The molten pool surface was periodically observed when the pyrometer shaft was temporarily blasted with air. The insignificant amounts of oxygen were then getting into the furnace and it was recorded by the oxygen sensor (Fig. 2.6).

The US measurements indicated either absence, or a very low rate of vessel steel corrosion during regime #1 (later the US measurements for this regime were found to be unreliable), and therefore a transition to the temperature regime #2 was made. Again, the screen was shifted 2 mm down at 3771, 3820 and 3995 s (Z_c=27 mm, Ze=18 mm). By regulating the inductor voltage, the temperature at the specimen top was maintained at about 1050°C and from 4000 through 11500 s measured the vessel steel corrosion kinetics by the US technique. When stabilizing temperature, periodical bursts of pressure (rarefaction) in the steam-gas line from the furnace took place, presumably due to periodical burning of the hydrogen mixture (deflagration) (Fig. 2.5). Also, cracking sounds were heard from the furnace occasionally. Presumably, hydrogen was accumulating in the shaft and detonation (rapid burning) of the mixture occurred. Hydrogen accumulation was stopped by blasting the shaft with nitrogen periodically. This also facilitated observations of the molten pool surface. Thanks to raising the melt surface temperature, the unwanted condensate accumulation at the pool surface stopped. At 5000 s water entered the condensate drip pan (7, Fig. 2.1), though the condensate weight growth slowed down according to the weight gauge (Fig. 2.7). It happened due to the seal failure of the inner quartz tube (separating the crucible above-melt space from the rest of the induction furnace volume) and steam partial condensation in the crucible manifold assembly. At 5000 and 5700 s the carrier gas flowrate was stepped up from 160 to 210 and 300 l/h (Fig. 2.1.7), respectively, in order to decrease hydrogen concentration in the carrier gas.

At 11500 s transition to temperature regime #3 was made and at 11575 s the crucible was shifted 4 mm upwards (Z_c=23 mm, Ze=14 mm), and the screen was shifted 2 mm down twice, at 11648 and 11854 s (Z_c=23 mm, Ze=18 mm). The temperature at the specimen top was approximately 1150°C and from 12000 through 13800 s, the studies of vessel steel corrosion kinetics were continued during the stabilized temperature regime #3 according to the test plan. During this temperature regime, the instability of the specimen temperature condition noted during regime #2 has worsened, and the specimen temperature stabilization required considerable manipulation of the inductor voltage.

At 13900 power in the melt was stepped up and transition to the temperature regime #4 made. The temperature at the specimen top was approximately 1220°C. The specimen temperature condition was also instable during this regime. By 14930 s the US sensor showed corrosion depth to be about 4 mm, i.e. indicated the corrosion front advance to the acoustic defect within the specimen body (Fig. 2.8).

At 14937 s heating was disconnected and the ingot with specimen were cooled in steam. During cooling, the ingot contacted with steam and water that condensed on the water-cooled components of the furnace.

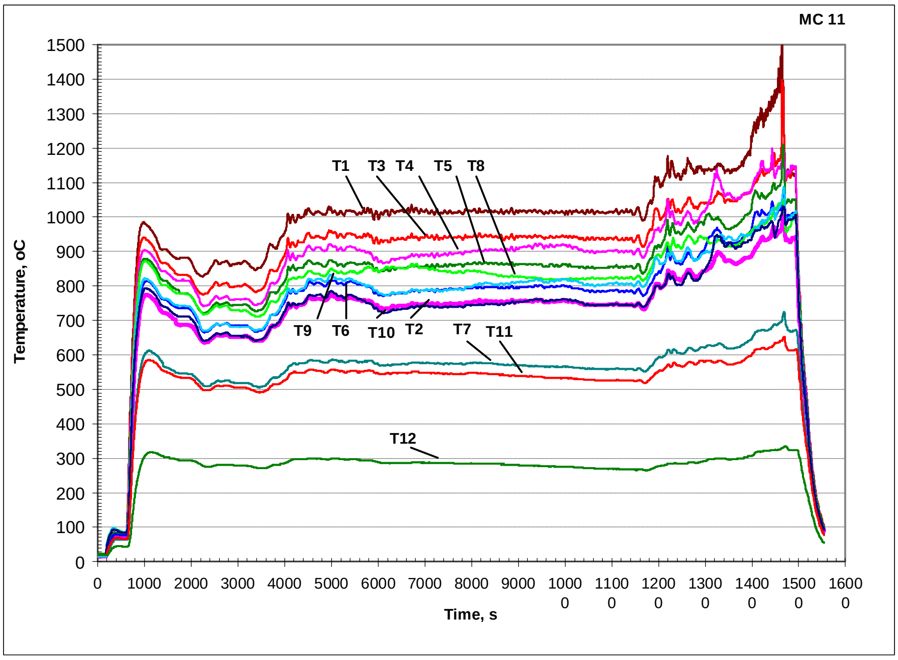

Fig 2.2 – Thermocouple readings in MC11

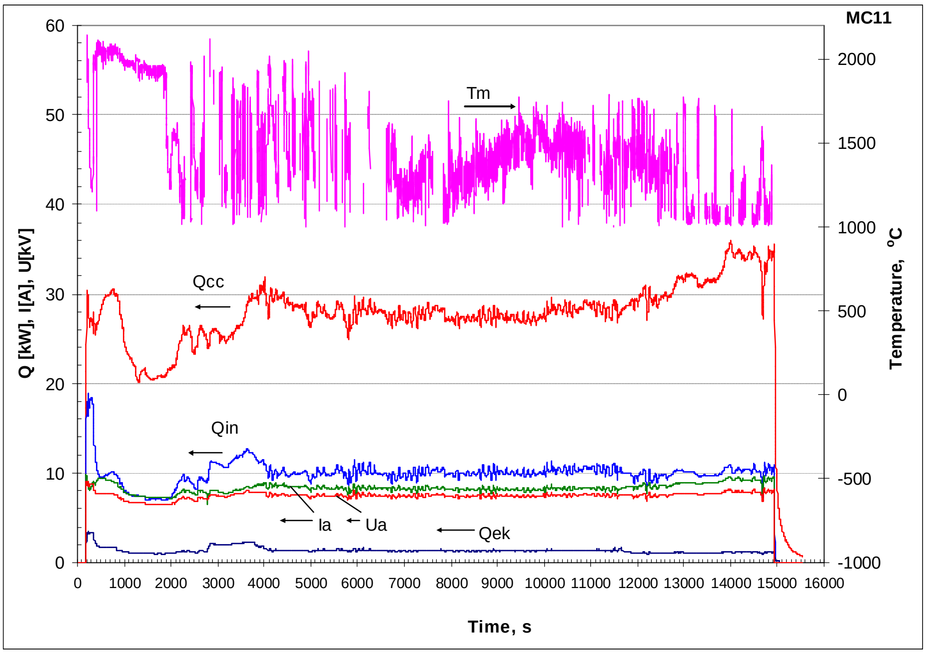

Fig. 2.3 – History of heat and electromagnetic fluxes, anode current and voltage, and pyrometer readings

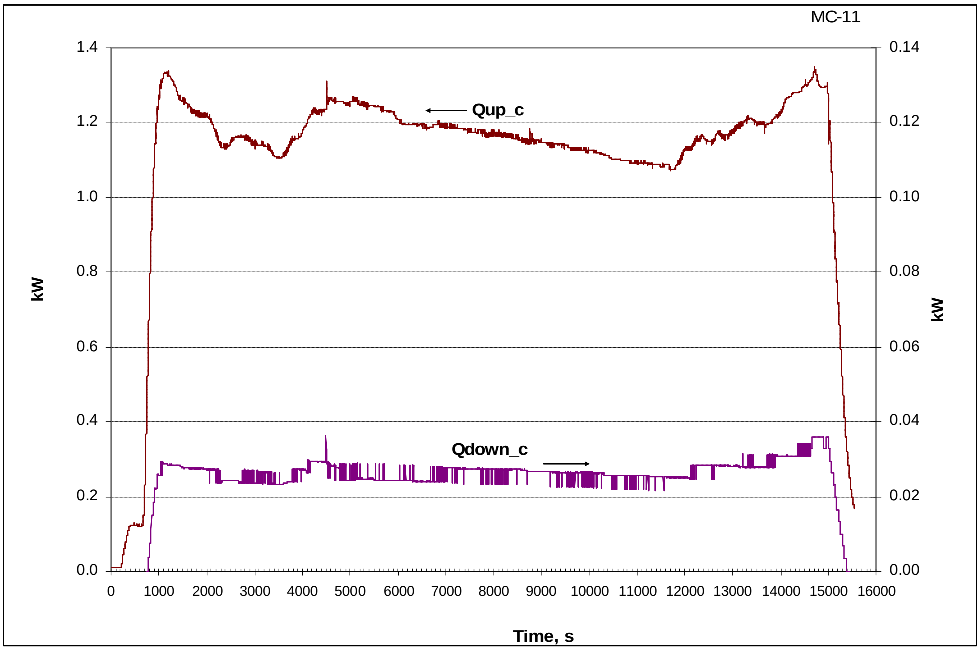

Fig. 2.4 – History of heat fluxes to the top (Q_{up}_c) and bottom (Q_{down}_c) calorimeters

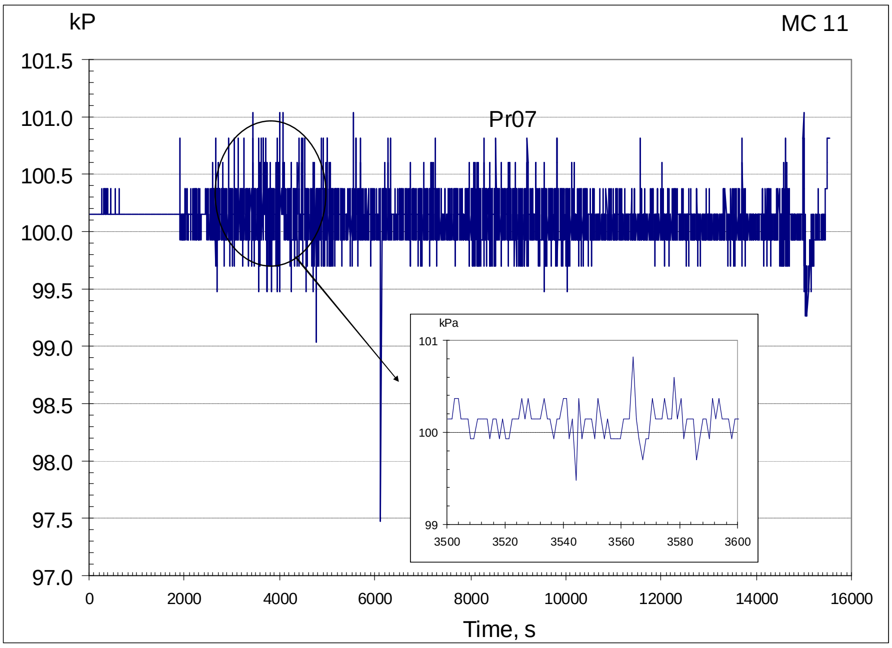

Fig. 2.5 – Absolute pressure gauge readings in the gas-steam line at the outlet from the furnace

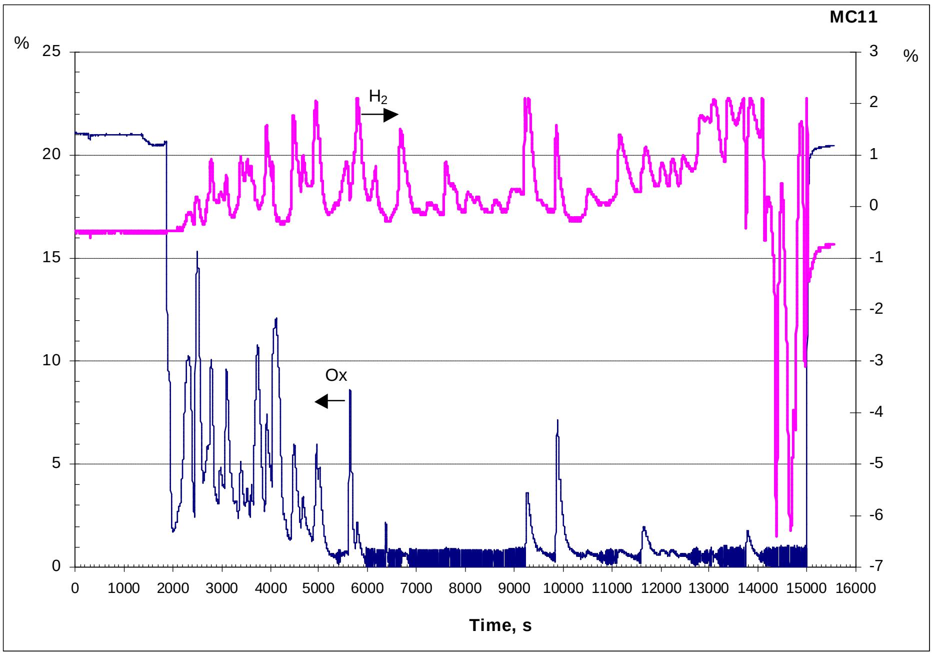

Fig. 2.6 – Readings of the oxygen and hydrogen electrochemical sensors

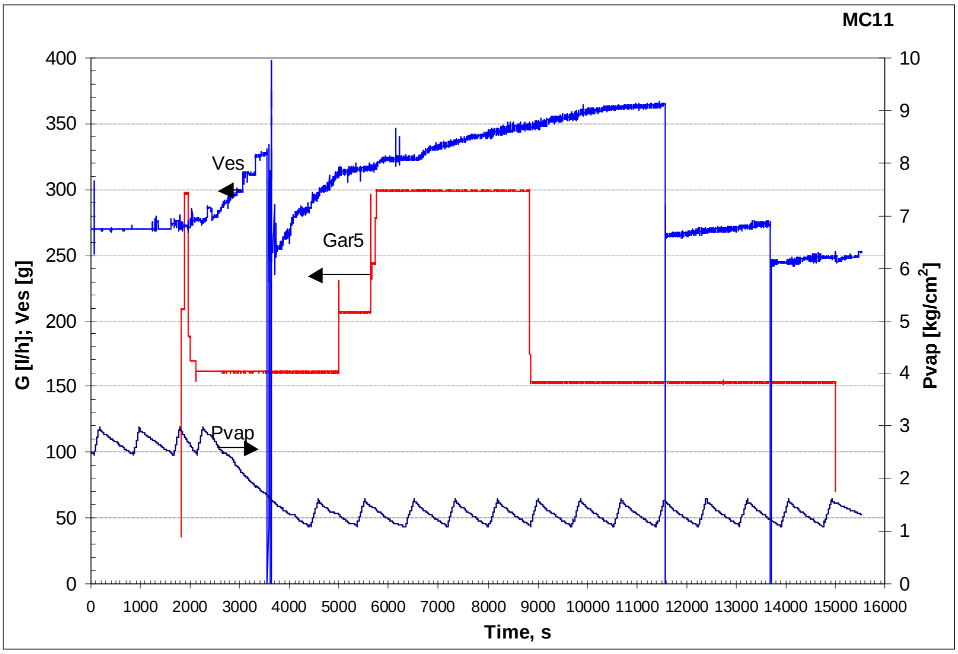

Fig. 2.7 – Readings of the steam generator pressure gauge (Pvap), carrier gas flowrate (Gar5) and weight strain gauge (Ves)

2.1.4 Ultrasonic measurements of the specimen corrosion

The technique of measuring the specimen corrosion depth in MC11 did not differ from the one used in MC10.

The corrosion depth history is shown in Fig. 2.8. Due to malfunction of the ultrasonic signals registration, the data obtained before the beginning of regime #2 were lost. Therefore, the average rate of corrosion during the time interval from ~700 till 4000 s (beginning of regime #2) was determined from the depth of corrosion reached by the beginning of regime #2, correlated with the said time interval. For other three regimes, corrosion rate was determined in the same way as in MC10. It should be noted that during regime #4 an abrupt spontaneous specimen temperature growth (see Fig. 2.2) was noted starting from 14600 s, so for determining the rate of corrosion, duration of this regime was limited by the said time.

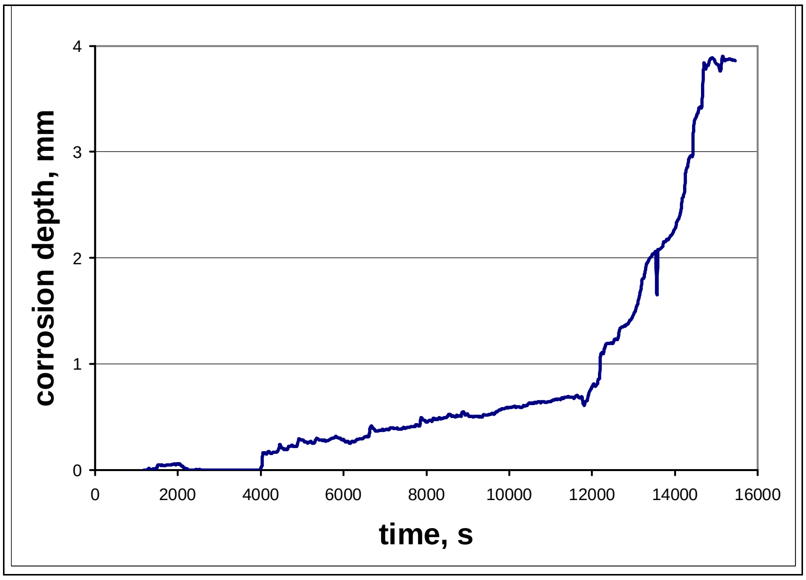

Fig. 2.8 – Specimen corrosion kinetics

Finally, the values of corrosion rate obtained for each of 4 regimes, are as follows:

Regime #1, from 700 through 4000 s – 0.17 mm/h.

Regime #2, from 4000 through 11500 s – 0.25 mm/h.

Regime #3, from 12000 through 13800 s – 2.8 mm/h.

Regime #4, from 14100 through 14600 s – 7.8 mm/h.

2.2 Posttest analysis

2.2.1 Specimen temperature condition

Like in MC10, calculations of the specimen temperature condition was preceded by calculations of the electromagnetic system and of the molten pool thermal hydrodynamics. Tab. 2.3 contains the results of the electromagnetic system calculations, and Fig. 2.9 presents the results of thermal hydrodynamic calculations of the heat flux distribution along the specimen top radius during regimes ## 2÷4.

Table 2.3 – Results of calculations

regime No	Time, s	Q_{melt}, kW	ρ_2, $\Omega\times$cm	a_2, mm	x, mm
2	4000-11500	19.26	6.77e-2	60	2
3	12000-13800	21.29	6.88e-2	61.5	1.5
4	14100-14600	25.62	5.85e-2	64.5	1.5

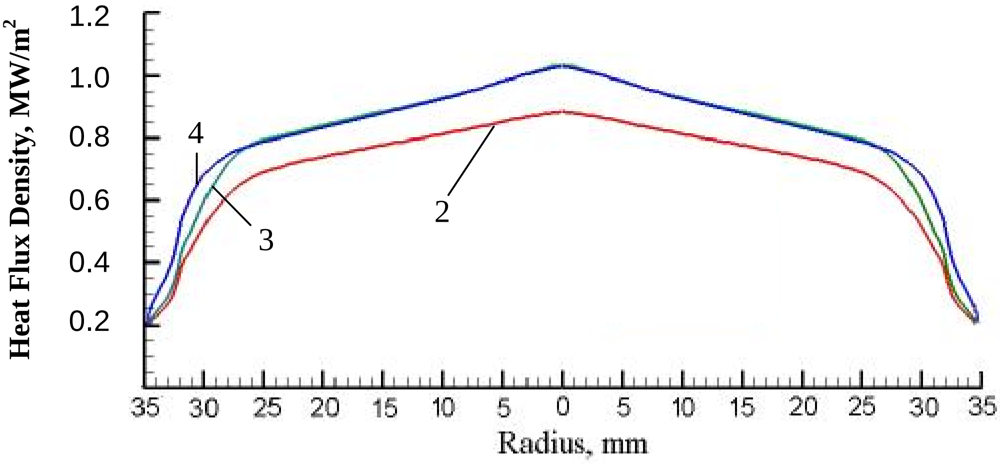

Fig. 2.9 – Radial distribution of heat flux density at the specimen upper top, regimes ## 2, 3, 4

A peculiarity of MC11 is in the monotonic growth of temperature during regimes ##3 and 4, as well as a notable history of the temperature at the interaction interface due to a comparatively rapid advance of the interface inside the specimen at the expense of corrosion. To take these factors into account, the specimen temperature condition was calculated twice for each regime, i.e. for its beginning and end. Then, taking the current position of the corrosion front into consideration, its temperature was determined (in the US sensor ∅15 sighting spot), and averaged for each regime. The same refers to the heat flux density.

Due to the loss of US data for regime #1, the exposure under stationary conditions from ~2500 through 3500 s at ~900°C at the specimen top happened to be unrepresentative. Therefore, in order to determine the characteristic temperature of the specimen corrosion front that would correspond to the average corrosion rate before the beginning of regime #2, a series of calculations has been performed for different temperature conditions of the specimen in accordance with Fig. 2.2. Averaging has been done taking into account duration of each temperature section and the characteristic average temperature in question obtained for the specimen at the corrosion front within the time interval from 700 through 4000 s. Though air was replaced by steam atmosphere only starting from ~1750 s, steam and air were assumed to be equal under the experimental conditions from the point of view of corrosion rate. This assumption was later confirmed when generalizing the experimental data. In the said series of calculations the heat flux distribution along the specimen radius was assumed to be the same as during regime #2 (Fig. 2.9). The technique of calculating the specimen temperature condition did not differ from that employed in MC10.

Fig. 2.10 shows the calculated distribution of temperature in the specimen in comparison with the experimental data. The satisfactory accuracy of calculations is obvious.

The temperatures and heat flux densities obtained as described above, as well as the calculated and experimental values of power into the specimen top calorimeter are summarized in Tab. 2.4.

Table 2.4 – Temperature and thermal parameters of the specimen

Regime No	**Temperature at the corrosion front, °C**			**Heat flux density at the corrosion front, MW/m^2**			**Power into the top calorimeter, kW**			
	beginning	**end**	**average**	**beginning**	**end**	**average**	**beginning**		**end**	
							calculated	**test**	**calculated**	**test**
1			950			0.99				
2	1060	1040	1050	1.18	1.15	1.16	0.99	1.24	0.98	1.11
3	1125	1135	1130	1.25	1.21	1.23	1.07	1.13	1.17	1.20
4	1220	1180	1200	1.34	1.24	1.29	1.26	1.27	1.28	1.30

T, °C T, °C

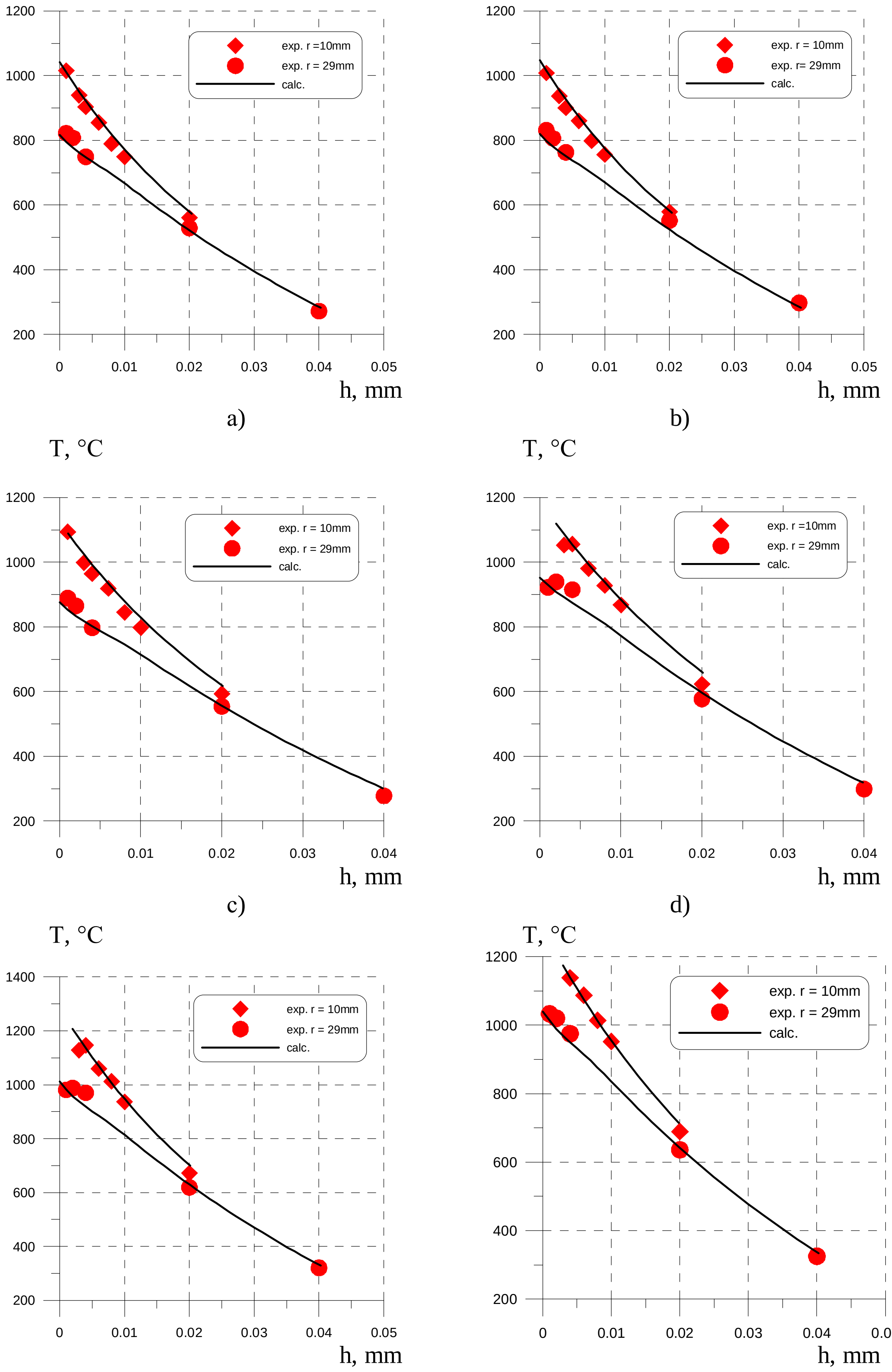

a – regime #2 beginning; b – regime #2 end; c – regime #3 beginning;
d – regime #3 end; e – regime #4 beginning; f – regime #4 end

Fig. 2.10 – Axial distribution of temperature in the specimen

2.2.2 Physicochemical analysis

There was no methodological difference between the posttest analyses for MC11 and MC10, and the present section contains only the obtained results.

2.2.2.1 Ingot macrostructure

After cooling, the specimen and ingot were embedded in epoxy together with the crucible, because the previous test has shown that the corium ingot fused in steam is characterized by a very high fissuring and fragility which prevent its safe extraction from the furnace together with the specimen without destruction. Then this assembly was cut along the axis for posttest analyses. Figs. 2.11 and 2.12 show the crucible after the test and the longitudinal section of the specimen and corium ingot.

Fig. 2.11 – Crucible after the test

Fig. 2.12 – Longitudinal section of the specimen and corium ingot

2.2.2.2 Material balance of MC11

Table 2.5 –MC11 material balance

Introduced into the melt, g		**Collected after the test, g**	
Corium from Pr- MC11 - <50 µm fraction *	1257.2	Rod sample**	4.6
U_3O_8	133.1	Crust	14.7
ZrO_2	41.8	Aerosols	38.6
metallic Zr	10.0		
FeO	80.1	Ingot	1489.6
Σ	**1522.2**	**Σ**	**1547.5**
Debalance	**+25.3**		

*) Corium had been produced in a special pretest and was used both as crust and main charge. Corium composition is given in Tab. 2.6.

**) The molten pool depth measuring with a tungsten rod resulted in a simultaneous melt sample hardening on the latter.

Table 2.6 – Physicochemical analysis of an average sample from the ingot produced in Pr-MC11

Determination method	**XRF**				**Chemical analysis**			
Element	**U**	**Zr**	**Fe**	**O**[1)]	U^{+4}	U^{+6}	Fe^{+2}	Fe^{+3}
Ingot average sample, mass %	50.45	18.28	13.69	17.58	46.76	4.64	12.31	1.11

1)- from residue.

2.2.2.3 Chemical analysis of the fused products from MC11

Four temperature regimes were maintained at the specimen top in MC11. During each regime, the condensed steam together with aerosols was gathered into collectors numbered according to each regime. The collectors were weighed and condensate was evaporated from them. Then the dry residue that corresponded to the quantity of aerosols at a certain regime, was weighed and subjected to both chemical analysis and XRF.

Tab. 2.7 offers the results of samples' chemical analysis. The process of evaporation could have influenced the oxygen potential of Fe and U oxides, therefore Tab. 2.7 gives the total content of Fe and U.

Table 2.7 – Chemical analysis of fused products from MC11

Sample	**Content, mass %**			
	Fe^{2+}	**Fe^{3+}**	**U^{4+}**	**U^{6+}**
Corium ingot average sample	14.6	2.6	45.3	0.7
Rod sample	15.8	0.7	48.1	0
Aerosols from collector #1	3.7		77.3	
Aerosols from collector #2	4.4		73.6	
Aerosols from collector #3	4.1		44.4	
Aerosols from collector #4	4.3		49.5	

The obtained results draw attention to the degrees of U and Fe oxidation in the melt. Small quantities of Fe^{3+} and U^{6+} may suppose that the hydrogen that forms at steam thermolysis dissolves in the melt well, and it leads to the reduction of the melt oxygen potential.

2.2.2.4 XRF of the fused products from MC11

Tab. 2.8 contains the XRF results and per-element mass balances, as the most comprehensive analysis for all elements has been performed by this method in both MC10 and MC11.

2.2.2.5 Fused corium density in MC11

In the same way as in MC10, the profilogram (see Fig. 2.28) was used in MC11 for determining the amount of steel that had transited during the test into the melt from the steel specimen (equal to the volume of the pore), which amounted to 3.5(±0.6) cm^3. Density of steel is close to that of metallic iron (7.87 g/cm^3), and the mass of iron that had transited into the melt was calculated to be ~27.5÷32.3 g. Experimentally, Fe (Cr, Ni, Mn) totaling 31.3 g were discovered in the fused products, and it agreed with the calculations well. Like in MC10, debalance for the main elements (U, Zr) was small and in the present case was below 1%, i.e. within the error limit of the applied analytical methods.

The bottle density of fused corium with 100-200 μm particle size was 7.2 g/cm^3

Table 2.8 – XRF results for the fused products and per-element mass balance for MC11

Sample	U	Zr	Fe	Cr	Ni	Mn	O1)	Fused product mass, g	U	Zr	Fe	Cr	Ni	Mn	O1)
	mass.%								g						
Corium ingot average sample	47.5	17.4	16.4	0.10	0.69	0.05	17.9	1489.6	707.6	259.8	243.7	1.5	10.3	0.7	266.0
Rod sample	47.5	17.3	17.6	0.00	0.00	0.00	17.6	4.6	2.2	0.8	0.8	0.0	0.0	0.0	0.8
Crust	55.6	16.3	11.4	0.10	0.00	0.00	16.6	14.7	8.2	2.4	1.7	0.0	0.0	0.0	2.4
Aerosols, condensate #11)	76.8	1.2	5.4	0.00	0.00	0.00	16.6	0.2	0.2	0.0	0.0	0.0	0.0	0.0	0.0
Aerosols, condensate #2	76.4	1.0	5.5	0.00	0.00	0.00	17.2	1.8	1.4	0.0	0.1	0.0	0.0	0.0	0.3
Aerosols, condensate #3	75.5	1.0	6.3	0.10	0.00	0.00	17.1	0.6	0.4	0.0	0.0	0.0	0.0	0.0	0.1
Aerosols, condensate #4	75.4	2.2	7.1	0.10	0.10	0.00	15.1	0.8	0.6	0.0	0.1	0.0	0.0	0.0	0.1
LAF	68.0	0.1	15.3	0.33	0.20	0.10	16.0	31.3	21.3	0.0	4.8	0.1	0.1	0.0	5.0
MAF	88.1	0.00	0.00	0.00	0.00	0.00	11.9	3.9	3.5	0.0	0.0	0.0	0.0	0.0	0.5
Collected in the end of the test								1547.5	745.2	263.1	251.2	1.6	10.3	0.8	275.3
Introduced into the melt								1522.2	747.1	270.8	232.6				271.7
Δ								+25.3	+1.9	+7.7	+18.6	+1.6	+10.3	+0.8	-3.5

1) - O and impurities determined from the residue.

.

2.2.2.6 The SEM/EDX

The SEM/EDX of corium ingot

A template from the ingot oxidic part longitudinal section has been prepared for the SEM/EDX. The analysis of the studied template bulk composition established the absence of noticeable changes (see Tab. 2.9, area 1 SQ1, Tab. 2.10 area 2 SQ1, Tab. 2.12 area 5 SQ1). Three phases may be identified in the crystallized ingot: a uranium-based solid solution $(UZr)O_{2+x}$ with a small content of iron; a zirconium-based solid solution $(ZrU)O_{2+x}$ with a small content of iron; and FeO_y (Tab. 2.9, points P1, P2, P4, respectively).

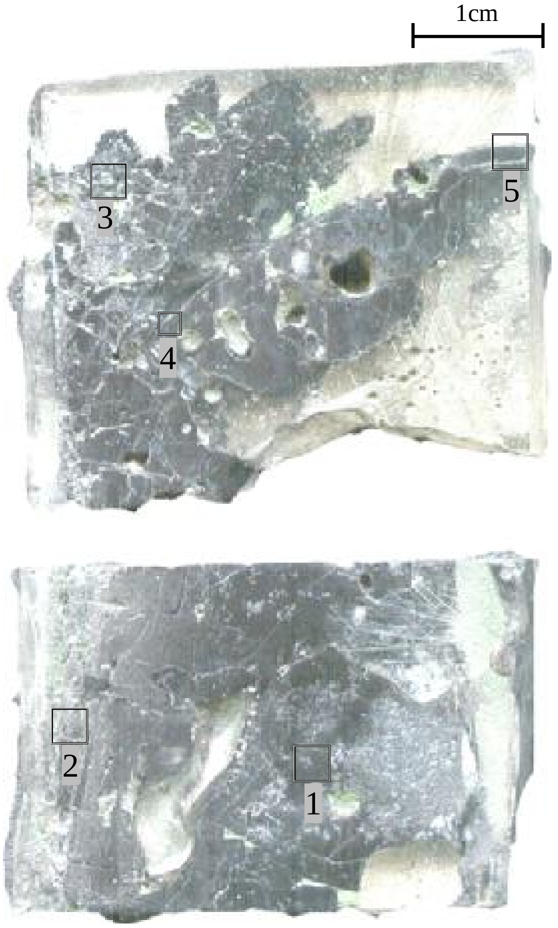

Fig. 2.13 – Longitudinal section of the ingot oxidic part from MC11 with regions marked for the SEM/EDX

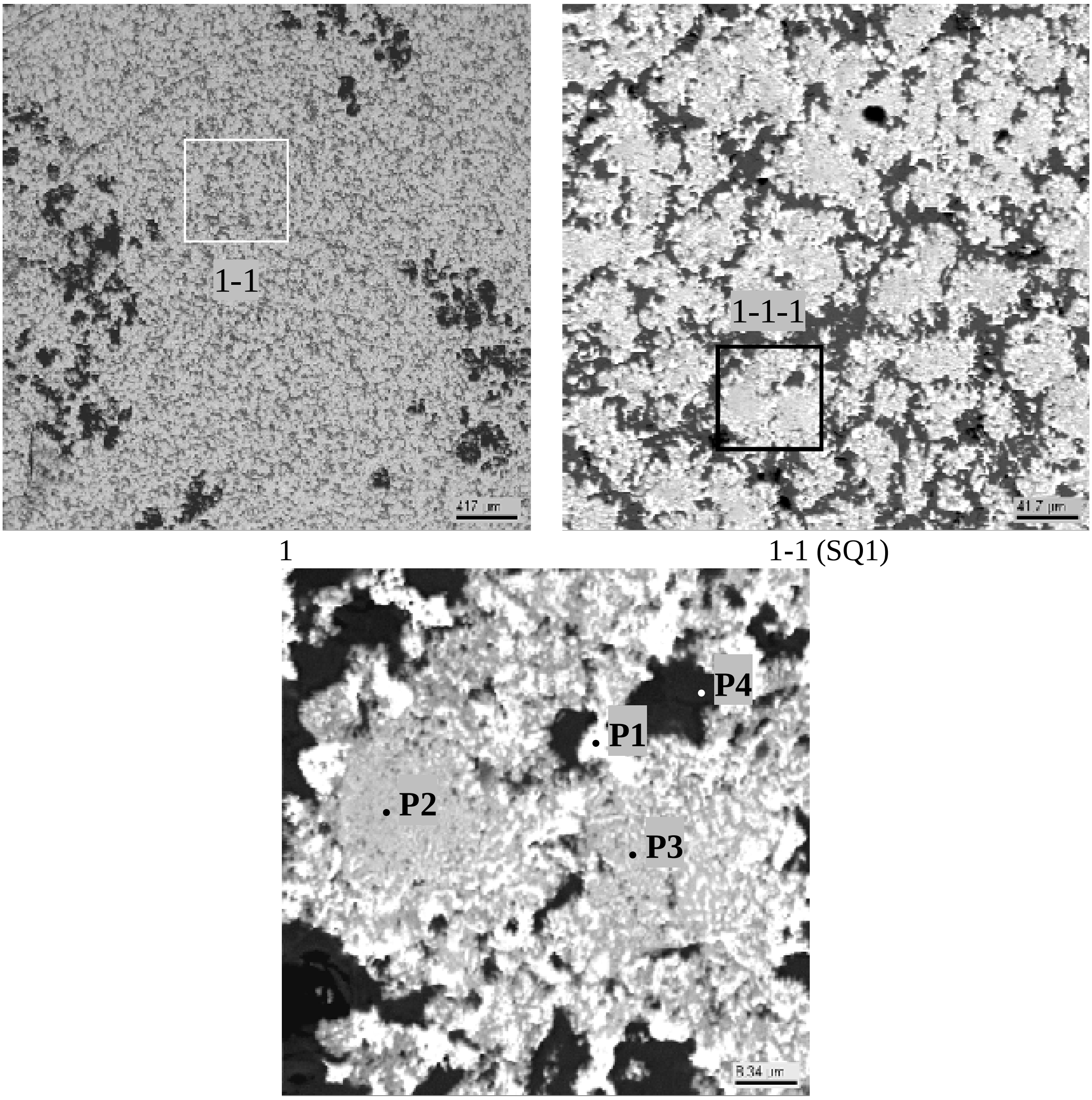

1 1-1 (SQ1)

1-1-1

Fig. 2.14 – Micrographs of region 1

Table 2.9 – Data on region 1 EDX analysis

No		U	Zr	Fe	~O
SQ1	mass %	38.08	12.25	21.85	27.31
	mol.%	6.63	5.57	16.23	70.81
	mol.% MeO_x	22.73	19.07	55.60	
P1	mass %	72.25	4.30	3.36	19.90
	mol.%	18.27	2.84	3.62	74.85
	mol.% MeO_x	72.63	11.27	14.38	
P2	mass %	40.47	21.20	6.94	30.77
	mol.%	6.88	9.40	5.03	77.80
	mol.% MeO_x	30.98	42.34	22.64	
P3	mass %	43.79	21.74	5.24	29.04
	mol.%	7.87	10.19	4.02	77.64
	mol.% MeO_x	35.20	45.60	17.97	
P4	mass %	2.53	1.16	61.04	34.94
	mol.%	0.32	0.38	33.01	65.93
	mol.% MeO_x	0.94	1.12	96.88	

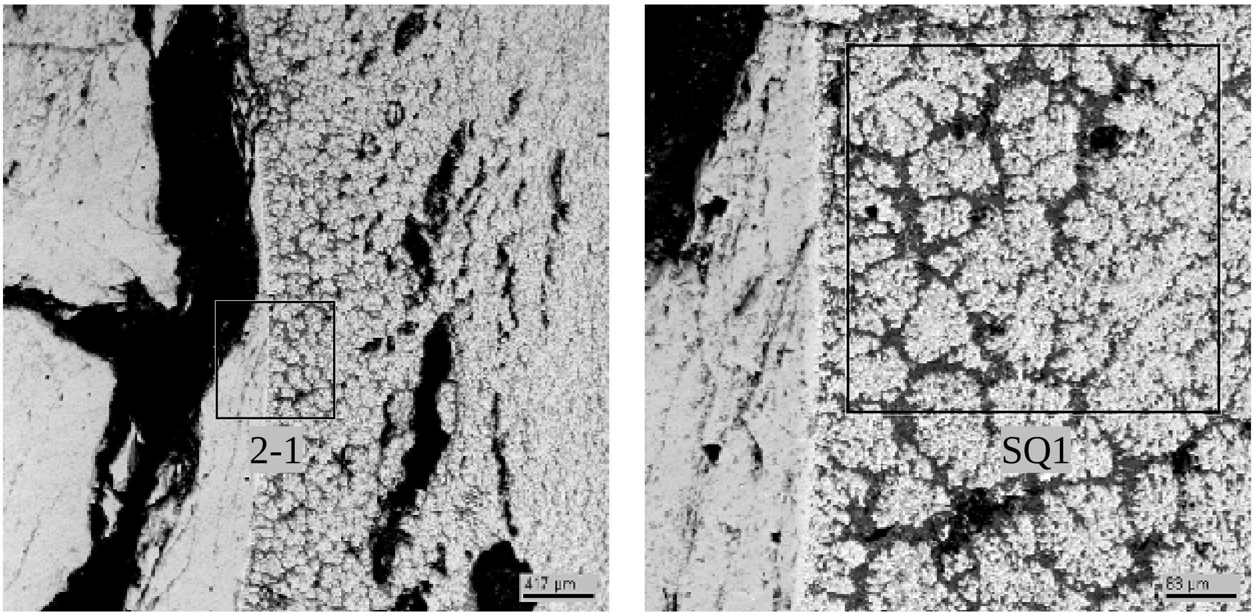

2 2-1 (SQ1)

Fig. 2.15 – Micrographs of region 2

Table 2.10 – Data on region 2 EDX analysis

No		U	Zr	Fe	~O
SQ1	mass %	39.72	10.54	20.96	28.23
	mol.%	6.83	4.73	15.37	72.25
	mol.% MeO_x	24.63	17.05	55.38	

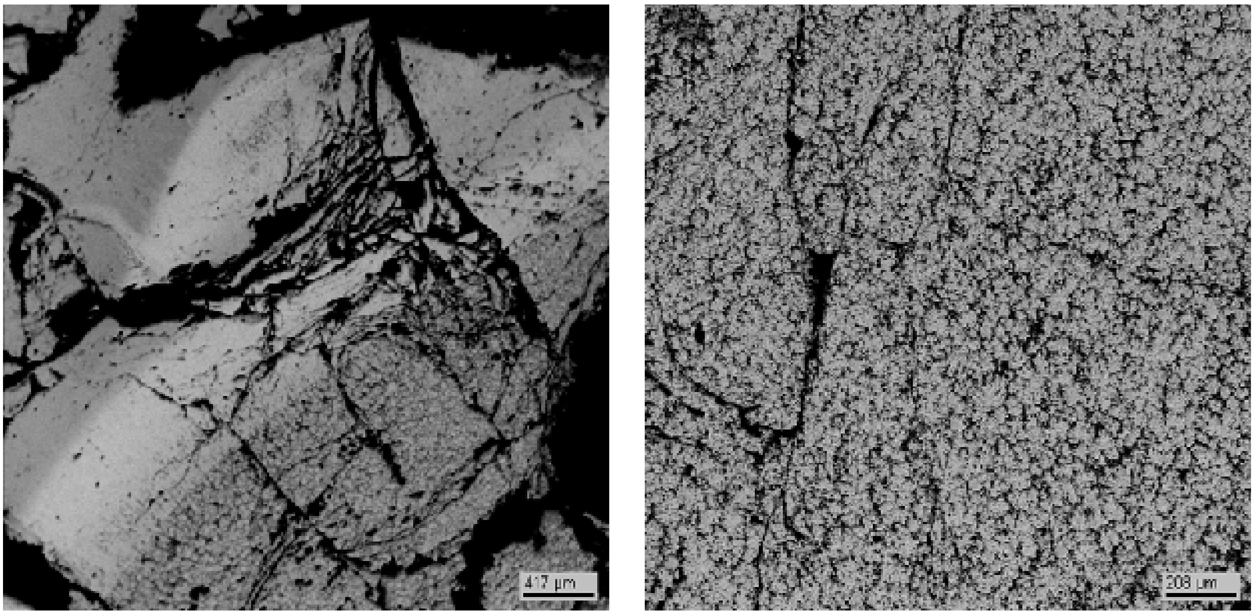

3 4(SQ1)

Fig. 2.16 – Micrographs of regions 3 and 4

Table 2.11 – Data on region 4 EDX analysis

No		U	Zr	Fe	~O
SQ1	mass %	37.77	10.16	19.75	31.83
	mol.%	6.03	4.23	13.44	75.63
	mol.% MeO_x	24.75	17.36	55.15	

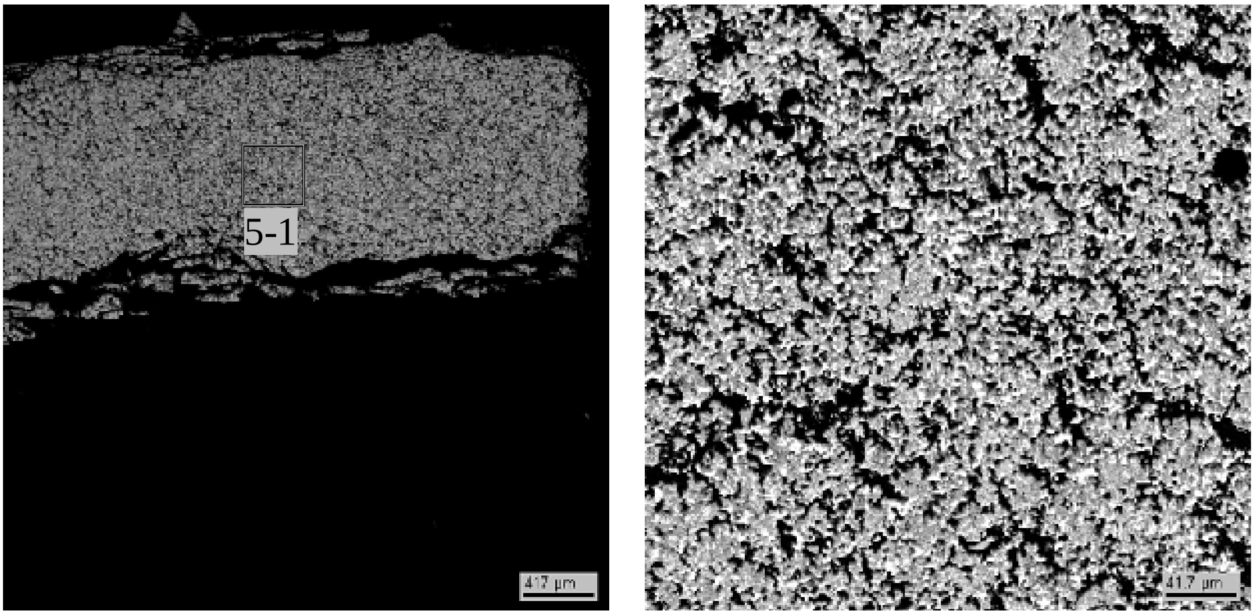

5 5-1 (SQ1)

Fig. 2.17 – Micrographs of region 5

Table 2.12 – Data on region 5 EDX analysis

No		**U**	**Zr**	**Fe**	**~O**
SQ1	mass %	39.03	11.21	23.49	25.78
	mol.%	7.02	5.26	18.00	68.98
	mol.% MeO_x	22.63	16.96	58.03	

The SEM/EDX of the corium/steel specimen interaction zone

A template from the longitudinal section of the ingot metallic part has been prepared for the SEM/EDX. Fig. 2.18 shows the template with regions marked for examination. Two characteristic layers may be noted at the interaction boundary. The first one, the corrosion layer adjacent to the metal, consists of the FeO phase (area 3 Tab. 2.16 P2) and small inclusions containing U and Zr. Obviously, these are eutectic inclusions that characterize the interaction between solid crust composed of $(UZr)O_{2+x}$ and the FeO layer. Further goes a layer (Fig. 2.23 region 6-1-1), which we believe to have been the crust layer. Notable is that this layer is more depleted in iron oxide that the melt (see Tab. 2.17 SQ1 and SQ2). A possible reason of the said structure formation at the interaction boundary is as follows: it was noted in Sect. 2.1.4 that shortly before the end of regime #4 an abrupt spontaneous growth of the specimen temperature was recorded. We attribute this to the disruption of the crust integrity. After stepping down power in the melt, molten corium crystallization has occurred on the specimen surface. According to the phase diagram of the UO_{2+x}-ZrO_2-FeO_y ternary system, the solid solution of iron $(UZr)O_{2+x}$, depleted in iron oxides, is the first to crystallize. A thin surface layer of FeO forms during the short (before the generator switching off) time of steel corrosion.

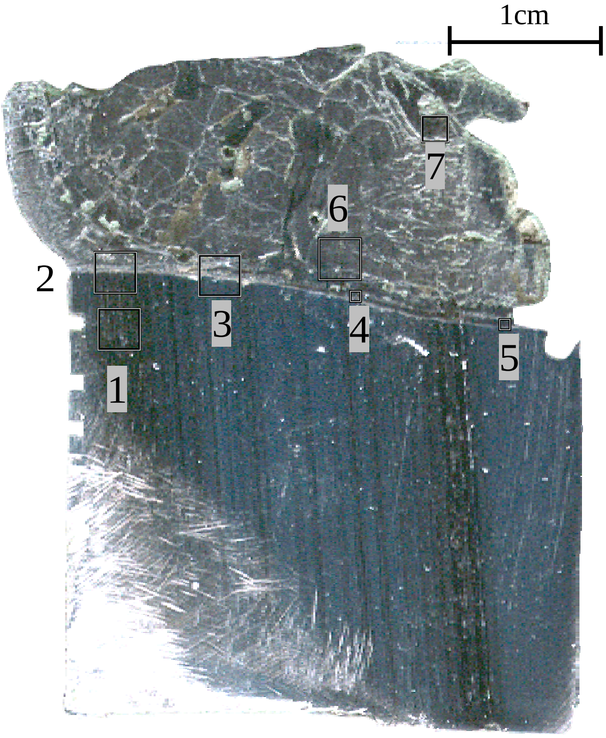

Fig. 2.18 – Longitudinal section of the ingot metallic part with the interaction boundary from MC11 with regions marked for the SEM/EDX

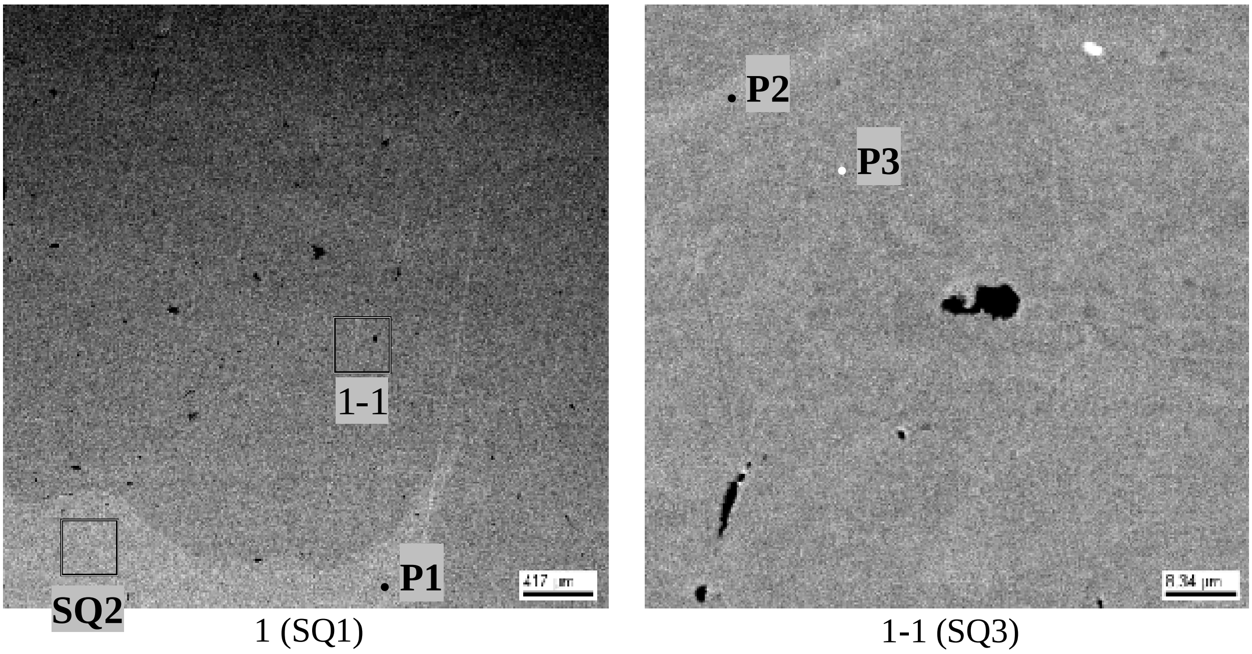

1 (SQ1) 1-1 (SQ3)

Fig. 2.19 – Micrographs of region 1

Table 2.13 – Data on region 1 EDX analysis

No		Fe	Cr	Ni	Mn	~O
SQ1	mass %	86.50	2.11	1.25	0.53	8.62
	mol.%	71.07	1.86	0.98	0.44	24.71
	mol.% MeO_x	94.40	2.47	1.30	0.59	
SQ2	mass %	93.70	2.20	1.41	0.50	1.13

	mol.%	90.88	2.29	1.30	0.49	3.82
	mol.% MeO$_x$	94.49	2.38	1.35	0.51	
SQ3	mass %	94.52	2.34	1.43	0.62	-
	mol.%	94.23	2.51	1.36	0.63	-
P1	mass %	93.62	2.49	1.34	0.44	0.97
	mol.%	91.19	2.61	1.24	0.44	3.29
	mol.% MeO$_x$	94.29	2.70	1.28	0.45	
P2	mass %	94.01	2.37	1.29	0.50	0.79
	mol.%	91.87	2.49	1.20	0.49	2.70
	mol.% MeO$_x$	94.42	2.56	1.24	0.51	
P3	mass %	94.46	2.49	1.47	0.44	-
	mol.%	94.25	2.67	1.39	0.45	-

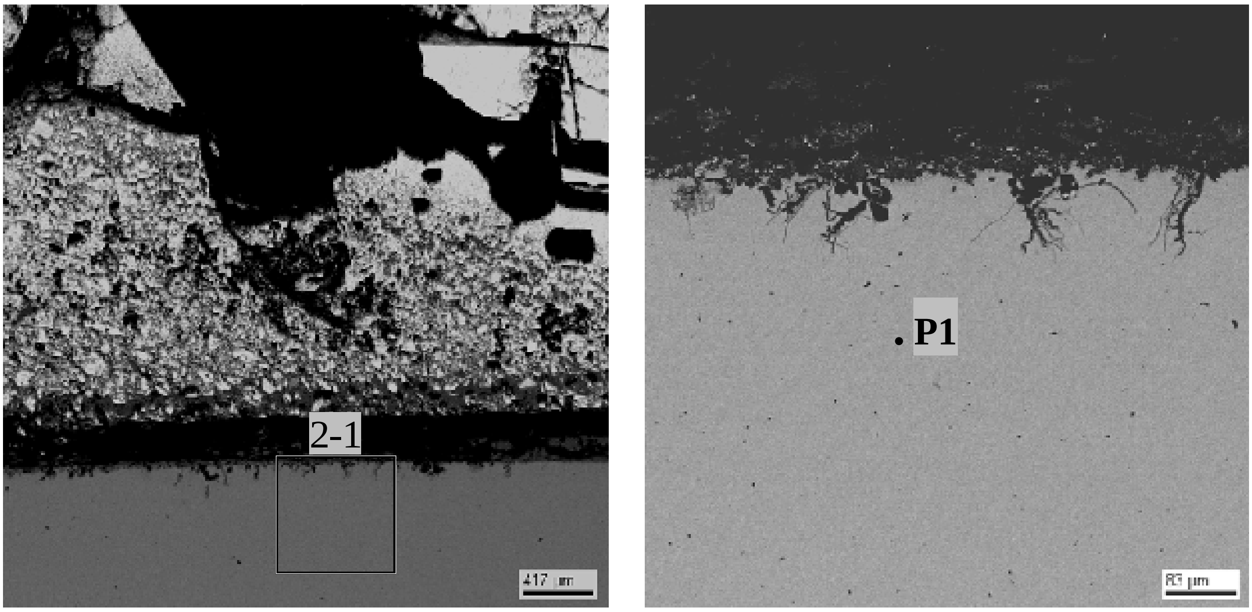

2 2-1

Fig. 2.20 – Micrographs of region 2

Table 2.15 – Data on region 2 EDX analysis

№		Fe	Cr	Ni	Mn	~O
P1	mass %	94.65	2.36	1.22	0.68	-
	mol.%	94.38	2.53	1.16	0.69	-

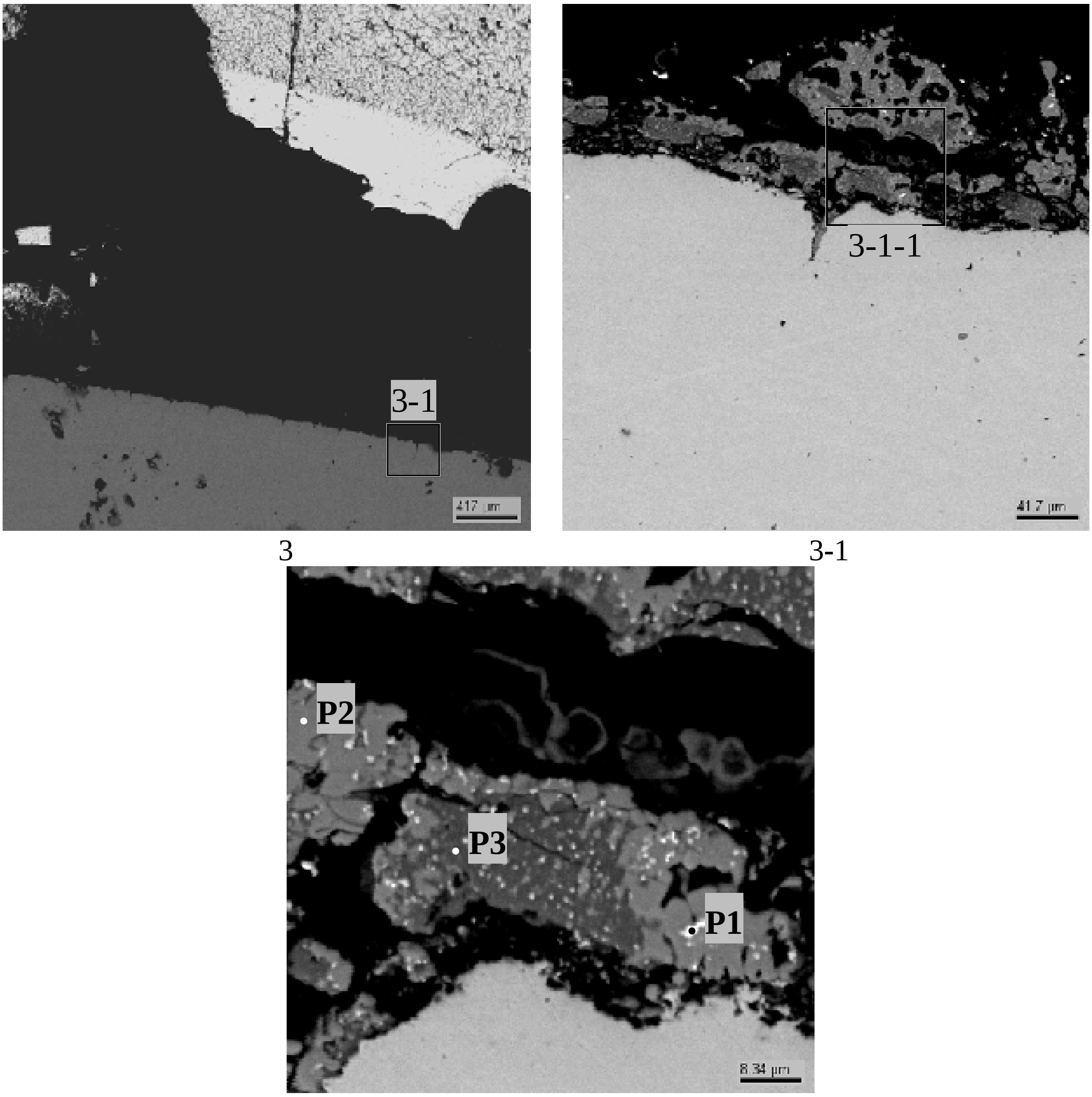

3 3-1

3-1-1

Fig. 2.21 – Micrographs of region 3

Table 2.16 – Data on region 3 EDX analysis

No		U	Zr	Fe	Cr	Ni	Mn	~O
P1	mass %	20.91	1.11	46.24	4.82	8.79	0.34	15.75
	mol.%	4.01	0.55	37.80	4.23	6.84	0.28	44.95
	mol.% MeO_x	7.29	1.01	68.66	7.69	12.42	0.52	
P2	mass %	-	0.29	69.99	1.53	-	-	27.90
	mol.%	-	0.10	41.22	0.97	-	-	57.36
	mol.% MeO_x	-	0.24	96.67	2.27	-	-	
P3	mass %	-	-	52.70	2.28	0.66	0.58	30.05
	mol.%	-	-	28.10	1.30	0.33	0.32	55.92
	mol.% MeO_x	-	-	63.74	2.96	0.76	0.72	

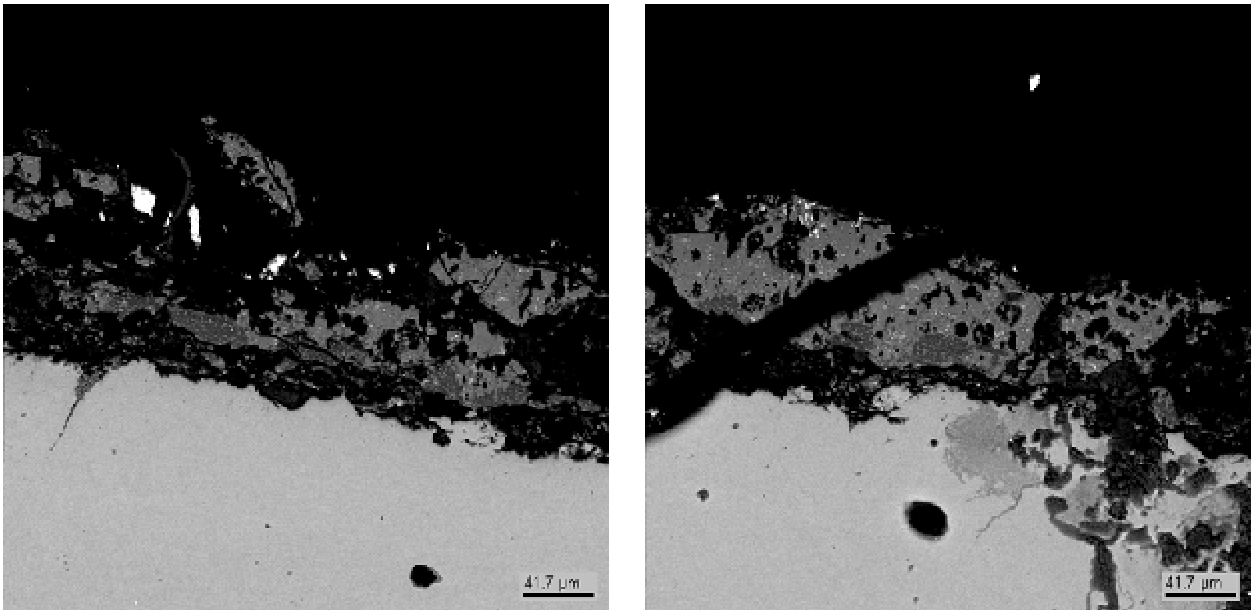

4 5

Fig. 2.22 – Micrographs of region 4 и 5

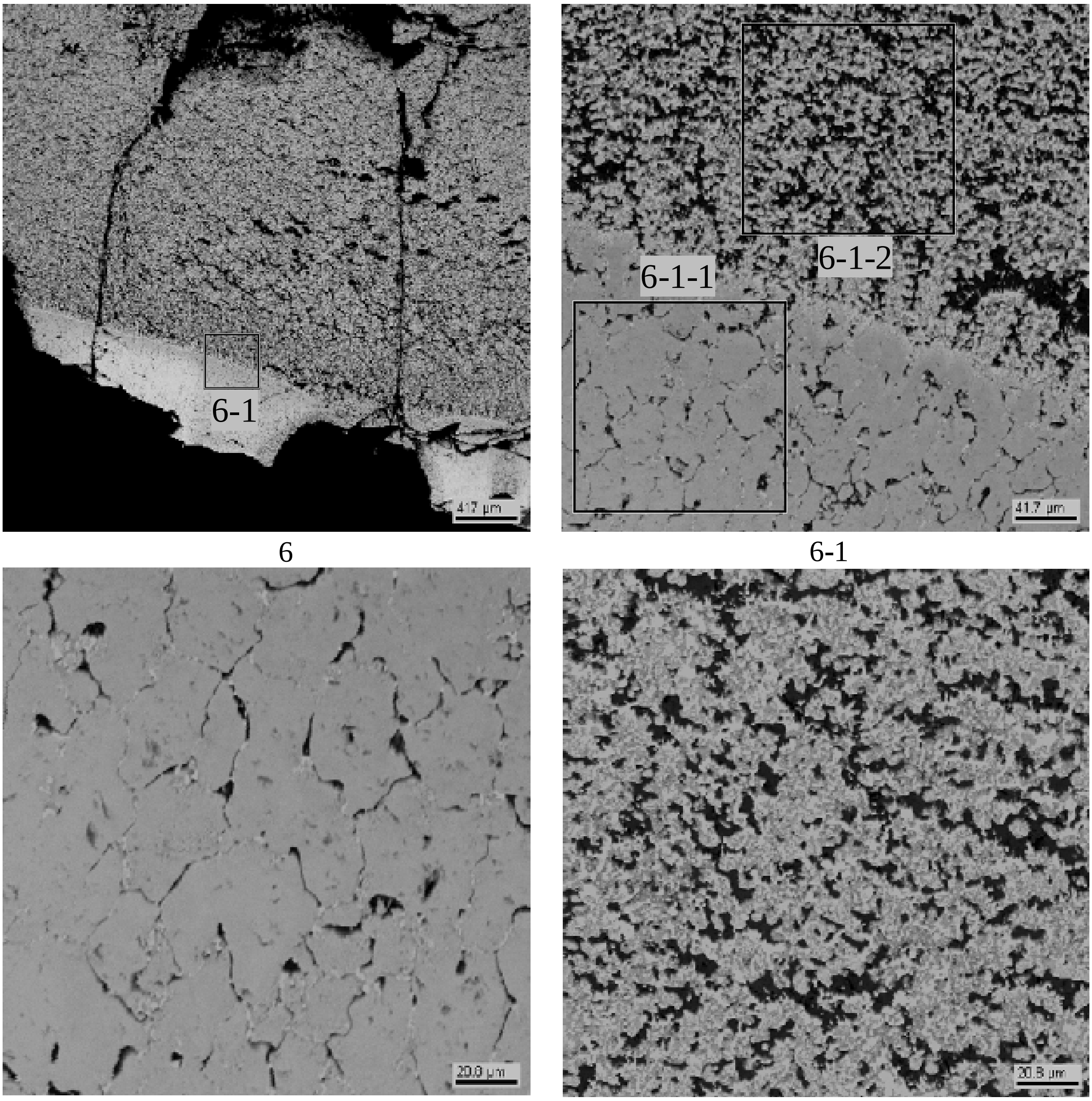

6 6-1

6-1-1 (SQ1) 6-1-2 (SQ2)

Fig. 2.23 – Micrographs of region 6

Table 2.17 – Data on region 6 EDX analysis

No		U	Zr	Fe	~O
SQ1	mass %	49.49	17.81	6.36	26.19
	mol.%	9.63	9.04	5.27	75.79
	mol.% MeO_x	39.77	37.34	21.78	
SQ2	mass %	45.19	12.18	20.71	21.58
	mol.%	9.24	6.49	18.05	65.63
	mol.% MeO_x	26.88	18.89	52.51	

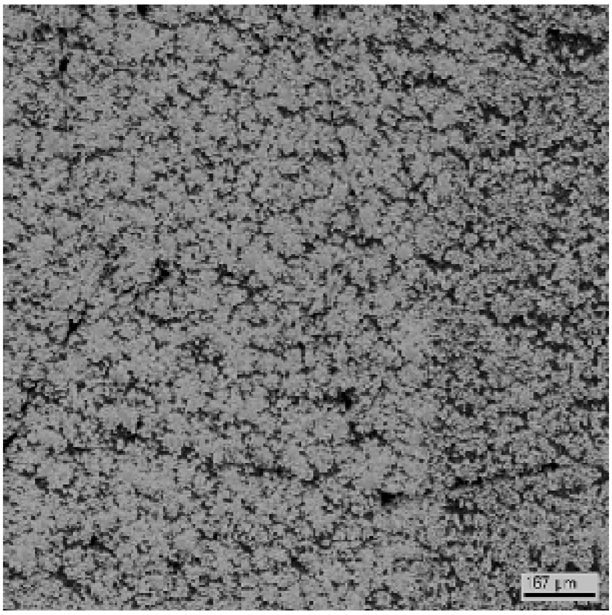

7 (SQ1)

Fig. 2.24 – Micrograph of region 7

Table 2.18 – Data on region 7 EDX analysis

No		**U**	**Zr**	**Fe**	**~O**
SQ1	mass %	41.21	10.90	23.90	23.54
	mol.%	7.84	5.41	19.38	66.63
	mol.% MeO_x	23.50	16.22	58.07	

2.2.2.7 Specimen metallography

Pre-test inspection of steel

Like for the tests MC5–MC10, the specimen for MC11 was made from 15Kh2NMFA-A vessel steel.

Metallographic pre-test inspection of the witness specimen included analysis of its macro- and microstructure, and microhardness measuring.

Metallographic investigations and microhardness measurements were performed in the same way as in the pervious tests and showed the initial microstructure of steel to consist of the finely-dispersed pearlite, and the integral microhardness of the witness specimen (H_μ) to be 250 ÷ 260 kgs/mm^2.

Initial specimen measurement

The dimensions were measured with the calipers with a scaling factor of 0.02 mm (20 µm) and the MBS-9 stereoscopic microscope with a 14 µm scaling factor and x50 magnification. The distance A from the upper top to the first groove, distance B to the reference hole axis and diameter D of the reference hole are given in Tab. 2.19. The points of measurements are shown in Fig. 2.25.

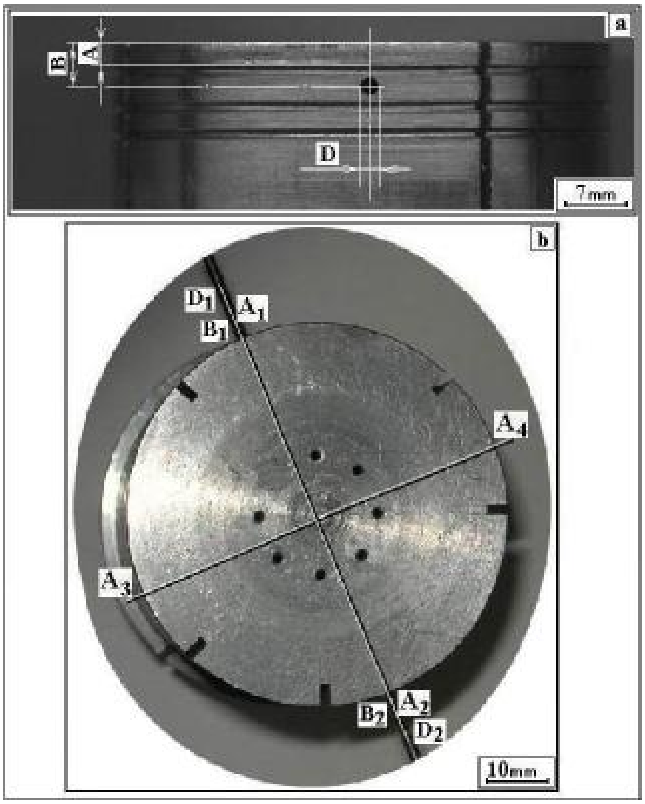

A (A_1, A_2, A_3, A_4), B (B_1, B_2), D (D_1, D_2) – points of measurements.

Fig. 2.25 – Fragments of steel specimen lateral surface (a) and upper top (b) before MC11

Table 2.19 – Steel specimen measurements (mm)

A_1	A_2	A_3	A_4	B_1	B_2	D_1	D_2
2.95	2.95	2.90	3.02	5.0	5.25	2.10	2.15

Specimen length L = 104.2 mm

These dimensions are important for the posttest determination of the initial top position and steel specimen corrosion depth.

Ingot macrostructure

A crust above the ingot and aerosol deposits on the crucible sections were discovered during the furnace disassembly. The extraction of corium ingot and steel specimen was done in three steps: (1) first the ingot upper top was embedded in epoxy, (2) then the steel specimen upper part and the oxidic ingot bottom part were coated with epoxy around the periphery thus fixing their relative position, and (3) all the block was embedded in epoxy after the crucible sections have been taken off the lateral surface. Cutting of the block along the axis in the A_3 – A_4 plane (see Fig. 2.25) yielded a template from the steel specimen and oxidic ingot longitudinal section. For determining qualitative and quantitative characteristics of ablation, a plate was cut from the template and a thin section produced from it for metallography and the SEM/EDX. The oxidic part was separated from the 2nd part of the block. Fig. 2.26 shows the steel specimen upper part and the steel specimen top plane after separation of the oxidic ingot.

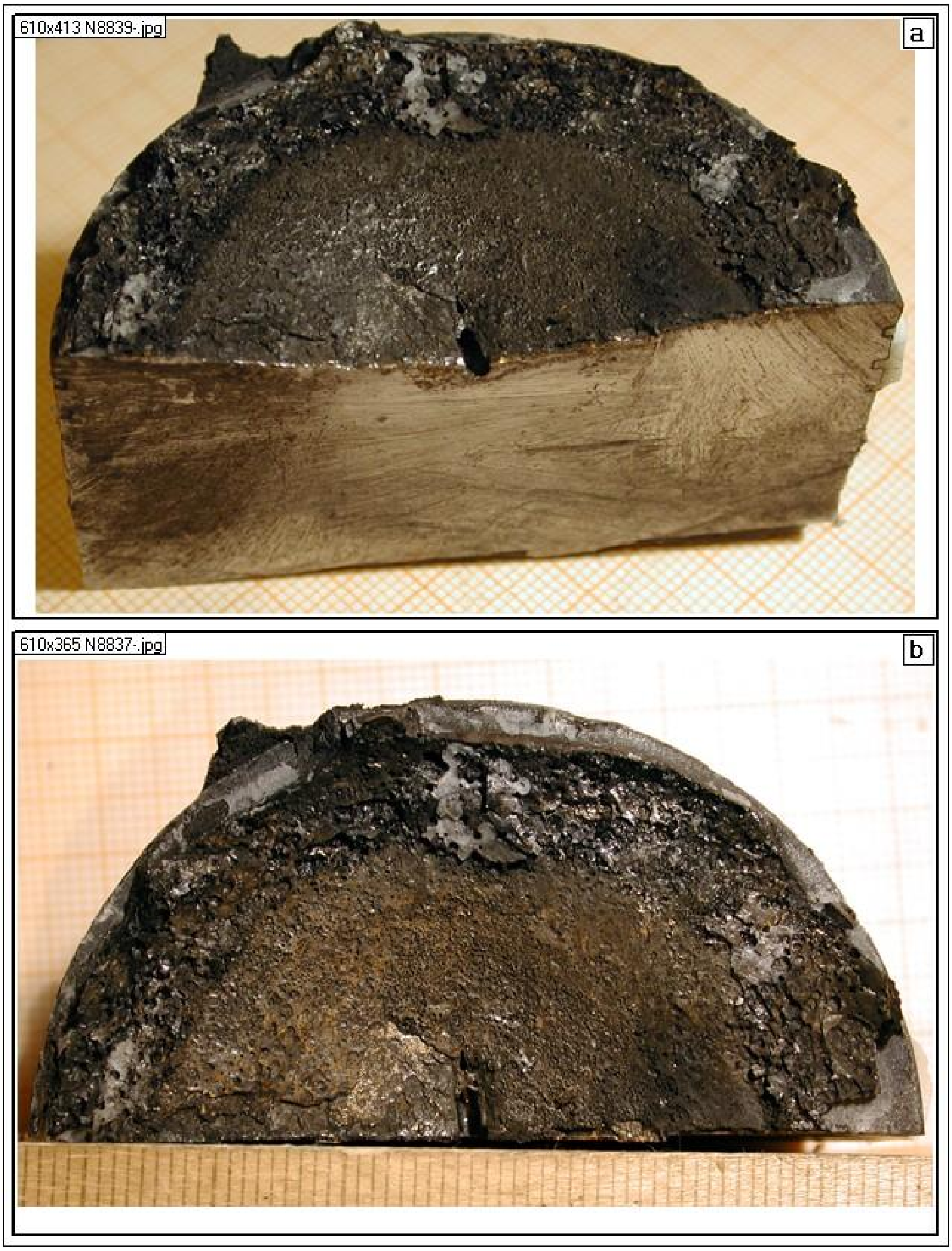

Fig. 2.26 – Steel specimen upper part and the steel specimen top plane after the oxidic ingot separation

Determination of steel ablation depth

Templates have been prepared from the oxidic corium and steel specimen after the test. The template of the steel specimen axial section was used for measuring the maximum depth of specimen ablation, determining boundary of the interaction zone and of changes in the macro- and microstructure of steel.

Fig. 2.27 shows macrostructure of the vessel steel specimen in the longitudinal section, of the thermal influence zone (lines 3 & 4), and of the regions (A-G) marked for microstructure examination in steel and corium.

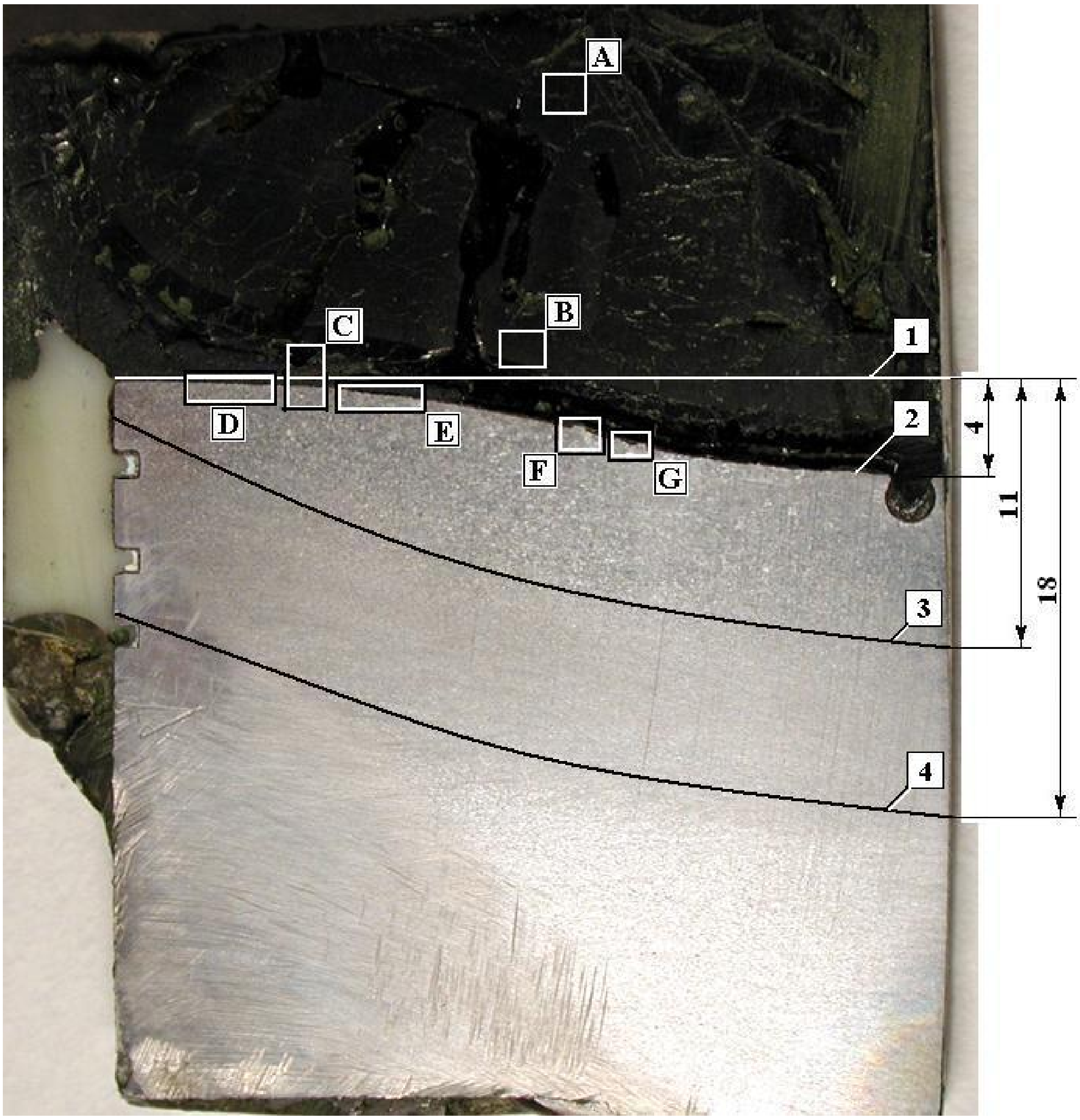

1- reference plane of the steel specimen initial upper top;
2- profile of specimen top after the test;
3- of molten corium thermal influence on steel macrostructure;
4- conventional boundary of changes in steel microstructure;
A–G – microsection areas where microstructure was photographed.

Fig. 2.27 – Longitudinal section of the oxidic ingot bottom part and steel specimen upper part

Direct measurements along the specimen longitudinal section were made using the PMT-3 microhardness tester at x180 magnification and the MBS-9 stereoscopic microscope at x50 and x100 magnifications. The scale factor of micrometer screws and object plate of microhardness tester is 0.01 mm (10 µm). The measurement error is ±10 µm; it was determined with the stage micrometer. The position of the initial top plane was determined from the groove made in the specimen lateral surface at the distance of 3.0 mm from the upper top. The images produced by processing macrosection photographs on the computer were used for plotting the steel specimen ablation diagram (Fig. 2.28, line 2). Dimensions marked in the profilogram are as follows: specimen width (diameter) – along the X-line; distance from the reference plane of the initial top – along the Y-line (top-down).

According to the results of measurements, the maximum depth of steel specimen corrosion amounted to 4.0 mm. In the US sensor sighting spot it was 3.7 mm (Fig. 2.28).

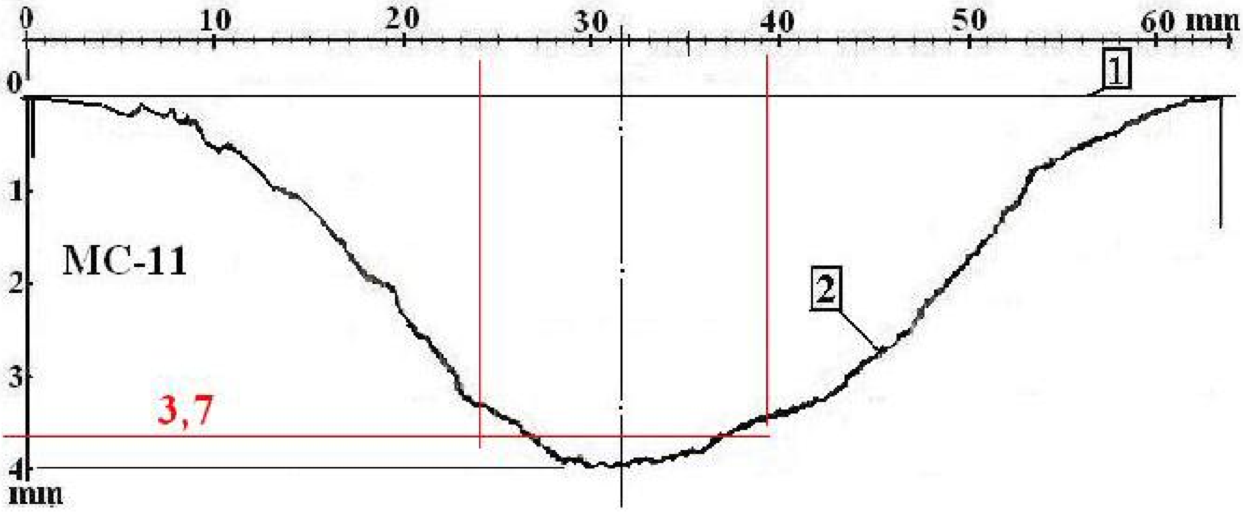

1 – reference plane of the steel specimen initial top;
2 – profile of specimen top after the test.

Fig. 2.28 - Profilogram of the steel specimen upper top in the axial section plane

Steel macro- and microstructure after the test

Grinding and polishing of the template was done according to the standard technique.

To reveal the microstructure, the prepared section was treated with etchants, and used metallographic microscopes for quality control. The combined use of etchants for the pearlitic and austenitic steels [17] displays both macro- and microstructure of the zone of molten corium high-temperature influence of steel and identifies microstructure of steel.

Sections' surfaces were photographed by a NIKON digital camera coupled with the METALLUX metallographic microscope at x200, x400 and x900 magnifications.

The area, within which structural transformations occurred in the specimen, spreads to a depth of 18 mm from its upper top.

The metallic and oxidic parts of the section in the longitudinal plane were subjected to microhardness measurements. The study employed the PMT-3 microhardness tester and was performed in compliance with requirements of the State Standard 9450 and the 'Procedural guidelines for the PMT-3 microhardness tester' (MI-244-82). At the loads of 50 g on the indentor, the diagonals of the diamond pyramid imprints were measured by the MOV-1-15^x eyepiece screw micrometer at x487 magnification. The value of microhardness was determined from 3 to 5 imprints made in each region of the metallic and oxidic parts of the section.

Figs. 2.29 - 2.32 show fragments of the corium microsection and steel microstructure in different zones of the template, marked by rectangles in Fig. 2.27.

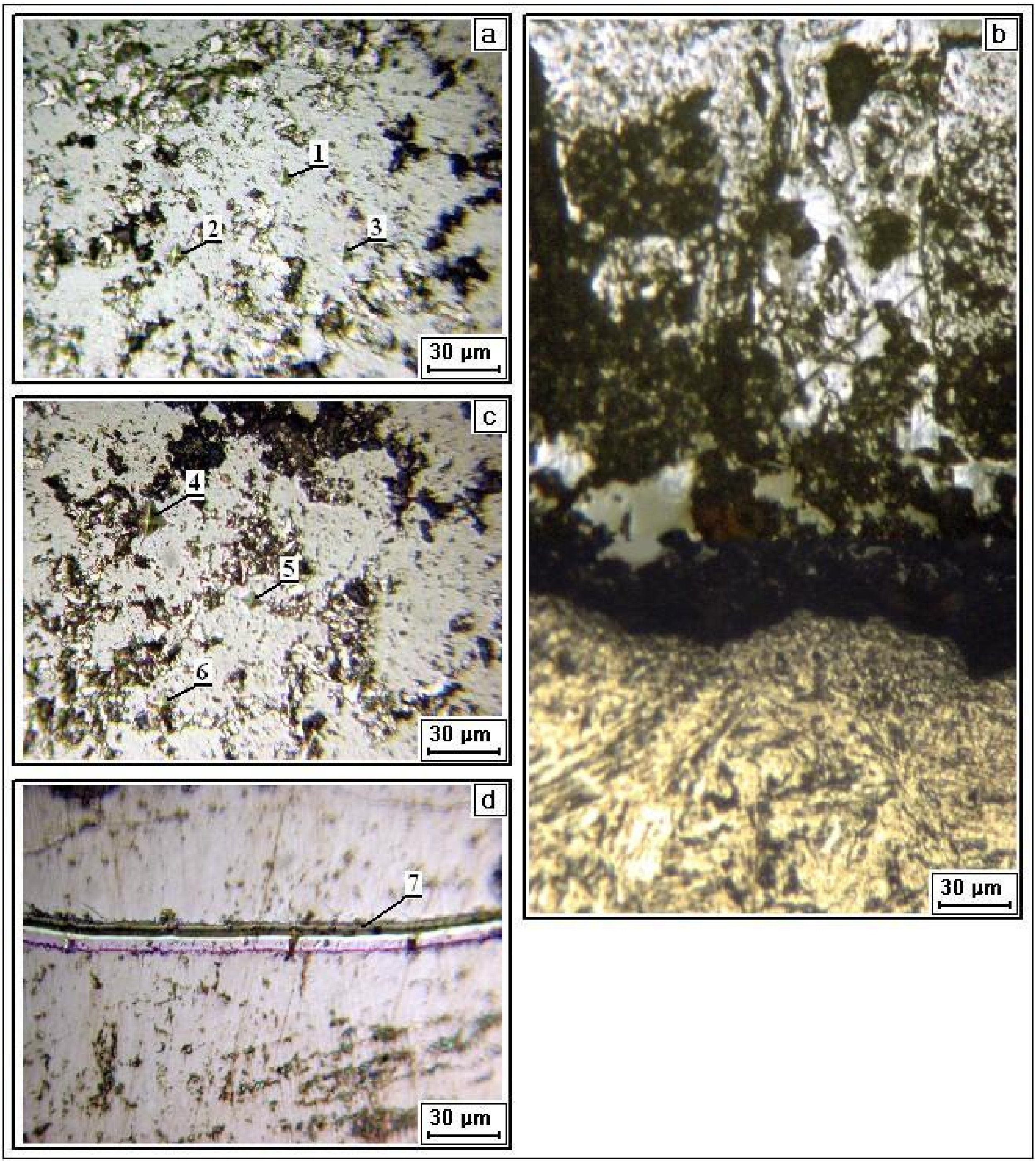

Fig. 2.29 – Fragments of corium microsections, areas A – a, c; B –d; C – b, c with diamond pyramid imprints (1 – 7)

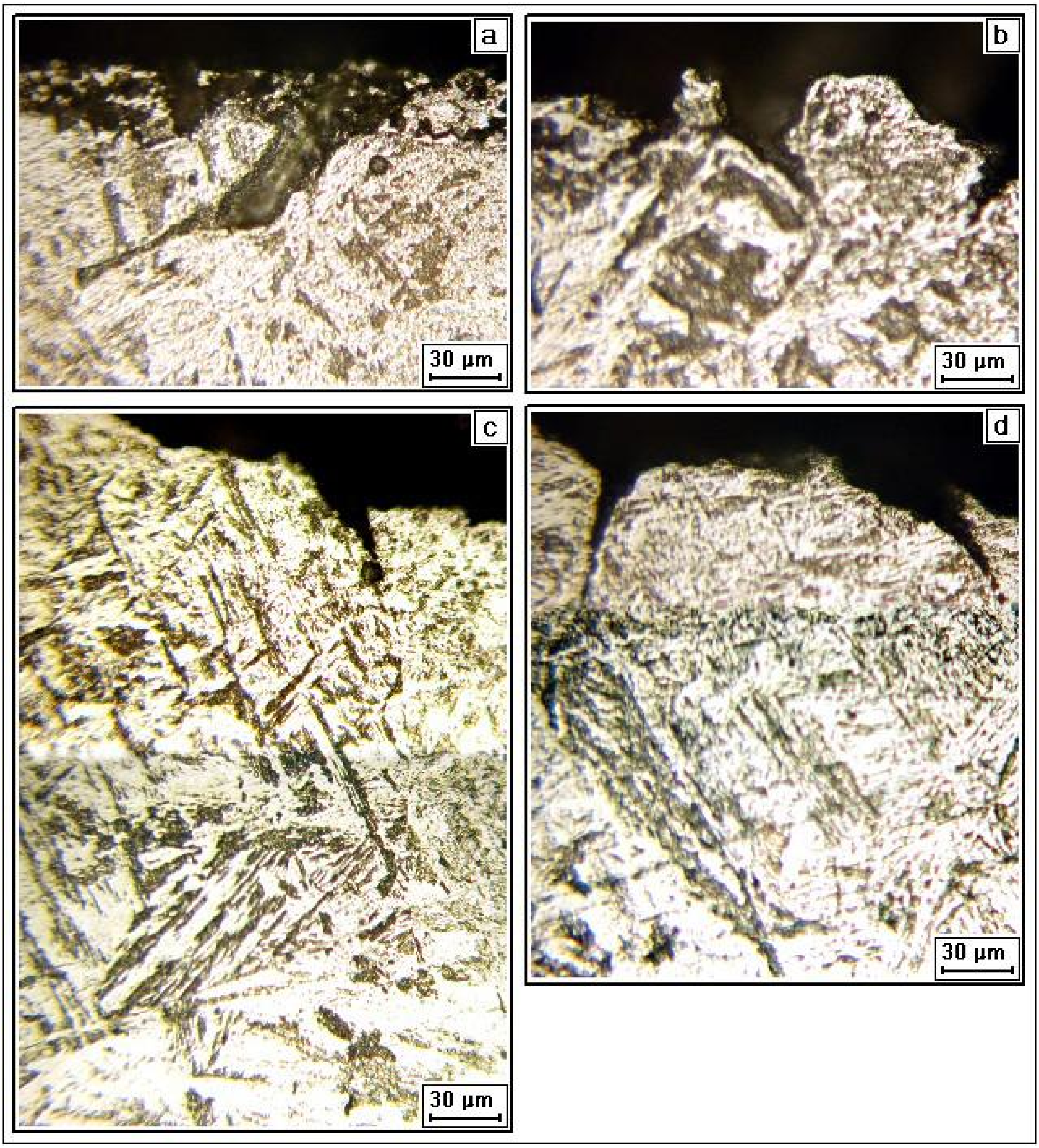

Fig. 2.30 - Steel microstructure near the top surface, area (D)

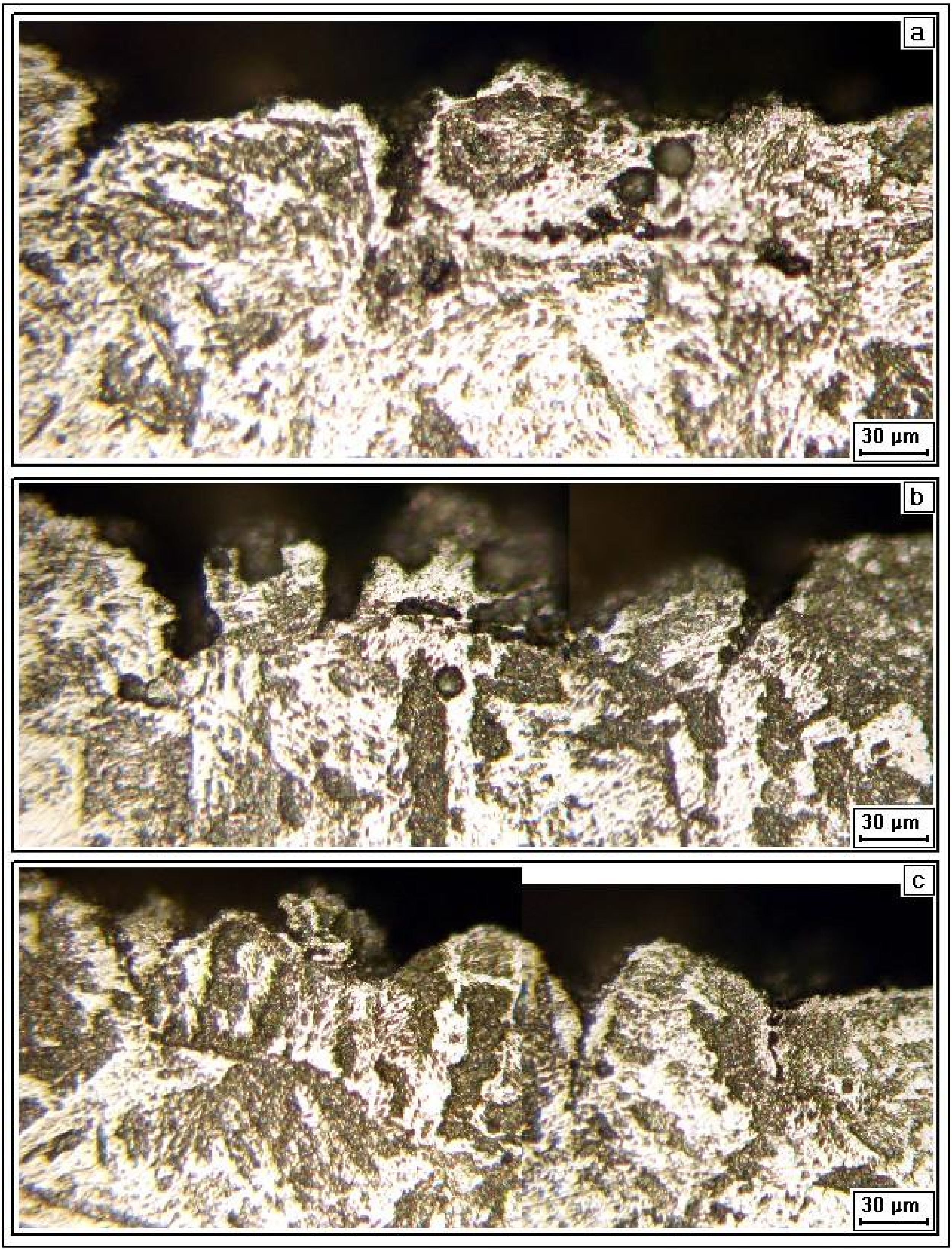

Fig. 2.31 - Steel microstructure near the top surface, area (E)

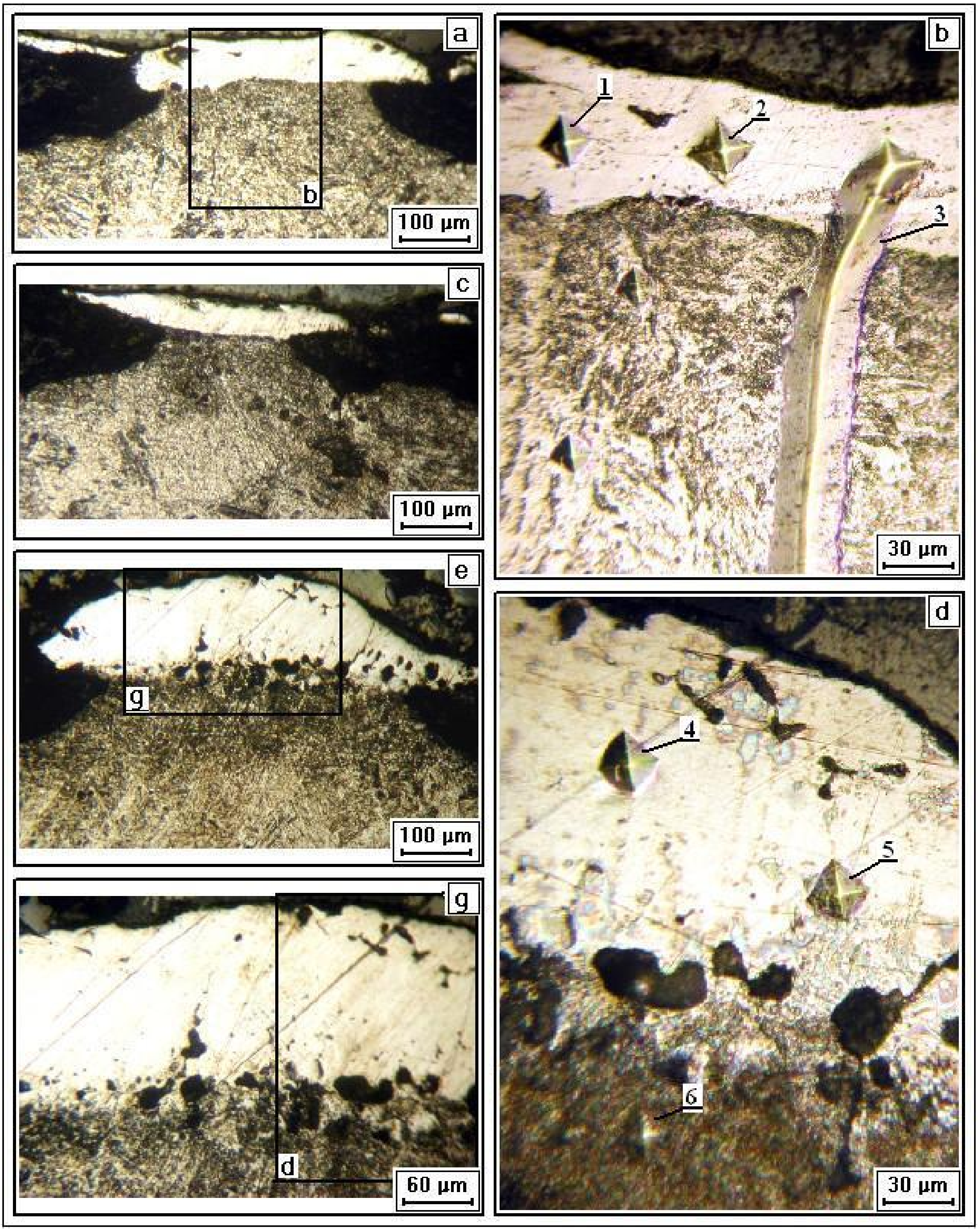

Fig. 2.32 - Steel microstructure near the top surface, area (G) wit enlarged fragments (1 – 6 diamond pyramid imprints after microhardness measurements and scleroscopy 3)

Metallographic investigations have yielded the following results:

The oxidic part of the block is porous, ranging from large pores like in Fig. 2.12 to micropores (see Fig. 2.29 a, c). The microsection also shows areas with dense corium, mostly in the ingot bottom part and on the lateral surface (Fig. 2.29 d).

In the subsurface layers of the steel specimen upper top, which profile is shown in Fig. 2.27 (line 2), the corium/steel interaction zone may be observed only at 8 to 10 mm from the specimen lateral surface. Judging by the surface microrelief (Fig. 2.30), in this area diffusion of the oxidic system components occurred along boundaries of austenite grains that form at high temperature. The traces of interaction are also visible in region E (see Fig. 2.31).

These regions are no thicker than 0.2 mm. The specimen macro- and microstructure above line 3 (Fig. 2.35) underwent transformations as the result of carbon and chromium repartitioning and grain size enlargement. This zone goes to a depth of 11 mm. No significant changes in macro- and microstructure occurred between lines 3 and 4.

On the post-interaction upper top of the steel specimen there left islets of metal with the minimal content of carbon (Fig. 2.32 a,c,e,g). In the decarbonized areas, microhardness was from 210 to 230 kgs/mm^2, and in the subsurface layers it varied within the 270÷350 kgs/mm^2 range, depending on the carbon content and steel structure. To illustrate the change of mechanical properties of the decarbonized areas and those below them, they were subjected to scleroscopy (scratching). The narrowing imprint of the diamond pyramid (see Fig. 2.32 b) and microstructural changes allow a supposition about the diffusion of carbon to the subsurface layer of the steel specimen upper top. Microhardness of the oxidic ingot varied within the 1700 ÷ 2000 kgs/mm^2 range.

3 DISCUSSION OF RESULTS

The data on corrosion rate obtained under specific conditions in MC10 and MC11 are summarized in Tab. 3.1. For the sake of a broader comparison and generalization, this table also contains the data from MC1 and MC2 of METCOR Phase 1.

Table 3.1 – Test results

Test	Melt composition	Atmosphere	Regime No	Specimen surface temperature, °C	Heat flux density, MW/m^2	Corrosion rate, mm/h
MC1	UO_{2+x}-ZrO_2-FeO_y	air	1	950	0.90	0.1
MC2			1	900	0.39	0.014
			2	990	0.44	0.068
			3	1050	0.47	0.076
			4	720	0.30	0.003
MC10	UO_{2+x}-ZrO_2	steam	1	1035	0.95	0.55
			2	1185	1.05	1.07
			3	1235	1.1	2.07
MC11	UO_{2+x}-ZrO_2-FeO_y		1	950	0.99	0.17
			2	1050	1.16	0.25
			3	1130	1.23	2.8
			4	1200	1.29	7.8

3.1 Analysis of the results from tests with molten UO_{2+x}-ZrO_2-FeO_y in air and steam

All the tests performed in the oxidizing above-melt atmosphere had the same peculiarity of time-independence of corrosion rate. Thus, time can be excluded from the parameters determining corrosion kinetics, and an attempt can be made of finding a relationship between corrosion rate and the main parameter, it being the steel surface temperature. Fig. 3.1 uses semilogarithmic coordinates to show corrosion rate data obtained in MC1, 2, 11, depending on the value, inverse to the indicated temperature. In accordance with the Arrhenius equation, the approximating dependence processed in such a way, should have linear character, if the change temperature change is not followed by the interaction mechanism change.

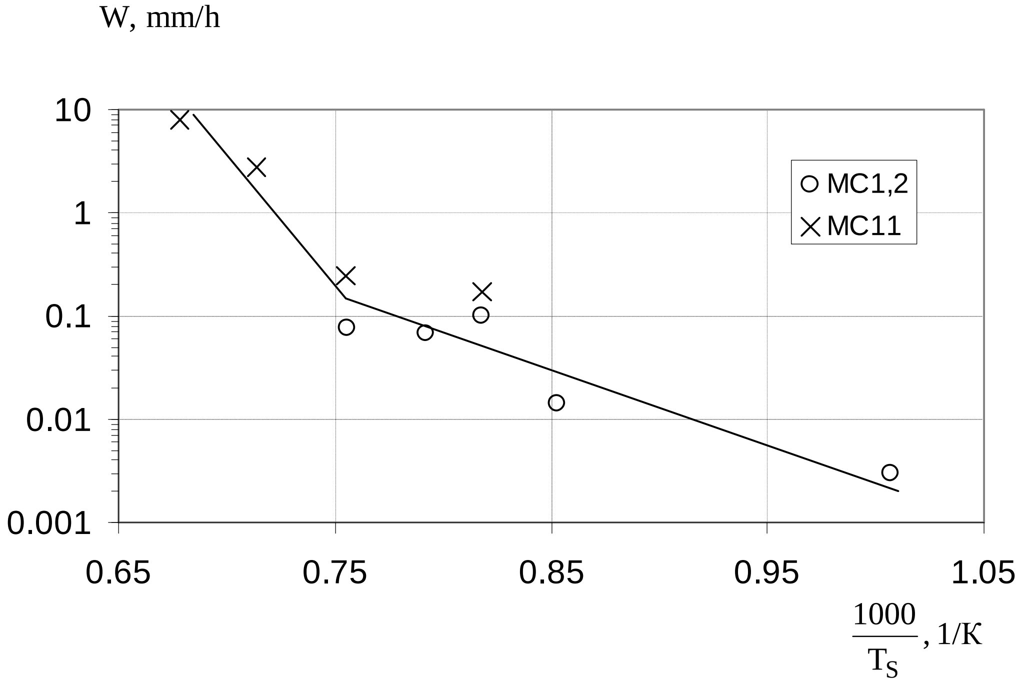

Fig. 3.1 – Dependence of corrosion rate on the specimen surface temperature

It may be seen from Fig. 3.1 that (1) at $T_S \approx 1050$°C (1323K) on the surface there is a bend in the dependence $W=W(1000/T_S)$, and (2) the scatter of points is great.

The generalization of data from MC1, 2 in [2] was based on the Tamman's equation in the below formulation:

$$W = A \exp\left(-\frac{E_a}{RT_S}\right) \cdot \frac{1}{\delta}, \qquad (3.1)$$

where W is corrosion rate, mm/h;

A is a numerical factor;

E_a is the energy of activation, J/mol.;

R = 8.314 J/(mol.·K) is the absolute gas constant;

T_S is the specimen surface temperature, K;

δ is the corrosion layer thickness, mm.

In [2], constancy of corrosion rate in time at T_S=const was linked with constant thickness of the corrosion layer δ, which serves as a diffusion barrier in the iron ions transfer to the surface of their oxidation. On the other hand, the corrosion layer thickness under thermogradient conditions is determined by the expression

$$\delta = \frac{\lambda \Delta T}{q}, \qquad (3.2)$$

where λ is the corrosion layer thermal conductivity, W/(m·K);

q is density of the heat flux to the specimen through the corrosion layer, W/m^2;

$\Delta T = T_\delta - T_S$ is the temperature difference in the corrosion layer, K;

T_δ is the temperature at the corrosion layer boundary, K.

By substituting δ from (3.2) into (3.1), we obtain

$$W = A\exp\left(-\frac{E_a}{RT_S}\right)\cdot\frac{q}{\lambda\Delta T}. \qquad (3.3)$$

The present analysis assumes an approximation that a change in the iron ions diffusion flux, which is determined by a change of T_S and governs the rate of corrosion, is compensated by an equal change in the diffusion flux of iron ions from the outer surface of the corrosion layer through the crust at a change of T_δ, equal in magnitude to the change of T_S, i.e. at ΔT=const. Then, at a temperature-independent value of λ, corrosion layer thickness δ would depend only on q, and the simplified dependence (3.3) becomes

$$W = A'\exp\left(-\frac{E_a}{RT_S}\right)\cdot q. \qquad (3.4)$$

The experimental data generalization in accordance with dependence (3.4) is shown in Fig. 3.2. Obviously, the scatter of points has significantly decreased, and within the range of scattering there is no difference between the data from tests performed in steam or in air. Nevertheless, the bend at $T_S \approx 1050°C$ (marked in Fig. 3.1) remained.

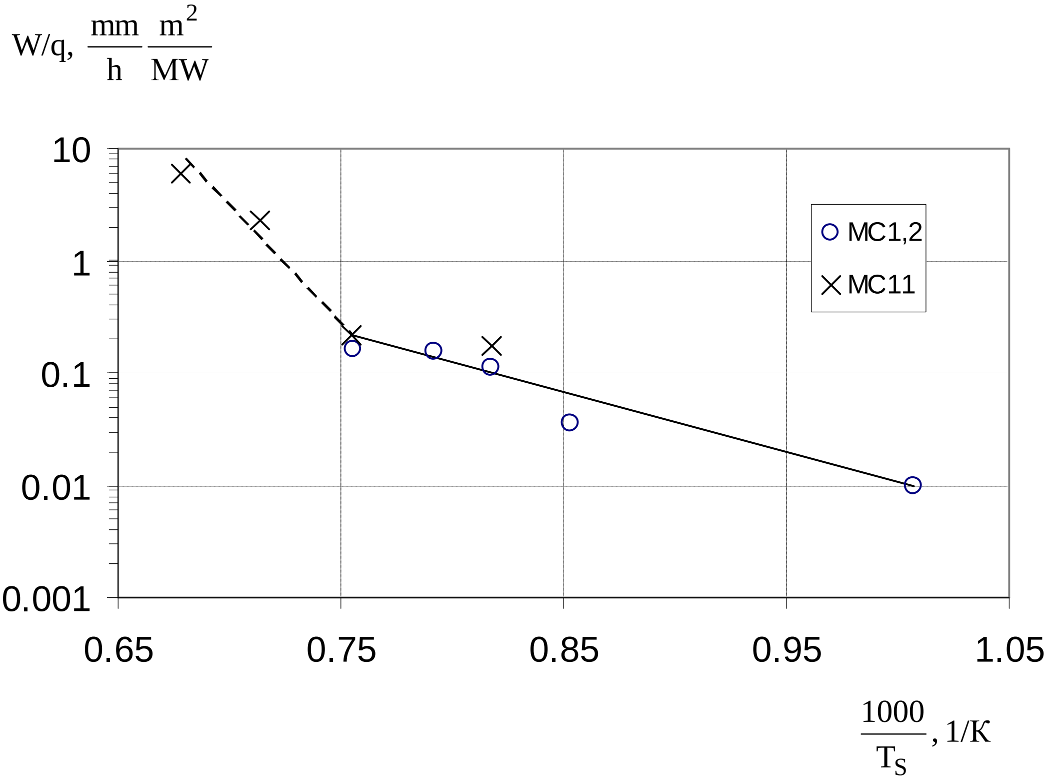

Fig. 3.2 – Experimental data generalization

In [2] it was noted that at the increase of T_S up to a certain value, T_δ may reach the eutectic temperature T_{eut} of the $UO_{2+X} – ZrO_2 – FeO_y$ system, which was accepted to be equal 1350°C. When generalizing the experimental data from MC1 & 2 using dependence (3.3), the value of T_δ was specified as the characteristic, i.e. T_δ=1350°C (1623K) and ΔT =1623- T_S, K. The data on corrosion in MC11 at the specimen surface temperatures above the previously attained T_S=1050°C (in MC2), as well as the bend (Figs. 3.1, 3.2) in the dependence of corrosion rate on the surface temperature at $T_S \geq 1050°C$ allow a supposition that T_δ may reach T_{eut} only at the increase of T_S up to 1050°C. When T_S grows above 1050°C, T_δ cannot exceed T_{eut} because of the eutectic melting of iron oxides at the corrosion layer boundary. Therefore, the assumption concerning the constancy of temperature change in the corrosion layer, which has been previously accepted and used for deducing dependence (3.4), becomes violated. At $T_S \geq 1050°C$

$\Delta T = T_{eut} - T_S$, noting that T_{eut} of the $UO_{2+X} – ZrO_2 – FeO_y$ system was refined in [18] and amounts to 1340°C. Fig. 3.3 shows four experimental points with $T_S \geq 1050$°C from MC2, MC11 within the W/q and 1000/ΔT coordinates. Apparently, they are generalized well by a simple linear dependence.

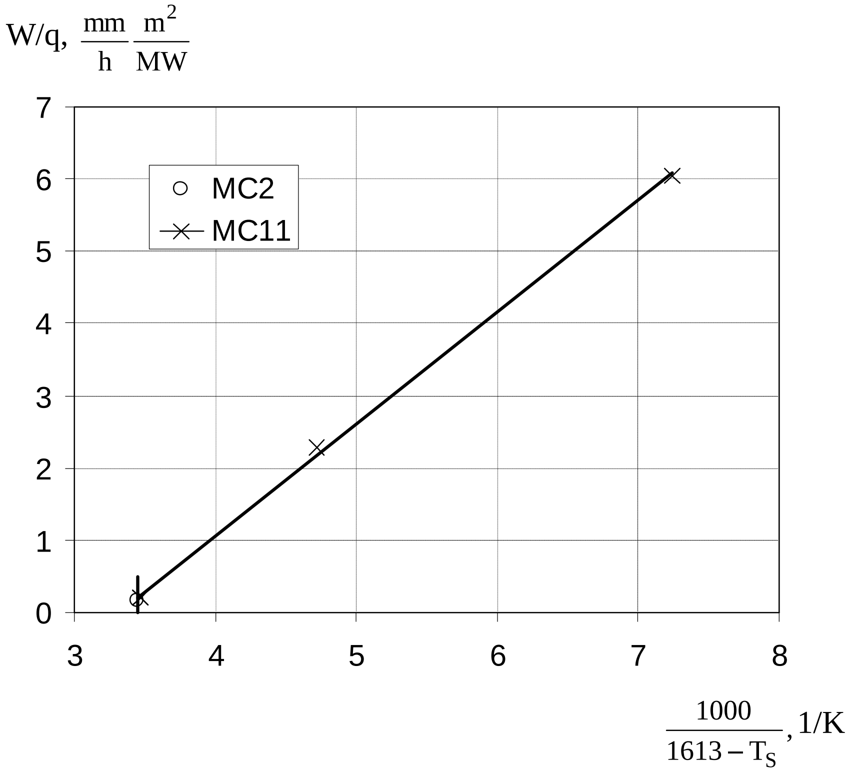

Fig. 3.3 – Generalization of experimental data for $T_S{}^{3}$1050°C (1323K)

It should be noted that for the $UO_{2+X} – ZrO_2 – FeO_y$ system with the components concentration specified in tests, T_{sol} is close to T_{eut}, i.e., at $T_S \geq 1050$°C in reality almost all the crust on the steel specimen surface was composed of iron oxides.

In accordance with the accepted model of the process, the relation between the corrosion layer thickness (δ) and crust thickness (Δ) at different temperatures on the surface of the steel specimen during its interaction with molten corium$UO_{2+X} – ZrO_2 – FeO_y$ is shown diagrammatically in Fig. 3.4.

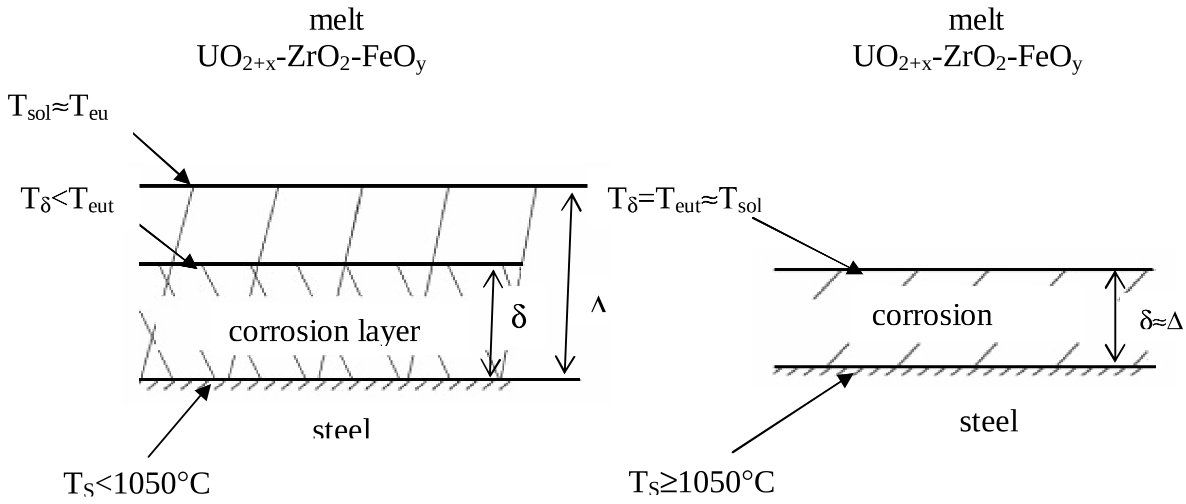

Fig. 3.4 – Simplified structure of the crust on the steel surface at the interaction with molten corium UO_{2+x}-ZrO_2-FeO_y

Unfortunately, the disruption of integrity of the oxidic crust (skull) on the specimen surface in the end of regime #4 of MC11 made it impossible to determine the corrosion layer structure and composition by the SEM/EDX of the corium/steel specimen interaction zone, and prevented confirmation of the hypothesized eutectic melting at the corrosion layer boundary after reaching 1050°C at steel surface. However, it may be indirectly confirmed by the SEM/EDX results for the interaction zone from MC2. For this purpose, data from [19] may be used.

Fig. 3.5 shows the interaction zone morphology. The figures on the left refer to different regions (layers), and those on the right – to corresponding thickness values in millimeters. The picture demonstrates 4 oxidic layers which can be distinguished after the molten pool crystallization between the steel specimen (region 1) and corium (region 6). Regions 2 and 3 are the common corrosion layer that almost completely consists of iron oxides, and regions 4 and 5 are predominantly composed of a mixture of iron and uranium oxides. The boundary between regions 5 and 6 is the crust boundary.

Microstructural and elemental analysis of phases in region 3 (see Figs. 3.6, 3.7) has revealed eutectic-like inclusions based on uranium oxides, with iron oxides concentration varying from 2.7 (Fig. 3.7) to 5.5 mass % (Fig. 3.6). Concentration of the uranium oxide-based phase grows in the direction towards corium.

It should be kept in mind that the “imprint” presented in Fig. 3.5 corresponds to the last regime in MC2 with 720°C at the steel specimen surface. This regime was preceded by another one with 1050°C at the steel specimen surface and a higher heat flux density (see Tab. 3.1). Apparently, in the last of the mentioned regimes the skull and corrosion layer were considerably thinner. Therefore, the eutectic-like structures discovered in layer 3 could form in the surface part of the corrosions layer (and skull), the position of which during the regime with T_S=1050°C was right within region 3 (Fig. 3.5) at the corrosion layer/corium boundary. It should be reminded that according to the proposed model of corrosion process, T_S=1050°C is the minimum temperature of the specimen surface, at which $T_\delta=T_{eut}$ at the corrosion layer boundary.

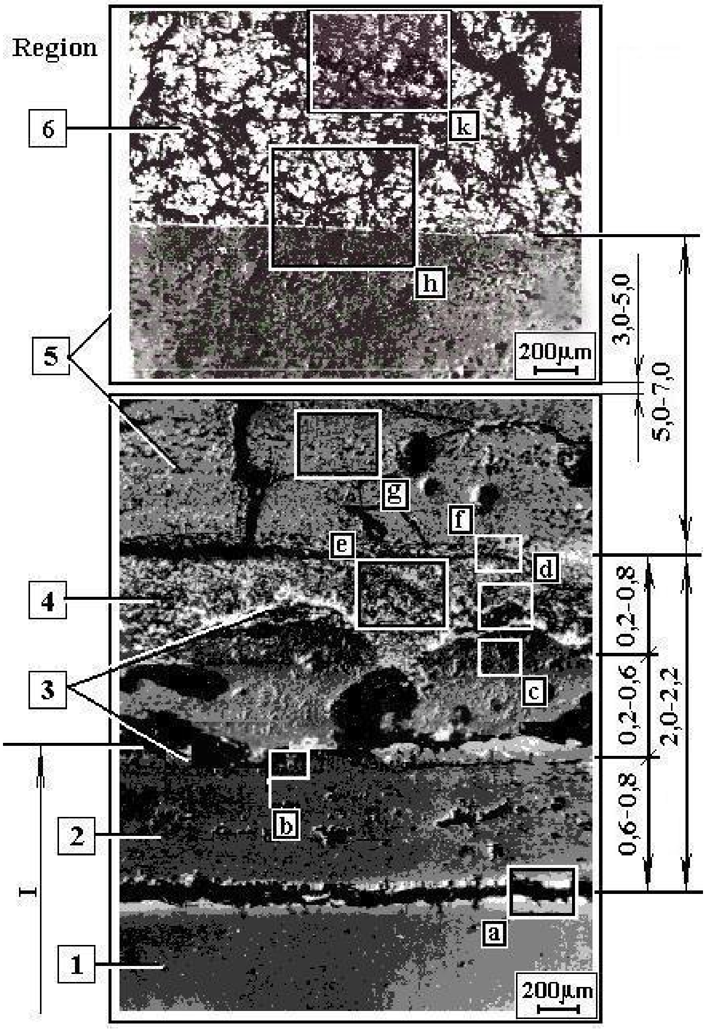

I – initial position of steel surface. 1 – steel specimen; 2÷5 – regions differing in structure and elemental composition; 6 – corium; a, b, c, d, e, f, g, h, k – fragments for which the SEM images were made and EDX analysis performed

Fig. 3.5 – Morphology of the corium/steel interaction transitional zone

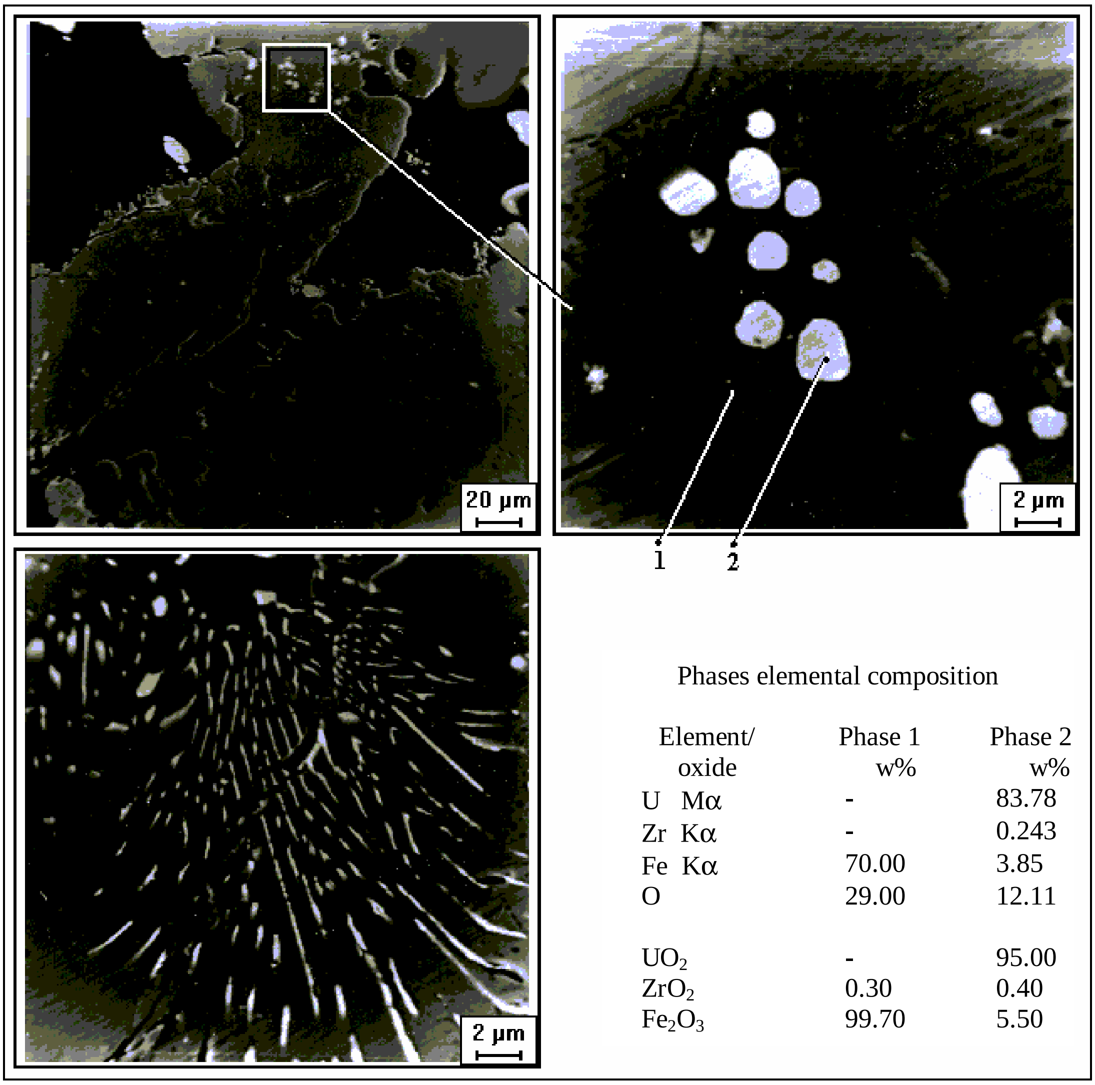

Phases elemental composition

Element/ oxide	Phase 1 w%	Phase 2 w%
U Mα	-	83.78
Zr Kα	-	0.243
Fe Kα	70.00	3.85
O	29.00	12.11
UO_2	-	95.00
ZrO_2	0.30	0.40
Fe_2O_3	99.70	5.50

Рис. 3.6 – SEM-имидж фрагмента [b] на рис. 3.4 и результаты количественного EDX-анализа

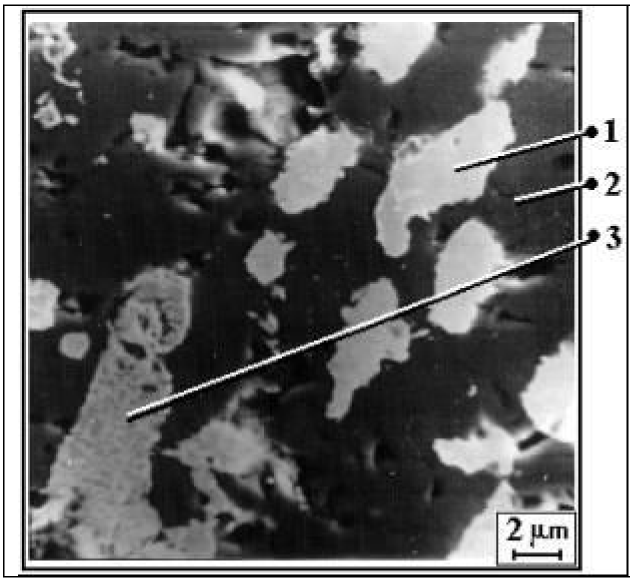

Phases elemental composition

Element/ oxide	Phase 1 w%	Phase 2 w%	Phase 3 w%
U Mα	59.76	0.06	80.09
Zr Kα	9.40	0.05	4.39
Fe Kα	14.55	70.01	1.86
O	16.27	29.87	13.66
UO_2	67.80	-	90.09
ZRO_2	12.70	-	5.90
FE_2O_3	20.80	100.00	2.70

Fig. 3.7 – SEM image of fragment [c] from Fig. 3.4 and results of quantitative EDX analysis

3.2 Results of tests with molten UO_{2+x}-ZrO_2

In Fig. 3.8, the experimental data on corrosion rates from MC10 are presented together with those from MC1, 2, 11 in the same way as in Fig. 3.2. A comparison of data obtained for two different corium compositions shows that:

1) In the case with corium UO_{2+x}-ZrO_2, the bend in the dependence of corrosion rate on the specimen surface temperature occurs at a higher surface temperature;

2) For corium UO_{2+x}-ZrO_2, the corrosion rate in the temperature domain confined by the corrosion layer boundary temperature, which is below T_{eut}, is approximately 2.5 times higher than for corium UO_{2+x}-ZrO_2-FeO_y.

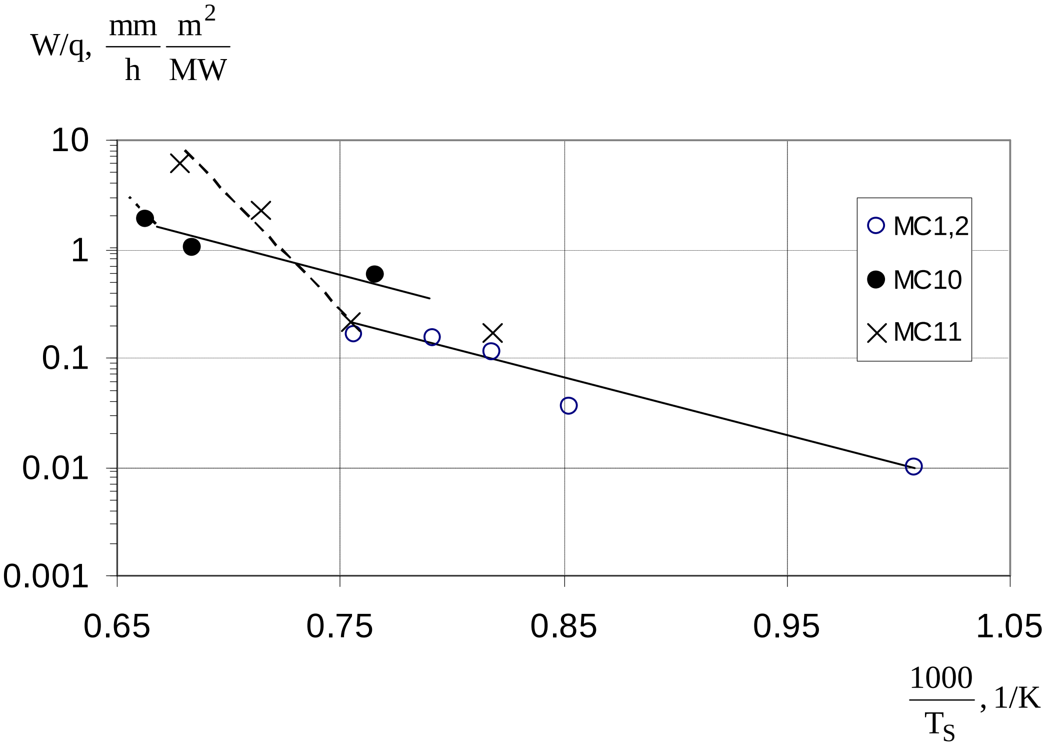

Fig. 3.8 – Generalization of experimental data from MC1, 2, 10, 11

From our point of view, the possible reasons for the noted differences may be as follows. Other conditions being equal, the corrosion rate increasing may be caused by a decrease in the corrosion layer thickness. The latter is determined by the balance of rates of iron ions “supply” to the corrosion layer and iron ions “removal” from the corrosion layer. The iron ions are “removed” by means of diffusion resulting from the difference of their concentrations in the corrosion layer and corium. The molar concentration of iron oxides (at loading) is 40% for corium UO_{2+x}-ZrO_2-FeO_y. In MC10, the corresponding concentration equals zero. Then, the difference of concentrations will be 100% in MC10 (UO_{2+x}-ZrO_2) and 60% for the tests with corium UO_{2+x}-ZrO_2-FeO_y, i.e. the “driving pressure” is noticeably higher under the MC10 experimental conditions. Besides, the temperature in MC10 was considerably higher than in the tests with a relatively low-temperature corium containing iron oxides. This condition is also possible of increasing the iron ions “removal”. As a consequence, the balance of iron ions “supply” and “removal” established in MC10 at a lower value of the diffusion coefficient, i.e. at a lower T_δ value and a smaller thickness of the corrosion layer.

A lower (than in the tests with molten UO_{2+x}-ZrO_2-FeO_y) temperature at the corrosion layer boundary in MC10 (other conditions being equal) means that the condition of T_δ=T_{eut} can be fulfilled at a higher specimen surface temperature, it being shown in Fig. 3.8. This T_S may be estimated to be around 1230°C.

Notable is that the crust is much thicker in MC10 than in the tests with the iron oxides-containing corium because of a much higher T_{sol}. Therefore, when the condition T_δ=T_{eut} is met, the corrosion layer reaches its utmost thickness within the crust, but this condition is not supposed to lead to qualitative differences of the processes at T_S≥1230°C in MC10 and at T_S≥1050°C in MC1, 2, 11 because of the liquid phase formation in MC10 inside the crust at T_S≥1230°C above the corrosion layer boundary. In the same way as Fig. 3.4, Fig. 3.9 shows the crust structure for molten corium UO_{2+x}-ZrO_2.

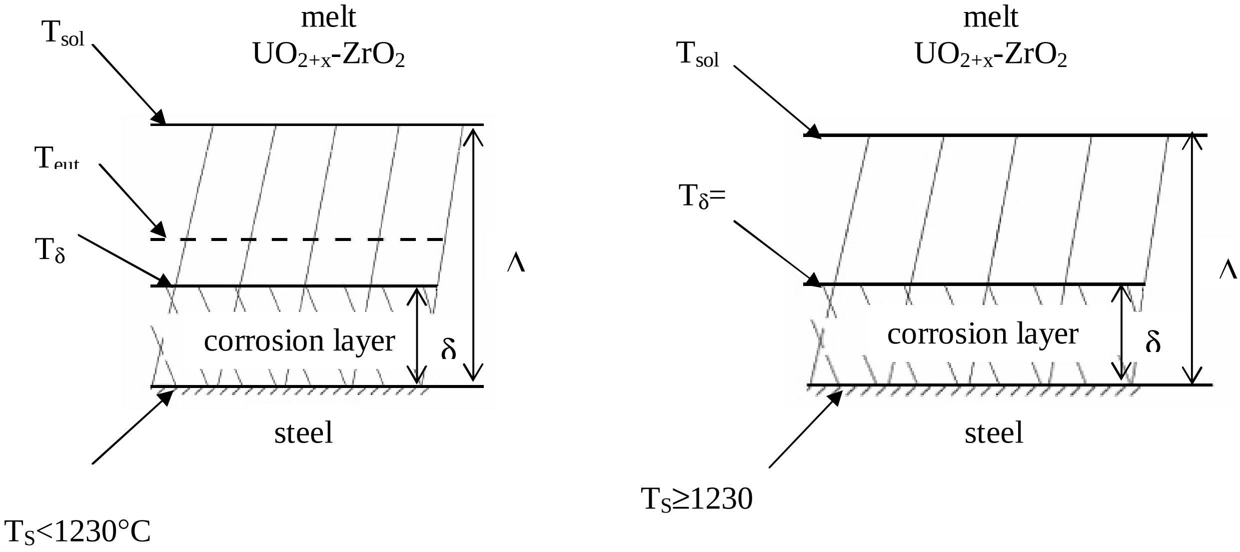

Fig. 3.9 – Simplified structure of the crust on the steel surface at the interaction with molten corium UO_{2+x}-ZrO_2

Fig. 3.10 repeats Fig. 3.3 and contains the single experimental point plotted from MC10, and a corresponding predicted corrosion rate dependence.

The match of the noted 2.5-time increase of the corrosion rate in MC10 to the growth of the T_S boundary value at which the condition of T_δ=T_{eut} is met in MC10, is confirmed by a close value of the temperature difference ratio in the corrosion layer at the said condition fulfillment: (1340-1050)/(1340-1230) ≈2.6.

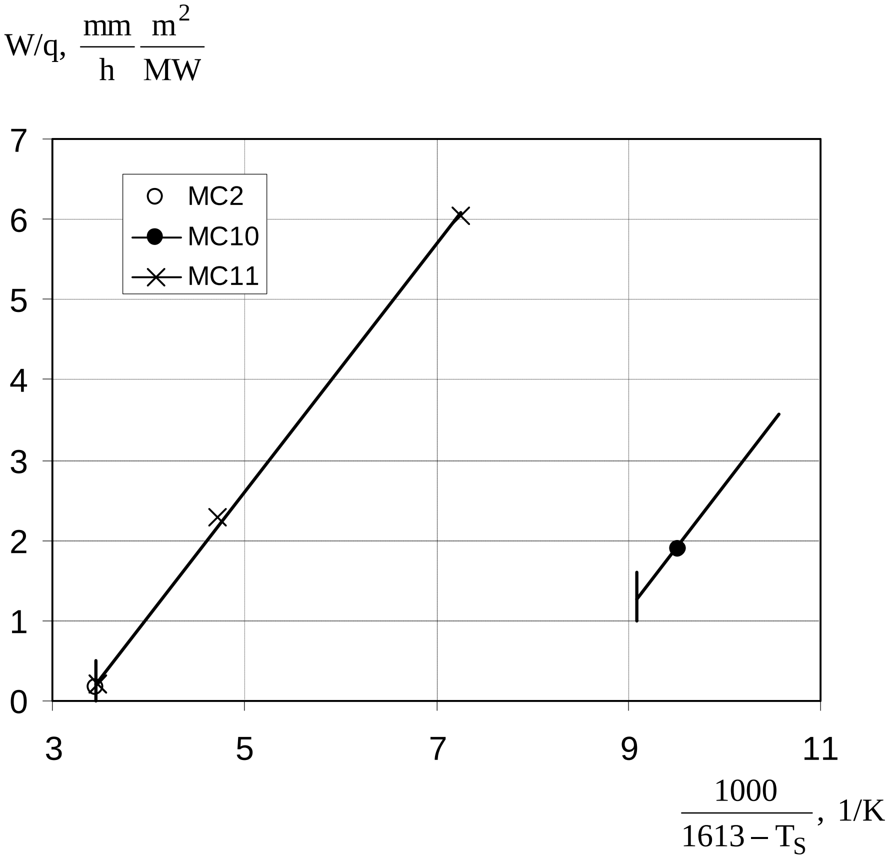

Рис. 3.10 – Generalization of experimental data from MC2, 11 for $T_S{}^3$1050°C (1323K) and MC10 for $T_S{}^3$1230°C (1503K)

3.3 Correlations concerning vessel steel corrosion kinetics during the interaction with molten corium in the oxidizing atmosphere

The processing of data from MC1, 2, 11 tests with molten UO_{2+x}-ZrO_2-FeO_y, has shown the rate of corrosion to be practically insensitive to the atmosphere (steam or air) in which the said corium was interacting with vessel steel. Hence, a common correlation can be used for generalizing these data. For the domain of the steel surface temperature change $T_S \leq 1050$°C, the approximation of 7 experimental points on the basis of dependence (3.4) is written as

$$\frac{W}{q} = 2330 \exp\left(-\frac{1.02 \cdot 10^5}{RT_S}\right), \tag{3.5}$$

where W is measured in mm/h, q – in MW/m^2, and T_S – in K.

For the temperature range of $1340 > T_S \geq 1050$°C a similar approximation of 4 experimental points looks as follows:

$$\frac{W}{q} = -5.28 + \frac{1.59 \cdot 10^3}{1613 - T_S}, \tag{3.6}$$

where W is measured in mm/h, q – in MW/m^2, and T_S – in K.

The value of activation energy in (3.5), i.e. $E_a = 1.02 \cdot 10^5$ J/mol., has increased in comparison with the value obtained in [2] when processing the results from MC1, 2, that is $0.7 \cdot 10^5$ J/mol. The difference is conditioned not by generalization of 2 additional points from MC11 in (3.5), but by the circumstance that [2] assumed $T_\delta=T_{eut}$ at the corrosion layer boundary, while in the present report this assumption was accepted only for the $T_S \geq 1050$°C temperature domain, while for $T_S \leq 1050$°C the constancy of temperature difference in the corrosion layer was assumed. The temperature $T_S=1050$°C is that very value at which the temperature at the corrosion layer boundary reaches $T_{eut}=1340$°C, and when T_S grows further, the corrosion layer thickness decreases inversely to $T_{eut}- T_S$. The corrosion rate is so strongly influenced by this factor that the influence of the diffusion coefficient increase because of the growing T_S is insensible, and this is confirmed by the linear (relative to $1/\Delta T$) character of dependence (3.6).

Though the data on corrosion rate is apparently deficient for corium UO_{2+x}-ZrO_2 , we can use the above-obtained activation energy value and, in accordance with Fig. 3.8, obtain a dependence that approximates 2 experimental points and differs from (3.5) only by the preexponential coefficient value:

$$\frac{W}{q} = 5870 \exp\left(-\frac{1.02 \cdot 10^5}{RT_S} \right). \tag{3.7}$$

This dependence is applicable to the $T_S \leq 1230$°C temperature domain. For the $1340 > T_S \geq 1230$°C temperature range a very approximate linear dependence can be obtained (in line with Fig. 3.10) which would be analogous to (3.6) and differ from it only by the absolute term value:

$$\frac{W}{q} = -12.8 + \frac{1.59 \cdot 10^3}{1613 - T_S}. \tag{3.8}$$

Generalization of the experimental data was based on the assumption that the temperature that determines corrosion kinetics is the steel specimen temperature at the corrosion front. Such an approach is quite justified in the framework of traditional investigations of corrosion under isothermal conditions. In the present case, however, conditions are very different from isothermal. Therefore, a comparison, e.g., of the activation energy value with a known value obtained under isothermal experimental conditions would be not quite correct.

If corrosion kinetics is controlled by diffusion processes in the corrosion layer, then some effective temperature of this layer that would be considerably higher than the specimen surface temperature under the experimental conditions in question may be considered as the determining temperature. An attempt of processing the experimental data from MC1, 2, 11 can be made having accepted the corrosion layer average temperature $T'_S = T_S + \Delta T / 2.$ as the effective temperature. In accordance with the previously accepted assumption, the temperature difference ΔT in the corrosion layer is constant for the $T_S \leq 1050$°C (1323K) temperature domain. Its value may be found from the condition of equality between the temperature of the corrosion layer boundary and the eutectic temperature at $T_S=1050$°C, i.e. $\Delta T=1340-1050=290$°C. The change of ΔT value in the $T_S > 1050$°C temperature domain follows the dependence $\Delta T=1340- T_S$.

Fig. 3.11 shows the results of a generalization similar to that presented in Fig. 3.2. In this case, the dependence that approximates 7 experimental points from the $T_S \leq 1050$°C (1323K) domain ($T'_S \leq 1195$°C (1468K)), is expressed as

$$\frac{W}{q} = 9250 \exp\left(-\frac{1.30 \cdot 10^5}{RT'_S} \right). \tag{3.9}$$

It is obvious that the activation energy (E_a) value of $1.30 \cdot 10^5$ J/mol. in the performed processing is much closer to $1.25 \cdot 10^5$ known for iron oxidation in air, than the value of $1.02 \cdot 10^5$ given in dependence (3.5).

When ΔT value is known for all the range of T_S variation, it becomes possible to use the Tamman's equation (3.1) and expression (3.2) for presenting all the experimental data as a dependence of $W\Delta T/q$ on T'_S (see Fig. 3.12). A sharp bend, like in Fig. 3.2, is visible. Before, it has been associated solely with the reaching of T_{eut} value by the corrosion layer boundary temperature T_δ. However, the bend remains during the experimental data processing (see Fig. 3.12) and it serves as an evidence that the eutectic melting at the corrosion layer boundary is accompanied not only by this layer thinning, but also by a considerable increase in the activation energy for the corrosion process. The approximation for the $T_S \leq 1050°C$ domain looks as:

$$\frac{W\Delta T}{q} = 2.68 \cdot 10^6 \exp\left(-\frac{1.30 \cdot 10^5}{RT'_S}\right), \qquad (3.10)$$

and the only difference of its right part from that of dependence (3.9) is in the preexponential coefficient. The corresponding approximation for the $T_S > 1050°C$ domain looks as

$$\frac{W\Delta T}{q} = 7 \cdot 10^{27} \exp\left(-\frac{7.32 \cdot 10^5}{RT'_S}\right), \qquad (3.11)$$

i.e., in comparison with (3.10) the activation energy has increased almost 5.5 times – from $1.30 \cdot 10^5$ up to $7.32 \cdot 10^5$. It should be noted that due to the small number of experimental points in from the $T_S > 1050°C$ temperature domain the last results cannot be accepted as statistically reliable. Besides, because of high values of and E_a the preexponential coefficient, the use of dependence (3.11) may lead to big errors. Therefore, the numerical analysis of corrosion under the VVER severe accident conditions and within the $1340 > T_S \geq 1050°C$ temperature range may justly employ dependence (3.6), moreover that this dependence generalizes the experimental data practically without scattering. In the case of molten corium UO_2-ZrO_2 interaction with steel, dependence (3.8) may be used in a very rough approximation for the corresponding temperature range $1340 > T_S \geq 1230°C$.

As for the choice of a dependence for calculating the rate of corrosion under the conditions when no eutectic melting has taken place yet at the corrosion layer boundary, all the considered correlations would be equal from the point of view of experimental points scatter. Presumably, more simple would be dependences (3.5), (3.7) which directly employ the steel temperature at the corrosion front as the argument.

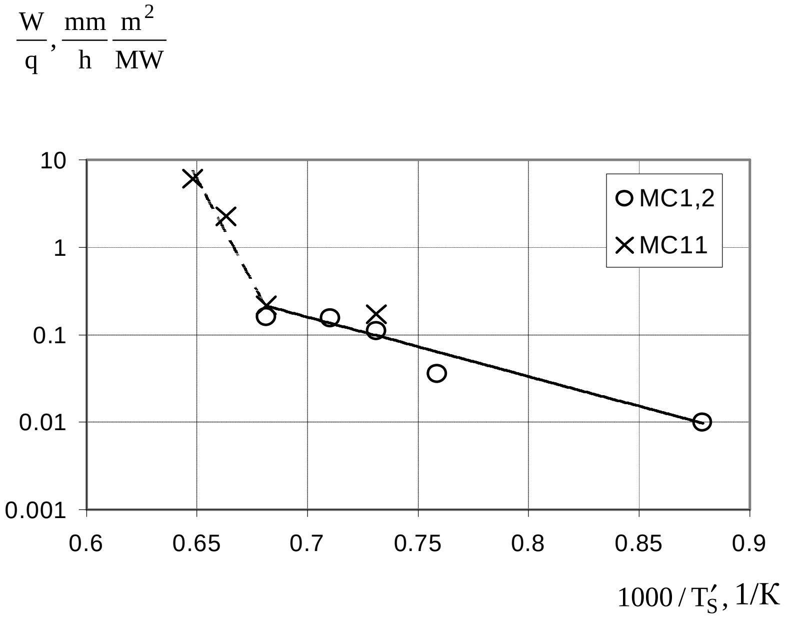

Fig. 3.11 – Experimental data generalization

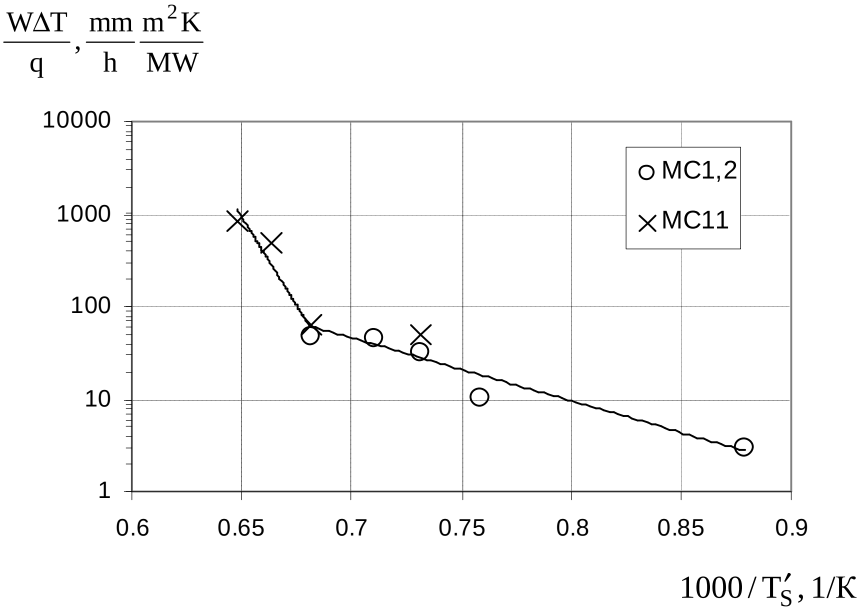

Fig. 3.12 – Experimental data generalization

An observation of the steel specimen final configuration in MC11 (see profilogram in Fig. 2.28) an its comparison with the typical temperature field in the specimen (Fig. 1.18) demonstrates the qualitative coincidence of the profilogram and isotherms in the specimen central part. For determining qualitative characteristics by the technique described in Sect. 1.2.3, 2.2.1, the specimen temperature condition prior to the generator switching off was calculated using the relevant thermocouple readings. The temperature field for the specimen upper part is shown in Fig. 3.13. The specimen corroded part boundary according to profilogram in Fig. 2.28 has been plotted in the field. It is clearly seen that a considerable length of the specimen central part profilogram is close to the ~1170°C isotherm. Deflections are due to the profilogram asymmetry which is not reproduced by calculations for the axis-symmetrically modeled thermal conductivity problem. Towards the specimen top surface edge, the temperature at the specimen corroded part boundary tends to go down towards 950°C. It should be noted that the temperature field in the specimen above the corrosion boundary is shown conventionally.

In order to understand if the obtained result was accidental or regular, steel corrosion has been calculated for the following arrangement. The temperature of 100°C was specified for the cold top of a 30-mm rod with thermal conductivity of 30 W/(mK), and a heat flux was directed to the hot top. As the result, the temperature distribution along the rod had the linear character with the unique dependence T=T(h). Then, the numerical time integration of equations (3.5), (3.6) ($W \equiv \frac{dh}{dt}$) made it possible to determine dependences h=h(t) and T=T(t), where T is the temperature at the corrosion front, h is the corrosion depth. Calculations were performed for 5 regimes with the incoming heat flux densities of 0.90 during regime #1, 0.95 (#2), 1.0 (#3), 1.1 (#4), and 1.2 MW/m^2 (#5) and hot top temperatures (T_0) of 1000; 1050; 1100; 1200 and 1300°C, respectively.

The results of calculations are presented in Figs.3.14, 3.15. As may be seen, corrosion depth at first grows quickly during the regimes with the initial hot top temperatures $T_0 \geq 1200$°C, but then the rate of corrosion slows down and further on the depth of corrosion increases extremely slowly, at approximately the same rates as at the very beginning during the regimes with $T_0 < 1200$°C. The higher the T_0 value is, the deeper corrosion is. The time dependence of temperature at the corrosion front during the regimes with $T_0 \geq 1100$°C shows a tendency to a common value of 1060°C, while at T<1100°C the temperature at the corrosion front decreases very slowly (it correlates well with the slow growth of ablation depth), and its value is noticeably lower than 1060°C.

Thus, for an interaction as long as that in MC11, the results of calculations have confirmed the possibility of temperature leveling at the corrosion front in the specimen, if corrosion proceeds in such a temperature range where corrosion rate is quite high (T>1100°C). If the neighbouring regions on the specimen top have a lower temperature, the depth of corrosion is insignificant there, the temperature practically does not change and noticeably differs from that at other areas of the corrosion front.

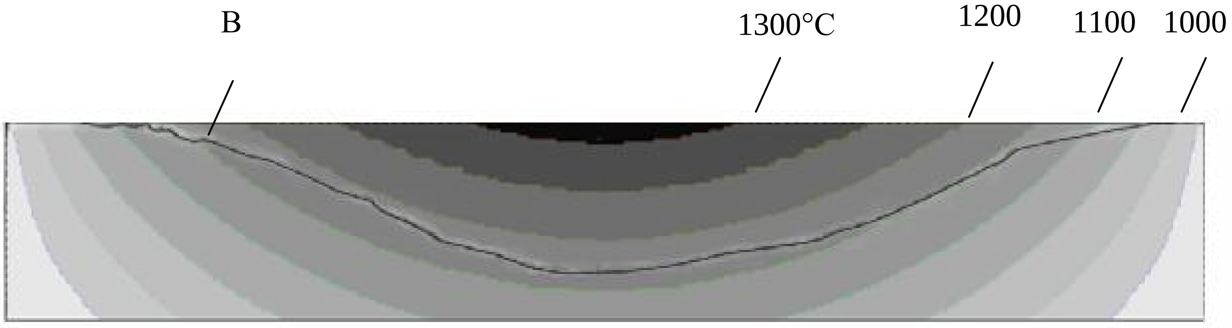

B – final position of the corrosion front

Fig. 3.13 – Temperature field in the specimen upper part before the generator switching off in MC11 (scale relations along R and Z lines are distorted)

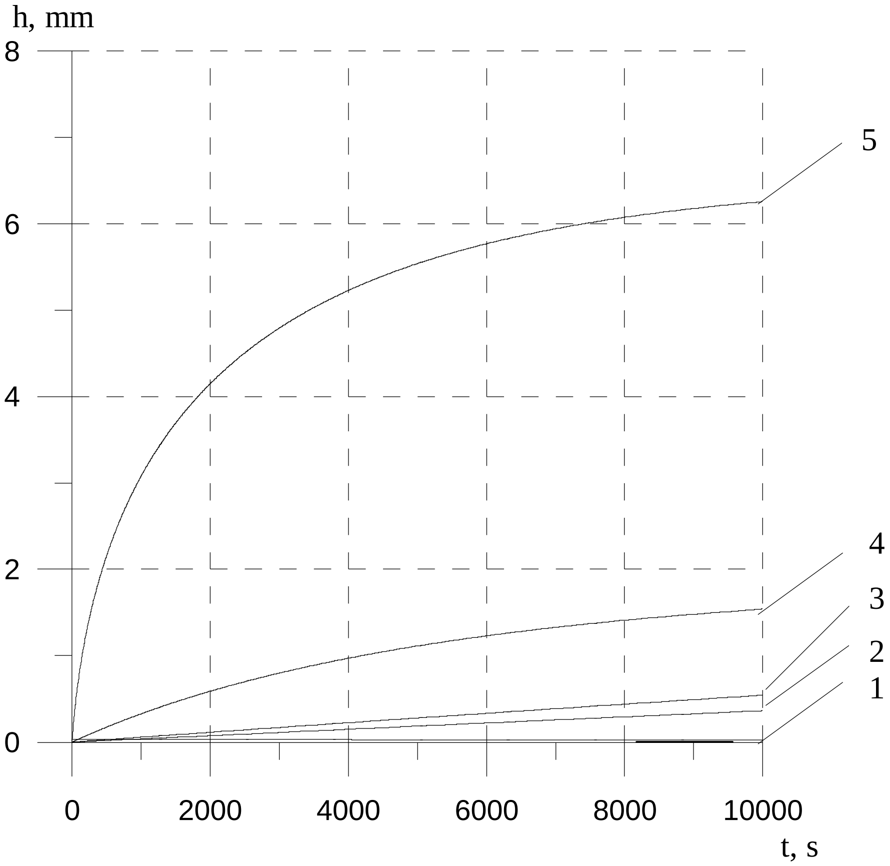

1…5 – regime numbers

Fig. 3.14 – History of corrosion depth

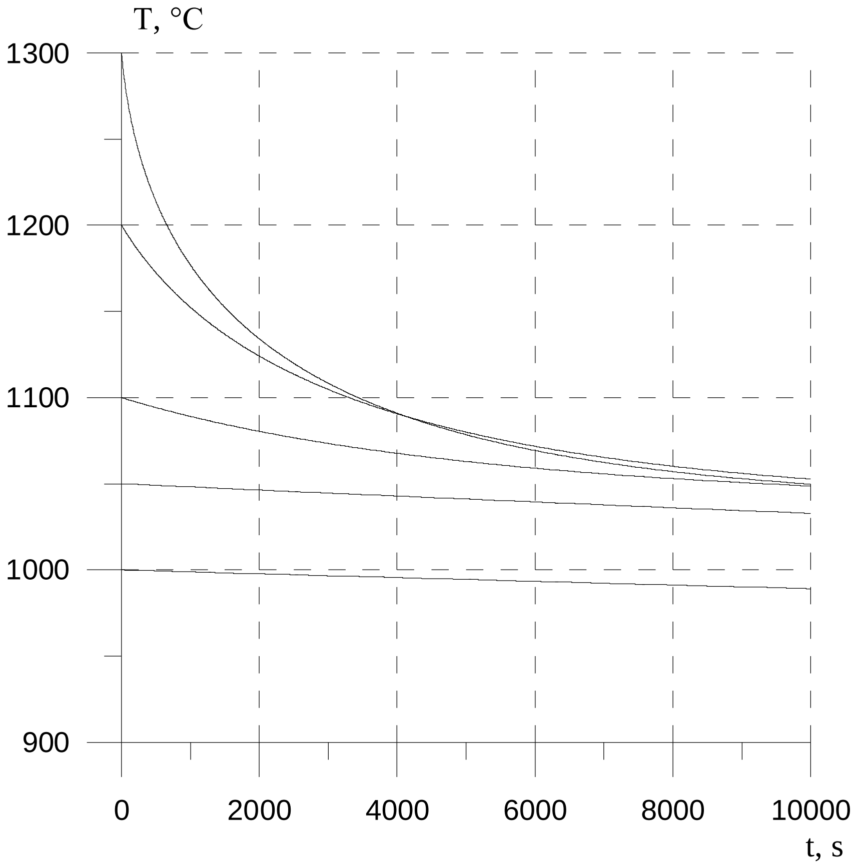

Fig.3.15 – History of steel temperature at the corrosion front

To check accuracy of the proposed correlations, corrosion kinetics of the specimen from MC11 has been calculated. Though these correlations have been obtained using the corrosion kinetics data from the same MC11, these data refer only to the mean integral values of corrosion depth in the specimen central part ∅15 mm.

The calculations have been performed as follows. By using the temperature fields in the specimen (see Sect. 2.2.1), the specimen temperature and heat flux density dependence on the distance from the upper top have been determined at several radial distances from the specimen axis (along several radiuses) for each regime (each temperature plateau). After that, numerical integration of corrosion rate correlations (3.5), (3.6) was done to obtain time dependences of corrosion depth (time intervals between plateaus and the interval after the 4th plateau till the generator switching off were 'added' to the neighbouring plateaus).

Fig. 3.16 shows the obtained dependences, and Fig. 3.17 offers a comparison of the calculated final corrosion depth with profilogram. A good agreement between the calculations and experimental findings is obvious, thus confirming satisfactory accuracy of both the proposed correlations and of the specimen temperature condition modeling technique.

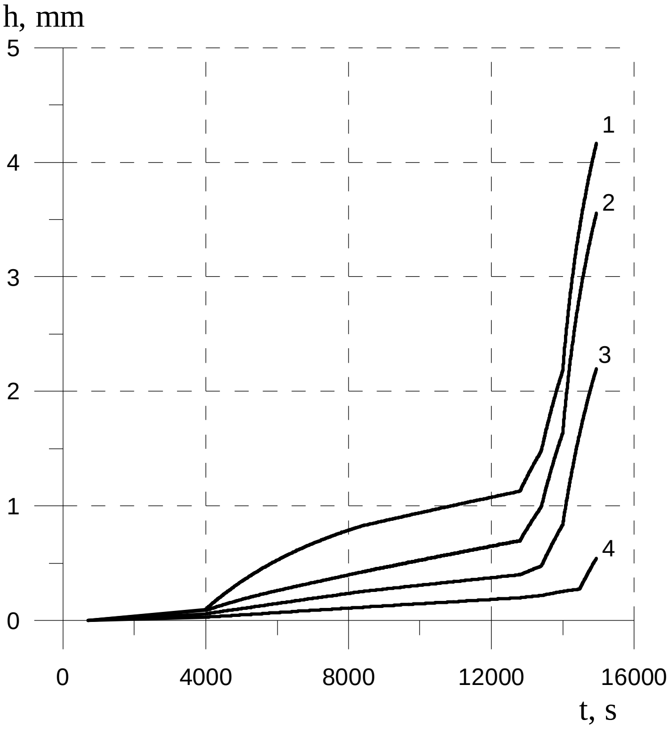

1 – R=0; 2 – 8; 3 – 16; 4 – 24 mm

Fig. 3.16 – Specimen corrosion kinetics

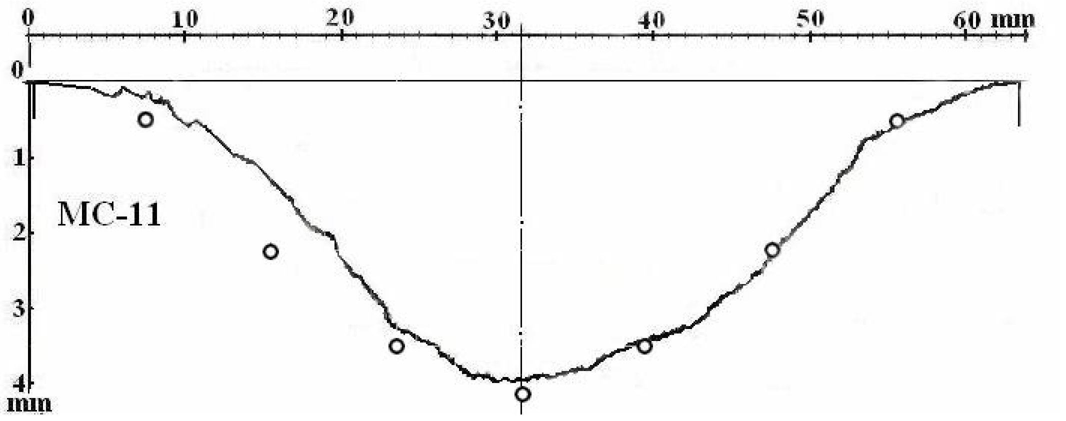

o – calculated; ▬▬ - profilogram

Fig. 3.17 – Comparison of calculated and experimental data on the final corrosion depth

The fundamental difference between the results of tests on the interaction of steel with the suboxidized molten corium and those with the fully oxidized corium in the oxidizing atmosphere should be stated. In the first case, the process of ablation of steel is based on its eutectic melting which is limited by T'_{eut} of the U-Zr-Fe-O system [4]. As a consequence, the final (end) position of the ablation front (after a sufficiently long exposure) has a clear boundary which corresponds to the T'_{eut} isotherm, i.e. on the specimen top there exist regions with a temperature below T'_{eut}, not in the least subjected to ablation. It is clearly seen, for example, in the picture showing the specimen section and profilogram from MC8 in which the suboxidized C-70 corium was used [4], Fig. 3.18.

At the interaction with corium in the oxidizing atmosphere, steel ablation represents the result of its corrosion, i.e. oxidation, which proceeds at any temperature (but at different rates which are temperature dependent). Under these conditions there can be no end position of the corrosion front within the actual area of temperature change. Therefore, as Fig. 3.18 shows, in MC11 corrosion occurred across the whole specimen top surface, but to different depths (in MC10 the picture has been distorted by steel melting at the final stage of the test).

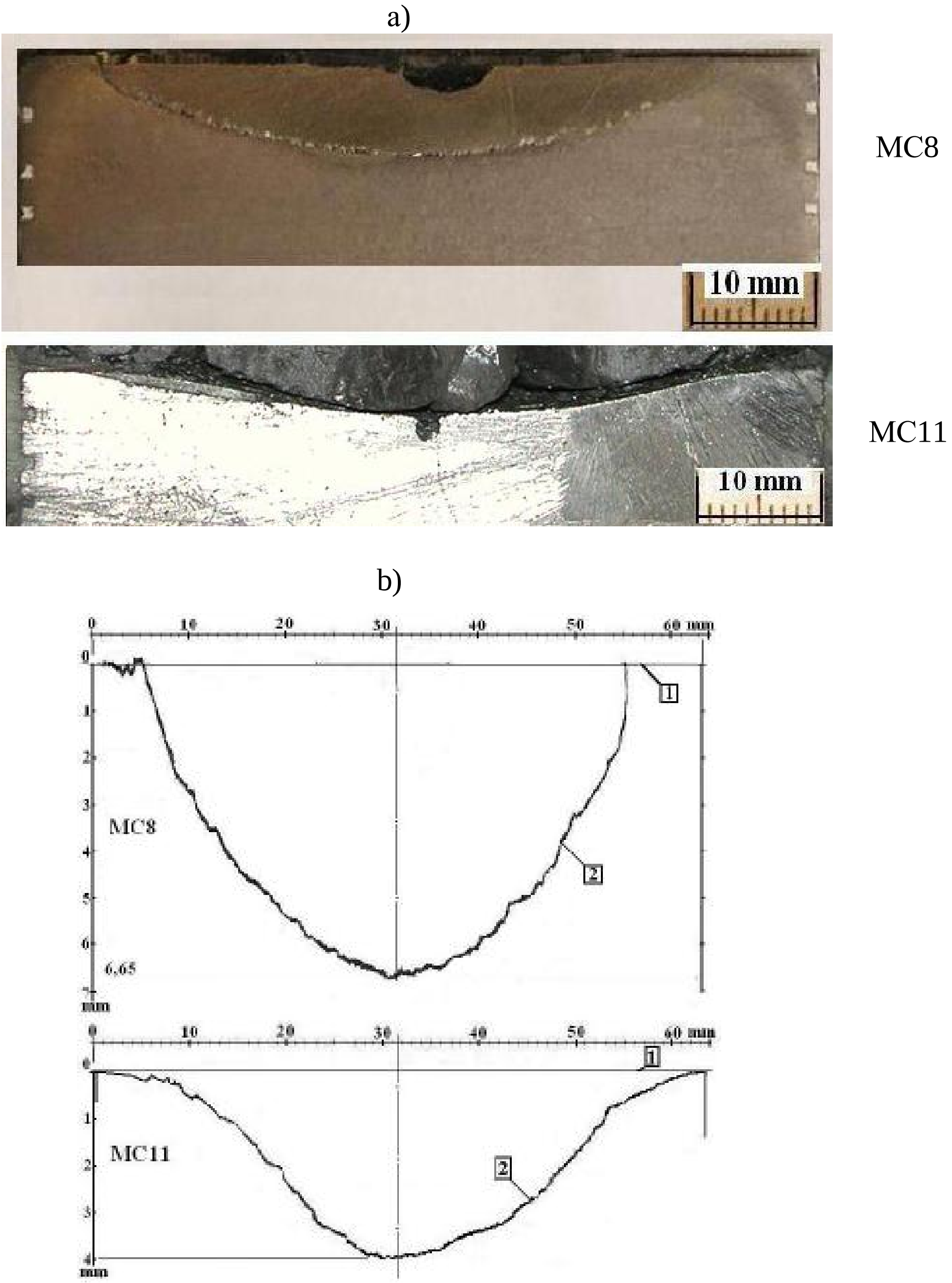

Fig. 3.18 – Comparison of the corrosion front (ablation) final shape) in MC8 & MC11;
a) – pictures of the specimen upper part longitudinal sections;
b) – profilograms, 1 – before interaction, 2 – after interaction

3.4. The liquid-phase burning mechanism of corrosion

The obtained correlations provide a formal basis for calculating corrosion at steel surface temperatures up to 1340°C. However, when the specimen surface temperature has reached only ~1200°C in MC11, instability expressed in a sharp uncontrolled rise of the specimen temperature was observed. It may be supposed that thinning of the corrosion layer (and crust), which is related to the specimen surface temperature rise, leads to the continuity violation and a contact of the steel surface with liquid corium. At that, the process of corrosion may accelerate considerably. However, of the highest danger are the conditions under which the rate of corrosion reaches a value at which the exothermal effect of steel oxidation manifests itself.

In a series of publications devoted to the in-vessel melt retention it was stated that from the point of view of the possible vessel melting-through the main danger is presented by the focusing effect of the molten steel surface layer. The heat flux to the vessel reaches its maximum density in the said zone, partial melting of the vessel occurs and its thickness becomes substantially smaller than the initial. At the same time, partial melting of the vessel also occurs, though to a shallower depth, in a limited area in the zone of contact with molten oxidic corium [20,21]. It should be noted that the above results have been obtained by calculating the vessel temperature condition under the quasistabilized stationary conditions.

Before the METCOR Project implementation, an experimental investigation of the interaction between the molten prototypic uranium-bearing corium and the water-cooled vessel steel in air on the Rasplav-2 facility has shown that at a steel surface temperature approaching that of steel melting, density of the heat flux from the melt to the vessel increases considerably and leads to intensive melting of the specimen [22]. A possible mechanism that may explain the observed effect is considered below.

After steel melting to a certain depth under the surface oxidic crust, disruption of the crust takes place. Due to the high oxygen potential of molten oxides, the melting steel oxidizes and the exothermal effect of the reaction causes a considerable growth of the heat flux to the steel wall. In accordance with our model of liquid-phase burning [23], a thin reaction layer forms near the steel wall, and heat from the redox reaction is generated in it. Part of this heat goes to the surface of steel, while another part goes to molten corium. Free convection is the mechanism of heat exchange. The described model was used in calculations with reference to the problem of in-vessel melt retention.

The following conditions have been accepted for the calculations:

- Considered is a steel wall, 0.18 m thick, at the initial temperature of 100°C. The temperature of the cooled surface does not change with time. The temperature of steel melting is 1500°C. The molten oxides temperature is 2500°C. Density of the heat flux from molten oxides to the wall (in presence of an oxidic crust) is 0.6 MW/m^2.
- The redox reaction U_3O_8+2Fe=3UO_2+2FeO with generation of 80 kJ/mol.Fe of heat, is taken into account.
- The fraction of melting steel that participates in the redox reaction within the reaction layer boundaries (μ) varies from 0 to 1.
- The problem is solved in the one-dimensional formulation.

Figs. 3.19, 3.20 show the history of the vessel non-melted part and of density of the heat flux removed from the cooled surface. With the increase of μ, the vessel non-melted part would be growing thinner, and the value of the maximum heat flux density would be getting higher. After the completion of melting, an oxidic crusts freezes on the wall and the heat flux decreases to the specified value of 0.6 MW/m^2.

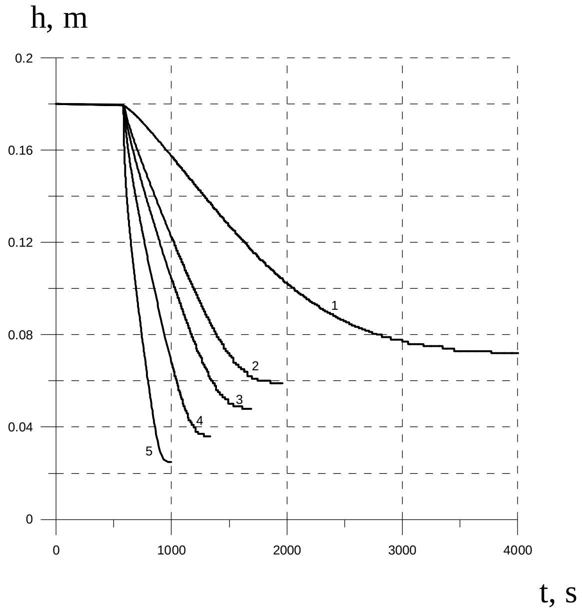

1 – μ=0; 2 – 0.1; 3 – 0.2; 4 – 0.5; 5 – 1

Fig. 3.19 – History of the steel wall thickness during the steel liquid-phase burning

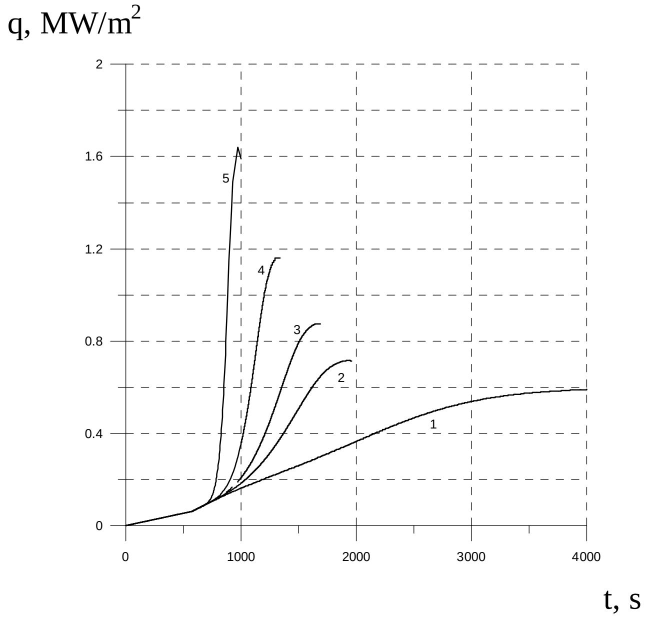

1 – μ=0; 2 – 0.1; 3 – 0.2; 4 – 0.5; 5 – 1

Fig. 3.20 – History of the removed heat flux density during the steel liquid-phase burning

As may be seen, at $\mu > 0.5$ density of the removed heat flux reaches the value comparable with the critical heat flux value (for the vertical surface in a big volume of saturated water at P=0.1 MPa $q_{cr} \approx 1.2$ MW/m^2).

The results of calculations confirm significance of the considered effect in the context of the discussed problem. Since the experimental data obtained by now are insufficient for making a conclusion concerning realizability of the considered effect, and its influence on the melt retainability in the vessel has never been taken into account, though it may be of special significance, it seems reasonable to conduct an additional experimental investigation with raising the steel specimen surface temperature.

Apparently, the redox reaction that leads to additional heat generation may proceed only when the molten oxides possess a high oxygen potential. However, the calculations performed to date to forecast a severe accident development and molten pool formation at the reactor vessel bottom, do not foresee such a situation. Nevertheless, taking into account uncertainties of some models, for instance, the model of interaction kinetics of the oxidic and metallic corium components in steam-air atmosphere after the remaining water has been evaporated from the vessel bottom, it would be premature to exclude the possibility that a molten pool with molten oxides possessing a high oxygen potential may form. This consideration is another convincing reason for conducting the proposed experimental investigation.

CONCLUSIONS

1 Tests have been performed for determining kinetics of the vessel steel corrosion at its interaction with molten corium UO_{2+x}-ZrO_2 and UO_{2+x}-ZrO_2-FeO_y in steam above the melt.

2 The corium composition has been shown to significantly influence corrosion kinetics, while experimenting in steam or air yields approximately similar results.

3 Two corrosion regimes differing in terms of kinetics have been identified. Transition occurs when the temperature at the corrosion layer outer boundary reaches 1340°C, i.e. the eutectic temperature of the UO_{2+x}-ZrO_2-FeO_y. system.

4 Correlations concerning vessel steel corrosion kinetics in the oxidizing atmosphere have been proposed. They generalize all the experimental data, including those obtained during METCOR Phase 1.

5 A numerical analysis of vessel steel oxidation by mechanism of the liquid-phase burning has been performed. Its results justify expediency of conducting investigations envisaging the steel specimen surface temperature increase.

REFERENCES

1. S.V. Bechta, V.B. Khabensky et al. Corrosion of Vessel Steel during its Interaction with Molten Corium. Part 1: Experimental. NED. 2006, in press.
2. S.V. Bechta, V.B. Khabensky et al. Corrosion of Vessel Steel during its Interaction with Molten Corium. Part 2: Model Development. NED. 2006, in press.
3. S. V. Bechta, V.B. Khabensky, V.S. Granovsky et al. New Experimental Results on the Interaction of Molten Corium with Reactor Vessel Steel, Proc. of ICAPP′04, Pittsburgh, PA USA, June 13-17, 2004, Paper 4114.
4. S.V. Bechta, V.B. Khabensky, V.S. Granovsky et al. Experimental Study of Interaction Between Suboxidized Corium and Reactor Vessel Steel, Proc. of ICAPP′06, Reno, NV USA, June 4-8, 2006, Paper № 6054.
5. I.V. Pozniak, A.Yu. Pechenkov, A.N. Shatunov. Induction Furnace with Cold Crucible as a Tool for Investigation of High Temperature Melts. 9th Korean-Russian International Symposium on Science & Technology / KORUS 2005, June 26 - July 2, 2005 Novosibirsk State Technical University , Novosibirsk, Russia.
6. Patankar S. Numerical Heat Transfer and Fluid Flow. Moscow. Energoatomizdat. 1984. 152 p. (Rus.)
7. SCDAP/RELAP5/MOD2. Code Manual, Vol.4: MATPRO-4 Library of Materials Properties for Light-Water-Reactor Accident Analysis, ed. J.K. Hohost, NUREG/CR-5273, EGG-2555, (1990).
8. RASPLAV Final Report. Behaviour of the corium molten pool under external cooling. Edited by V. G. Asmolov, V.F.Strizhov, Yu.G.Degaltsev, OECD RASPLAV Project, July, 2000.
9. Losev N.F. Quantitative X-ray fluorescence analysis. Moscow, Nauka Publishers, 1969. (Rus.)
10. Riabchikov D.I., Seniavin M.M. Analytical chemistry of uranium. Moscow, Publishing House of the USSR Academy of Sciences. 1962. (Rus.)
11. Lukianov V.F., Savvin S.B., Nikolskaya I.V. Photometric detection of uranium microquantities using reagent arsenazo III. JACh., v. XV, issue 3. 1960. (Rus.)
12. Markov V. K. et al. Uranium. Methods of its determination. Moscow, Atomizdat Publishers, 1964. (Rus.)
13. GOST 4011-72. Drinking water. Methods for determination of total iron. (Rus.)
14. Sendel E. Methods of metal traces determination by colorimetry. Moscow, Mir Publishers, 1964. (Rus.)
15. Butirin G.M. High-porosity carbon materials. Moscow, Khimiya Publishers, 1976. (Rus.)
16. Constitution diagrams of refractory oxidic systems. Reference book. Issue 5. Binary systems. Leningrad, Nauka Publishers, 1991. (Rus.)
17. Bekkert M, Klemm H. Reference book on metallographic etching. (Russ. transl.), 2nd edition, revised and updated. Moscow, Metallurgiya Publishers, 1988, 400 p., illustr.
18. Phase diagrams for multicomponent systems containing corium and products of its interaction with NPP materials (CORPHAD). Phase 2. Annual technical report № 2-1950.2-2003. Investigation of Ternary Oxidic Systems: System UO_x-ZrO_2-FeO_y., 2004.

19. Investigation of corium melt interaction with NPP reactor vessel (METCOR). Phase 1. Final technical report #833-1999 Appendix 2. Molten corium interaction with vessel steel in air. Test MC2/99, 1999.

20. Theofanous T.G. et al. In-vessel coolability and retention of a core melt. US Department of Energy. DOE/ID – 10460. 1996.

21. Kymalainen O., Tuomisto H., Theofanous T.G. In-vessel retention of corium at the Loviisa plant // Nuclear Engineering and Design. 1997. №169. P. 109-130.

22. Bechta S.V. et al. Experimental studies of oxidic molten corium – vessel steel interaction // Nuclear Engineering and Design. 2001. N210. P. 193-224.

23. Bechta S.V. et al. Molten corium interaction with oxidic sacrificial material of the corium localization device during a severe accident at an WWER NPP // Proceedings of ICAPP’05, Seoul, KOREA, May 15-19, 2005, Paper 5240.